

POLITECNICO DI TORINO

Master's Degree in Biomedical Engineering



Master's Degree Thesis

**Analysis of spatio-temporal parameters
during running at different speeds using
foot-mounted magneto-inertial sensors**

Supervisors

Prof. Ing. Andrea CEREATTI

Ing. Rachele ROSSANIGO

Candidate

Beatrice UTZERI

December 2023

Abstract

Running characterisation can be highly valuable in predicting the onset of running-related injuries, thereby enabling their mitigation or prevention, and in assessing runner's performances through the estimation of relevant spatio-temporal parameters, such as stride velocity and stride length. The existing literature presents a variety of approaches for the out-of-lab estimation of running spatio-temporal parameters utilising body-mounted magneto-inertial measuring units (MIMUs). The most widely used approach for assessing stride velocity and length is based on the double integration of feet accelerations between two consecutive ground contacts of the same foot. Specifically, the following steps need to be implemented. Firstly, foot orientation is estimated from the inertial data to remove the gravitational contribution from foot accelerations. Secondly, the zero-velocity update technique is implemented to detect the instants when the foot can be assumed to be stationary during the stance phase. The final step involves the removal of residual drift. As errors associated with each step propagate to the estimation of the final quantities, it is essential to identify sub-optimal values for each method composing the computational pipeline. However, this is not straightforward as the values of the optimal parameters may vary according to the running speed analysed. This thesis dealt with the identification, implementation, and fine-tuning of state-of-the-art methods for the estimation of stride velocity and length under different running speeds. For this purpose, two datasets were analysed. The first dataset included shoe-mounted inertial data from 10 amateur runners running at 14 km/h on a treadmill, and the stereophotogrammetric data considered as a gold standard. For the second dataset 10 elite runners were enrolled to perform 50-m sprints at their maximal speed (19-29 km/h) and were instrumented with shoe-mounted MIMUs. Pressure-sensitive insoles and video recordings were used as portable gold standards. The results obtained from the MIMU-based pipeline were compared with the references provided by the available gold standards. The optimisation procedure enabled to considerably improve the results with respect to a standard non-optimised pipeline: the mean absolute percentage error on running stride velocity decreases from 19.7% to 10.4%, and from 22.7% to 14.3% for the first and second dataset, respectively. For the stride length the mean absolute percentage error on running stride length decreases from 34.8% to 14.4% for the first dataset and from 34.9% to 16.2% for the second dataset. Thus, the proposed optimised pipeline is a promise solution for in-field running characterisation at different speeds.

Acknowledgements

At the end of this journey, I want to express my gratitude to Professor Cereatti for providing me with the opportunity to embark on this project and for serving as a significant mentor and resource throughout its execution.

I also extend my thanks to my supervisor, Ing. Rossanigo, for her invaluable assistance and unwavering support. Thank you, Rachele, for being an exceptional mentor and for making this research experience not only educational but also rewarding. Your encouragement and dedication have been a driving force behind the successful completion of my thesis.

I want to acknowledge the colleagues I have encountered during this experience. It wouldn't have been the same without you. I appreciate each and every one of you.

Finally, I want to express my thanks to all the people who have consistently believed in me, including my family and friends, who have continuously encouraged me to persevere despite the obstacles and challenges.

*“My dear, here we must run as fast as we can, just to stay in place.
And if you wish to go anywhere you must run twice as fast as that.”
Lewis Carroll, Alice’s Adventures in Wonderland*

Table of Contents

List of Tables	VI
List of Figures	VIII
1 Introduction	1
1.1 Background and Relevance	1
1.1.1 Running Cycle	2
1.1.2 Running spatio-temporal parameters	5
1.1.3 Instrumentation for Running Analysis	6
2 State of the art for the estimation of running spatio-temporal parameters	21
2.1 Spatio-temporal parameters computation pipeline	21
2.1.1 Orientation estimation and gravity removal	22
2.1.2 Zero Velocity Update (ZUPT)	26
2.1.3 Double integration and Drift Removal	27
2.1.4 Estimation of Stride Velocity and Stride Length	29
2.2 Issues and Challenges	29
3 Materials and Methods	31
3.1 Experimental protocols	31
3.1.1 Amateurs protocol - 14 km/h	31
3.1.2 Sprinters protocol - from 19 km/h to 29 km/h	32
3.2 Spatio-temporal parameter estimation with a non-optimised pipeline	33
3.3 Optimisation of the state-of-the-art methods for the estimation of running stride velocity and stride length	36
3.3.1 Zero Velocity detectors	36
3.3.2 Selection of integration boundaries	41
3.3.3 Orientation estimation and gravity removal	42
3.3.4 Methods for velocity drift removal	49
3.3.5 Validation procedures	49

3.3.6	Metrics for the pipeline assessment	51
4	Results	52
4.1	Spatio-temporal parameter estimation with the baseline pipeline . .	52
4.2	Optimisation of the state-of-the-art methods for the estimation of running speed and stride length	56
4.2.1	Zero Velocity detectors	57
4.2.2	Selection of integration boundaries of the integration interval	61
4.2.3	Orientation estimation	65
4.2.4	Methods for velocity drift removal	73
4.2.5	Comparison between the original pipeline and the optimised algorithm	77
4.3	Statistical Analysis	85
5	Discussion	91
5.1	Performance of the baseline pipeline	91
5.2	Performance of the optimised pipeline	92
5.2.1	Zero Velocity Detectors	92
5.2.2	Selection of integration boundaries of the integration interval	92
5.2.3	Orientation estimation and gravity removal	93
5.2.4	Results of the comparison of the methods for velocity drift removal	93
5.2.5	Final comparison between the baseline pipeline and the opti- mised pipeline	94
6	Conclusions	96
	Bibliography	98

List of Tables

3.1	<i>Threshold values for the ZUPT detectors.</i>	38
3.2	<i>Overview of the literature on the use of the ZUPT detectors in running analysis.</i>	39
3.3	<i>Experimentally determined threshold values for acceleration and angular velocity based on stride duration intervals.</i>	48
4.1	<i>Summary of the results obtained with the non-optimised pipeline for the dataset at 14 km/h.</i>	53
4.2	<i>Summary of the results obtained with the non-optimised pipeline for the dataset at 19-29 km/h.</i>	56
4.3	<i>Results of the percentage overlap between estimated ZUPT intervals and those obtained from the SP.</i>	60
4.4	<i>Results regarding the SV and SL at the ZUPT detector optimisation phase of the algorithm for the dataset at 14 km/h.</i>	61
4.5	<i>Overlap% between estimated ZUPT intervals and the reference</i>	65
4.6	<i>Results regarding the SV and SL at the ZUPT detector optimisation phase of the algorithm for the dataset at 19-29 km/h.</i>	66
4.7	<i>Results regarding the SV and SL with the four definitions of integration instants, for the dataset at 14 km/h.</i>	68
4.8	<i>Results regarding the SV and SL with the four definitions of integration instants, for the dataset at 19-29 km/h.</i>	68
4.9	<i>Results regarding the SV and SL with the different methods of initialisation of the quaternion, for the dataset at 14 km/h.</i>	70
4.10	<i>Results regarding the SV and SL with the different methods of initialisation of the quaternion, for the dataset at 19-29 km/h.</i>	73
4.11	<i>Results regarding the SV and SL with the different de-drifting methods, for the dataset at 14 km/h.</i>	74
4.12	<i>Results regarding the SV and SL with the different de-drifting methods, for the dataset at 19-29 km/h.</i>	76
4.13	<i>Results regarding the SV and SL with the different de-drifting methods, for the dataset at 14 km/h.</i>	81

4.14	. Results regarding the SV and SL with the baseline and the optimised pipeline, for the dataset at 19-29 km/h.	85
4.15	Statistical test results over the two dataset on SV and SL for evaluating the statistical differences between baseline and optimised pipeline.	89
4.16	Statistical test results over the two dataset on SV and SL, for evaluating the statistical difference between the two dataset with the same optimised pipeline.	90

List of Figures

1.1	<i>Visualisation of the running gait cycle, from [5].</i>	3
1.2	<i>Visualisation of rear-, mid- and forefoot strike types.</i>	4
1.3	<i>Gait cycle with phases and individual components. (A) Walking. (B) Running. From [8].</i>	5
1.4	<i>Passive Markers.</i>	7
1.5	<i>Illustration of an Optoelectronic system.</i>	8
1.6	<i>Force platform.</i>	9
1.7	<i>Instrumented treadmill.</i>	10
1.8	<i>Athlete utilising the Optojump Next[12].</i>	11
1.9	<i>Example of the attachment of MIMUs on the different body location [18].</i>	13
1.10	<i>Visualisation of different sensor positions on a running shoe [19].</i>	13
1.11	<i>Accelerometer spring-mass-damper system[21].</i>	14
1.12	<i>Representation of Yaw, Pitch and Roll. Adapted from [24].</i>	16
1.13	<i>Structure of a classic gyroscope. Adapted from [26].</i>	17
1.14	<i>Hall effect. Adapted from[27].</i>	19
1.15	<i>Pressure Insoles from the INDIP system [32].</i>	20
2.1	<i>Block Diagram of complementary filter, from [39].</i>	24
2.2	<i>Diagram of Kalman filter steps.</i>	24
3.1	<i>Subject wearing an inertial sensor on the instep of each shoe, below the red tape, and retro-reflective markers.</i>	32
3.2	<i>Subject wearing INDIP system including a MUMU and a pressure insole per shoe.</i>	33
3.3	<i>Camera placement scheme.</i>	33
3.4	<i>Exemplary diagram highlighting the first frame of the running trial (t_0).</i>	35
3.5	<i>Block diagram summarising the stages of the pipeline, explicitly showing, on the right, the algorithms employed in the baseline pipeline.</i>	35
3.6	<i>Extraction of the ZUPT intervals from the SP.</i>	40

3.7	<i>Extraction of the ZUPT intervals from the PIs.</i>	41
3.8	<i>Block diagram representation of the complete orientation estimation algorithm for Madgwick's complete orientation filter including magnetic distortion and gyroscope drift compensation.</i>	44
3.9	<i>Typical look of a wide angle lens.</i>	50
4.1	<i>Comparison between SV and SL derived from the SP and those obtained from the MIMU with the baseline pipeline.</i>	53
4.2	<i>Displacement estimated with the baseline pipeline, where the black curve represents the displacement in the horizontal plane x-y and the blue curve represents the vertical component. The dashed green line represents the averaged reference value provided by the SP.</i>	54
4.3	<i>Comparison between the MV obtained from the reference and from the MIMU with the baseline pipeline, among the 7 subjects, for the dataset at 19-29 km/h.</i>	55
4.4	<i>Comparison between SV and SL derived from the GoPro and those obtained from the MIMU with the baseline pipeline, among 7 subjects, for the dataset at 19-29 km/h.</i>	55
4.5	<i>Displacement estimated with the baseline pipeline, where the black curve represents the displacement in the plane x-y and the blue curve represents the vertical component. The dashed line represents the reference value provided by the GoPRO.</i>	56
4.6	<i>SHOE ZUPT intervals vs SP ZUPT intervals.</i>	57
4.7	<i>ARE ZUPT intervals vs SP ZUPT intervals.</i>	58
4.8	<i>MV ZUPT intervals vs SP ZUPT intervals.</i>	58
4.9	<i>MAG ZUPT intervals vs SP ZUPT intervals.</i>	59
4.10	<i>MAG ZUPT intervals vs SP ZUPT intervals.</i>	59
4.11	<i>Comparison between SV and SL derived from the SP and those obtained from the MIMU utilising different ZUPT detectors.</i>	60
4.12	<i>Comparison between displacement estimated with different ZUPT detectors. The dashed line represents the reference value provided by the SP.</i>	61
4.13	<i>SHOE ZUPT intervals vs Pressure Insoles ZUPT intervals.</i>	62
4.14	<i>ARE ZUPT intervals vs Pressure Insoles ZUPT intervals.</i>	62
4.15	<i>MV ZUPT intervals vs Pressure Insoles ZUPT intervals.</i>	63
4.16	<i>MAG ZUPT intervals vs Pressure Insoles ZUPT intervals. In the second interval. It is noticeable how the MAG detector fails to detect the zero-velocity update (ZUPT) interval.</i>	63
4.17	<i>Ma et al. 2018 ZUPT intervals vs Pressure Insoles ZUPT intervals.</i>	64
4.18	<i>Parametric ZUPT intervals vs Pressure Insoles ZUPT intervals</i>	64

4.19	<i>Comparison between SV and SL derived from the GoPro and those obtained from the MIMU utilising different ZUPT detectors.</i>	65
4.20	<i>Comparison between displacement estimated with different ZUPT detectors. The dashed line represents the averaged reference value provided by the GoPro.</i>	66
4.21	<i>Comparison between the SV and SL derived from the SP and those obtained from the MIMU utilising different definitions of integration instant for the integration intervals.</i>	67
4.22	<i>Comparison between the SV and SL derived from the GoPro and those obtained from the MIMU utilising different definitions of integration instant for the integration intervals.</i>	69
4.23	<i>Comparison between the displacement estimated with different definitions of integration instants. The dashed line represents the reference value provided by the GoPro (dataset at 19-29 km/h). T function is based on the angular velocity.</i>	70
4.24	<i>Quaternions with different initialisation methods. q_0 is the scalar number.</i>	71
4.25	<i>Comparison between SV and SL derived from the SP and those obtained with different quaternion initialisation methods.</i>	71
4.26	<i>Comparison between displacements evaluated with different quaternion initialisations methods, at 14 km/h.</i>	72
4.27	<i>Results regarding the SV and SL with the different methods of initialisation of the quaternion, for the dataset at 19-29 km/h.</i>	72
4.28	<i>Comparison between displacements evaluated with different quaternion initialisations methods, at 19-29 km/h.</i>	73
4.29	<i>Influence of the β value on the RMSE error on SV, at 14km/h. In orange, the RMSE value is presented with the beta of the baseline pipeline, while in purple, the value minimising the RMSE error is shown. In yellow, the trade-off value between the two datasets is reported to achieve a unique value.</i>	74
4.30	<i>Influence of the β value on the RMSE error on SL, at 14km/h. In orange, the RMSE value is presented with the beta of the baseline pipeline, while in purple, the value minimising the RMSE error is shown. In yellow, the trade-off value between the two datasets is reported to achieve a unique value.</i>	75
4.31	<i>Influence of the β value on the RMSE error on SV, at 19-29 km/h. In orange, the RMSE value is presented with the beta of the baseline pipeline, while in purple, the value minimising the RMSE error is shown. In yellow, the trade-off value between the two datasets is reported to achieve a unique value.</i>	76

4.32	<i>Influence of the β value on the RMSE error on SL, at 19-29km/h. In orange, the RMSE value is presented with the beta of the baseline pipeline, while in purple, the value minimising the RMSE error is shown. In yellow, the trade-off value between the two datasets is reported to achieve a unique value.</i>	77
4.33	<i>Comparison between the SV and SL derived from the SP and those obtained with and without the reliability check of the integration instants, for the dataset at 14km/h.</i>	78
4.34	<i>Comparison between SV and SL derived from the SP and those obtained with different de-drifting methods.</i>	78
4.35	<i>Comparison between displacements estimated with different de-drifting methods, for the dataset at 14km/h.</i>	79
4.36	<i>Comparison between SV and SL derived from the GoPro and those obtained with different de-drifting methods.</i>	79
4.37	<i>Comparison between displacements estimated with different de-drifting methods, for the dataset at 19-29 km/h.</i>	80
4.38	<i>Comparison between SV and SL derived from the SP, with the baseline and the optimised pipeline, for the dataset at 14 km/h.</i>	80
4.39	<i>Comparison between the displacements at the initial stage of the optimisation process (in red) and those at the end (in blue).</i>	81
4.40	<i>Bland Altman plot of all subjects in the dataset comparing SV from the SP and with the use of the baseline pipeline.</i>	82
4.41	<i>Bland Altman plot of all subjects in the dataset comparing SV from SP and with the use of the optimised pipeline.</i>	82
4.42	<i>Bland Altman plot of SL of all subjects in the dataset comparing SP and the results of the baseline pipeline (dataset 14km/h).</i>	83
4.43	<i>Bland Altman plot of SL of all subjects in the dataset comparing SP and the results of the optimised pipeline (dataset 14km/h).</i>	83
4.44	<i>Comparison between the trajectories at the initial stage of the optimisation process (in red) and those at the end (in blu), for the dataset at 14 km/h.</i>	84
4.45	<i>Comparison between MV, with the baseline and the optimised pipeline.</i>	84
4.46	<i>Comparison between SV and SL derived from the GoPro, with the baseline and the optimised pipeline.</i>	85
4.47	<i>Comparison between the displacements at the initial stage of the optimisation process (in red) and those at the end (in green).</i>	86
4.48	<i>Bland Altman plot of SV of 7 subjects in the dataset comparing GoPro and the results of the baseline pipeline (dataset 19-29 km/h).</i>	86
4.49	<i>Bland Altman plot of SV of 7 subjects in the dataset comparing GoPro and the results of the optimised pipeline (dataset 19-29 km/h).</i>	87

4.50	<i>Bland Altman plot of SL of 7 subjects in the dataset comparing GoPro and the results of the baseline pipeline (dataset 19-29 km/h).</i>	87
4.51	<i>Bland Altman plot of SL of 7 subjects in the dataset comparing GoPro and the results of the optimised pipeline (dataset 19-29 km/h).</i>	88
4.52	<i>Comparison between the trajectories at the initial stage of the optimisation process (in red) and those at the end (in green), for the sprinting dataset.</i>	88
5.1	<i>Block diagram summarising the stages of the pipeline, explicitly showing, on the right, the algorithms employed in the baseline and optimised pipeline.</i>	94

Acronyms

IMU

Inertial Measurement Units.

IC

Initial Contact.

FC

Final Contact.

SP

Stereophotogrammetry System.

GRF

Ground Reaction Forces.

COP

Center of Pressure.

COF

Center of the Force.

PI

Pressure Insoles.

INDIP

INertial module with DIstance sensors and Pressure insoles.

DCM

Direction Cosine Matrix.

CF

Complementary Filter.

KF

Kalman Filter.

EKF

Extended Kalman Filter.

INS

Inertial Navigation System.

DRI

Direct and Reverse Integration.

SV

Stride Velocity.

SL

Stride Length.

ZUPT

Zero-velocity UPdaTe.

MIMU

Magneto Inertial Measurement Unit.

Chapter 1

Introduction

1.1 Background and Relevance

Running is a basic human movement that has fascinated researchers, athletes, and fitness enthusiasts for ages. This lively activity, deeply rooted in our evolutionary past, showcases human flexibility and survival skills. Nowadays, it represents one of the most common and loved ways to stay active around the world. From the past up to now, running has been a lasting interest, appreciated for its simplicity, effectiveness, and significant positive effects on both body and mind [1]. Studying running is valuable in preventing injuries and enhancing athletes' performance [2].

This thesis centres on the study of running biomechanics, with a specific emphasis on estimating spatio-temporal parameters using signals obtained from wearable magneto-inertial sensors. In terms of research, an accurate understanding of spatio-temporal parameters is essential for coaches, clinicians, and researchers. In recent years, several works have attempted to estimate spatio-temporal parameters using body-mounted magneto-inertial measurement units (MIMUs) [3]. The existing literature offers various methods for estimating spatio-temporal parameters using body-mounted MIMUs. The most commonly employed approach involves integrating acceleration data between two consecutive ground contacts of the same foot. This method necessitates the combination of multiple algorithms within a single analytical framework. Firstly, it estimates foot orientation from inertial data to eliminate the effects of gravity on foot accelerations. Subsequently, it employs the zero-velocity update (ZUPT) technique to identify moments when the foot is stationary during the stance phase. This step is critical for enhancing the accuracy of parameters related to stride, as it defines the boundaries of strides, allowing for the integration of linear acceleration into velocity and, ultimately, foot displacement. The final step in this framework addresses the removal of residual

drift. However, a challenge with this approach lies in the fact that the results can exhibit variations depending on the running speed.

In this thesis, each component of this analytical framework has been implemented, drawing from existing literature and incorporating optimisations, with specific innovations introduced in certain aspects. The aim is to create an optimal procedure for estimating spatio-temporal parameters that can effectively adapt to different running speeds.

In particular, the Project Outline is organised as follows:

Chapter 1 (current chapter) gives an introduction of the topic of the thesis and explains the thesis rationale and general objectives. It provides a general overview of the running gait cycle and a short summary of the instrumentation commonly used in this field, with particular focus on the description of the general functioning of inertial sensors.

Chapter 2 describes the current state of the art of the estimation of the spatial parameters. Specifically, each step of the computation pipeline is thoroughly examined, focusing on the main issues encountered.

Chapter 3 details the experimental protocols and methodologies employed in the thesis. The implementation of each stage of the pipeline is described.

Chapter 4 describes the results obtained during the optimisation process.

Chapter 5 provides comments on the results and recommendations for the estimation of spatio-temporal parameters of running with inertial sensors on the feet at various speeds.

Chapter 6 summarises the thesis' major accomplishments.

1.1.1 Running Cycle

First and foremost, it is essential to define the term 'running' and explore how it differs from the simple act of walking. To begin with, running involves higher speeds compared to simple walking, consequently leading to amplified ground reaction forces. Even though walking and running may seem similar at first impact, their distinctive cycles show notable differences.

A complete gait cycle is defined by the presence of two successive phases, which are as follows:

- **Stance Phase:** The stance phase accounts for 60% of the stride and it begins with the foot strike, called initial contact (IC) and it ends with the toe off, terminal contact, called final contact (FC). It is the period that indicates the duration of ground contact where it sustains all or part of the body weight.
- **Swing Phase:** The swing phase takes up the last percentage of the gait cycle and relates to the period when the foot is not in touch with the ground but rather in the air as the leg extends towards the next foot contact[4].

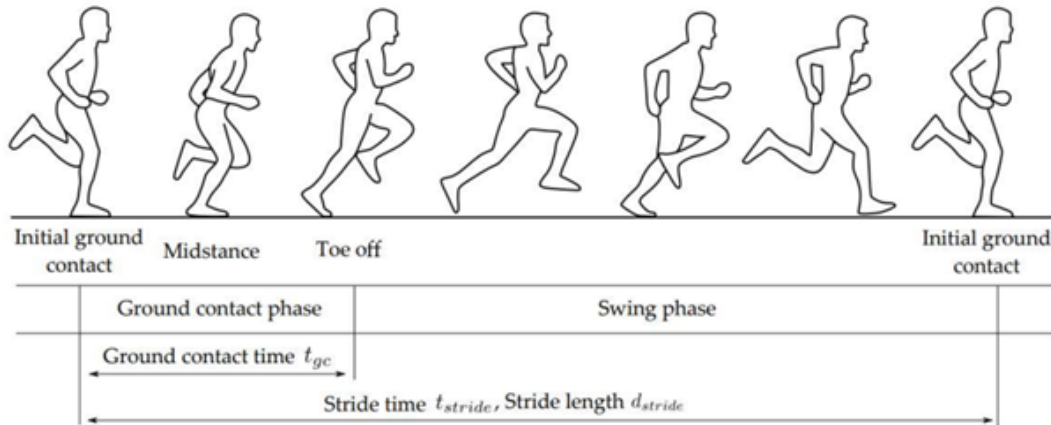


Figure 1.1: Visualisation of the running gait cycle, from [5].

Similar to walking, the running cycle can also be divided into different phases (depicted in Figure 1.1):

- **The Stance Phase** (ground contact phase), in which the foot is in contact with the ground. This phase is further divided into three stages:
 - *The initial contact.* In general, when pace increases from running to sprinting, the form of initial contact shifts from rearfoot contact to forefoot contact. Competitive runners often strike the ground with just the forefoot, never hitting the ground with the rearfoot, with the goal of covering the greatest distance in the shortest period of time. When running at slower speeds, the entire foot makes contact with the ground. Statistics reveal that the majority of runners (80%) are rear-foot strikers, with the remainder being mid-foot or fore-foot strikers [6]. During this phase, the impact of the body on the ground is cushioned through knee flexion, similar to the response to load phase in walking, but the flexion is more

pronounced. Moreover, muscles store elastic energy to be used during the propulsion phase.

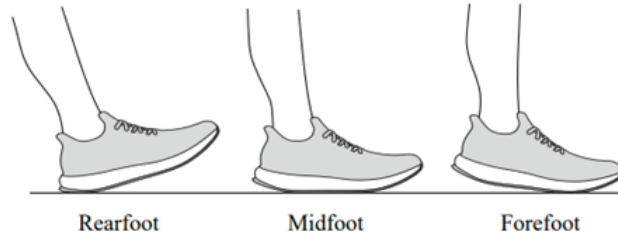


Figure 1.2: Visualisation of rear-, mid- and forefoot strike types.

- *The mid-stance* or single support phase. During this phase, the knee is at its maximum flexion, and the pelvis continues to move forward.
 - *The propulsion phase*. In this phase, the joints extend and release the elastic energy stored during the cushioning phase to propel the body forward and upward. Proper cushioning is essential for propulsion because the more elastic energy stored by the muscles, the less energy the muscles need to generate during this phase [7].
- **The Swing Phase**, in which the foot is off the ground. The flight phase begins at the moment of the final contact. Typically, the foot leaves the ground before reaching 50% of the entire running cycle. In contrast to walking, where support constitutes about 60% of the entire cycle and flight is about 40%, these percentages are reversed in running. Additionally, these percentages change with speed: the support phase is longer during slow running and shorter during fast running. High-level sprinters may leave the ground as early as 22% into the running cycle[7].

In other words, these two stages (stance and swing phases) can be observed in both running and walking; however, the timing of these varies. During walking, there is a phase of double support when transitioning from one foot to the other, during which both lower limbs are in contact with the ground. A differentiation between the running cycle and the gait cycle stems from the existence, in running, of the double-suspension phase, which replaces the double-support phase. As runners increase their speed, the duration of their stance periods becomes shorter. In Figure 1.3 it is possible to confront gait and running cycles [8].

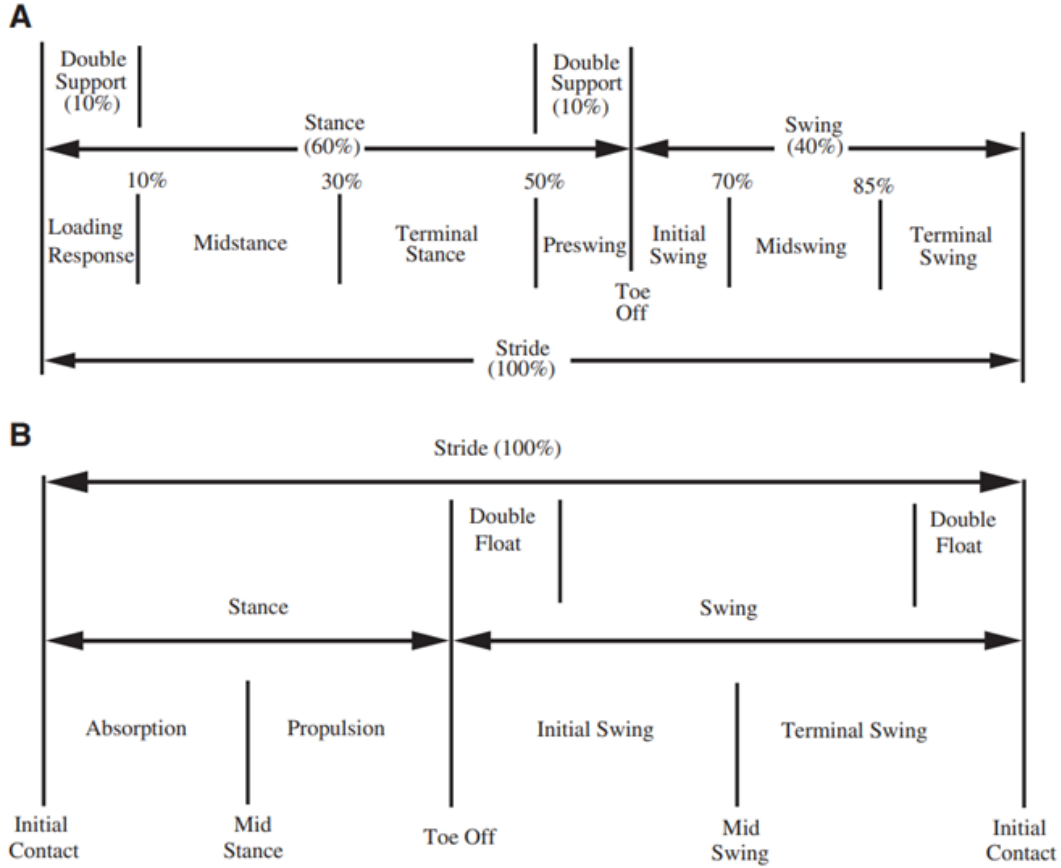


Figure 1.3: *Gait cycle with phases and individual components. (A) Walking. (B) Running. From [8].*

1.1.2 Running spatio-temporal parameters

While anatomical differences result in varying running styles among individuals, certain fundamental parameters can be commonly observed across different running patterns. In fact, spatio-temporal parameters have demonstrated a robust correlation with athletes' performance, rendering them excellent indicators of an individual's activity. This, in turn, enables coaches and athletes to gain enhanced insights into their movements.

Gait and running parameters can be divided into temporal and spatial parameters.

The temporal parameters provide temporal references, these are the parameters that have to do with time, such as timing and duration. They can be divided into:

- Cadence $[\frac{\text{step}}{\text{min}}]$, the number of steps per unit of time

- Stride duration [s], the duration of the stride
- Step duration [s], the duration of the step
- Stance phase duration [s], which starts with an IC and ends with an ipsilateral FC.
- Swing phase duration [s], which starts with an FC and ends with an ipsilateral IC.
- Speed [$\frac{m}{s}$], which is the distance covered by the subject per unit time.

The spatial parameters can be described as:

- Stride length [m], which is the distance between two consecutive contacts with the ground of the same foot. The stride length determines the local gait direction of progression
- Step length [m], which is the distance between the contact of one foot to the ground and the consecutive contact of the other foot.
- Stride width [m], which is the distance, computed perpendicularly to the direction of the gait, between the contact of one foot to the ground and the consecutive contact of the other foot.

1.1.3 Instrumentation for Running Analysis

For running analysis, several systems are employed. This section will present a description of some of the technologies utilised in the literature, the following can be listed:

- Optoelectronic systems
- Force platforms
- Instrumented mat or treadmill
- Photocell systems
- Magneto Inertial Measurement Units (MIMU)
- Pressure insoles

Optoelectronic systems

An optoelectronic system for Motion Capture is a very accurate tool that is often utilised as the gold standard in movement analysis. It consists of a set of video cameras that record the scene where the subject is moving. The cameras are typically calibrated and stationary. The subject's movement is calculated by processing the image data captured by the cameras. These systems can be divided into three categories based on the methodology used for analysis: systems with passive markers, systems with active markers, and markerless optical systems. This analysis system is also referred to as *Stereophotogrammetry* (SP) [9].

Method with passive markers

Systems for marker-based Motion Capture are composed of several elements: a set of at least two cameras equipped with flashes for scene illumination, a set of spherical markers covered with reflective material attached to the subject (Figure 1.4), and a computer that receives images from the cameras.



Figure 1.4: *Passive Markers.*

An algorithm extracts markers from images, reconstructing their three-dimensional positions using flashes and reflective markers for high-contrast images. Reflective markers, appearing brightly in captured images, interact with infrared light emitted by camera diodes, which is then captured by the cameras. Each camera, described by a simple mathematical model, generates a two-dimensional projection of a three-dimensional scene. Triangulation enables the calculation of marker positions, contingent on knowing the position and orientation of each camera. These parameters are determined during the system's calibration phase, involving accurate estimation of camera model parameters.

Calibration is carried out in two phases: in the first phase, a calibration object consisting of three orthogonal axes with markers attached at known positions is captured. This establishes the global reference system and obtains the positions and orientations of the camera planes. In the second phase, a rigid bar with markers, called the Active Wand, attached at known positions is moved along the three

directions in space within the calibration volume to obtain the internal camera parameters. This system reconstructs the three-dimensional position of the markers at each moment in time. During the tracking phase, the points are grouped to reconstruct the trajectories of each individual marker. Finally, to each trajectory, a specific anatomical meaning is assigned through an appropriate model. The main applications are in clinical and sports contexts. For a comprehensive gait analysis, a SP system is necessary to obtain a view of the subject's anatomical landmarks and their trajectories during the analysis. In Figure 1.5 there is an example of an Optoelectronic system.



Figure 1.5: *Illustration of an Optoelectronic system.*

Method with active markers

Systems using active markers are very similar to those using passive markers, but the markers consist of coloured LEDs that emit their own light. Therefore, an external illumination device is not necessary. Usually, the LEDs are activated sequentially so that the system can automatically detect each marker based on pulse synchronisation, thus facilitating the tracking phase. Nevertheless, these systems have not achieved the same commercial success as passive marker systems due to the presence of power and synchronisation cables for the markers, which makes the setup cumbersome [9].

Markerless Method

Optical markerless systems consist of systems that autonomously recognise different body segments in the acquired images and subsequently calculate their position

and orientation in three-dimensional space. Other markerless optical systems can recognize the entire subject's silhouette captured by the cameras and calculate the volume occupied by the subject in space at each moment in time. This technology aims to minimise the intrusion on movements, however minimal, caused by marker use. Moreover, it seeks to significantly reduce propagation times and, more importantly, analysis errors associated with marker utilisation. As data processing remains computationally intensive and accuracy is still limited, these systems are still in the research phase. Nonetheless, these systems are considered the future of Motion Capture systems [9].

Force platforms

Force platforms are a widely used instrument for movement analysis and are mechanical sensing systems designed to measure the Ground Reaction Forces (GRF). They can be either single-axial, which allows the measurement of only one component of the ground reaction force, or multi-axial, which enables the detection of all the components of said vector. Thanks to this system, it is possible to estimate the Center of Pressure (COP), the Center of the Force (COF), the moment around each axis, etc. [10].



Figure 1.6: *Force platform.*

Additional metrics can be estimated by knowing the frequency of the force data obtained, such as:

- Speed and power
- Displacement
- Temporal variables
- Asymmetry of the left and right sides

A force plate's constituent technical parts could consist of piezoelectric sensors, strain gauges, or beam load cells. These elements can change the force imposed on voltage. In addition, force plates can be implanted in instrumented treadmills used for in-lab gait analysis [11].

Instrumented mat or treadmill

In the field of gait and running analysis, instrumented mats and treadmills play a crucial role.

These advanced tools offer researchers and clinicians a regulated, highly quantified setting for the thorough analysis of biomechanical dynamics during walking and running. Instrumented mats, also known as instrumented walkways, are platforms with several pressure sensors integrated. These mats enable the measurement of the force spread across a certain region, or pressure, as opposed to the measurement of the resulting forces.

Instrumented treadmills and mats allow the collection of comprehensive data on people's gait patterns, including crucial variables like step length, contact times, and force distribution. This data enables a deeper investigation into how individuals walk, ultimately leading to improvements in our knowledge of human locomotion, injury prevention, and performance enhancement in various settings, from clinical applications to sports science. However, it's worth noting that both instrumented mats and force platforms are relatively expensive, require a significant amount of space, and are primarily used in laboratory settings.



Figure 1.7: *Instrumented treadmill.*

In Figure 1.7 there is an example of instrumented treadmill.

Photocell systems

Photocell systems in track and field events are commonly linked to applications such as photo-finish timing and distance measurements. However, these systems are a valuable tool in gait and running analysis for researchers and professionals in sports science, biomechanics, and physical therapy. These systems use photodetectors and light sources to capture data about an individual's movement and provide insights into their gait and running mechanics.



Figure 1.8: *Athlete utilising the Optojump Next[12].*

The OptoJump Next (Microgate, Bolzano, Italy) is an example of an innovative optical system for athlete performance's analysis (Figure 1.8). It is composed of a transmitting bar and a receiving bar. The LEDs positioned on the transmitting bar communicate with those on the receiving bar. The system detects any interruptions and calculates their duration. This enables the measurement of flight and contact times during a series of jumps with very high precision. The dedicated software allows for obtaining a range of athlete performance-related parameters, such as the stride length, the exact and average velocity, or the stride angle. Optojump Next, thanks to small, freely placeable cameras, also enables the recording of images from the tests performed. However, the cost of the system is very high, and it is only used by extremely high-level professional athletes [12].

Magneto Inertial Measurement Units (MIMU)

The development of low-cost, miniaturised inertial sensors has opened up new fields of application where traditionally the use of inertial sensors was either too expensive or the sensors were too bulky. Two such areas of application are gait analysis and pedestrian navigation, where the use of inertial sensors mounted on the feet has demonstrated promising results in the last decades [13].

Wireless sensor-based systems incorporating MIMUs have evolved as an alternative to camera-based laboratory systems. These sensors, which usually consist of tri-axial accelerometers, gyroscopes, and magnetometers, have the advantages of being lightweight, portable, affordable, and miniaturised, allowing prolonged outdoor examination. The alignment of the sensor with gravity (accelerometer), the Earth's magnetic field (magnetometer), and angular velocity (gyroscope) determines orientation estimates MIMUs. The quaternion format, which describes 3D rotation in space, represents these estimates [14].

Besides their benefits, sensor-based systems have drawbacks that need to be taken into account. A particular restriction is the presence of drift, which causes errors and results in incorrect orientation predictions. MIMUs are also impacted by ferromagnetic disturbances, which can lead to heading accuracy issues [14]. Different data correction algorithms can be used to reduce these errors. Moreover, misalignment between anatomical and sensor-based body segment coordination systems may result in inaccurate sensor-based spatio-temporal characteristics. These two coordination systems can be calibrated to minimise errors like this and increase precision. Wireless sensors have nevertheless been successfully used in obtaining spatio-temporal parameters during gait and running analysis despite these limitations [15]. Human movement has been increasingly monitored by using wireless sensors, either to assess the performances of athletes or to prevent injuries ([16]-[17]).

For the evaluation of the running events, sensors have been placed on the foot, the lumbar spine, and the tibia, as shown in Figure 1.9.

According to a thorough analysis conducted by Horsley *et al.* [20], the mathematical technique used is more important than where the sensor is placed when it comes to accurately detecting events. The ideal location would be in a hollow made in the sole of the shoe, according to comparative research done by Zrenner *et al.* [19] with a focus on the placing of the MIMU on the foot for the estimate of running gait characteristics. A representation of the different positions investigated is shown in Figure 1.10. Numerous studies in the literature utilise data from sensors positioned in the area located above the shoelaces. This thesis will also utilise signals from sensors placed in this manner.

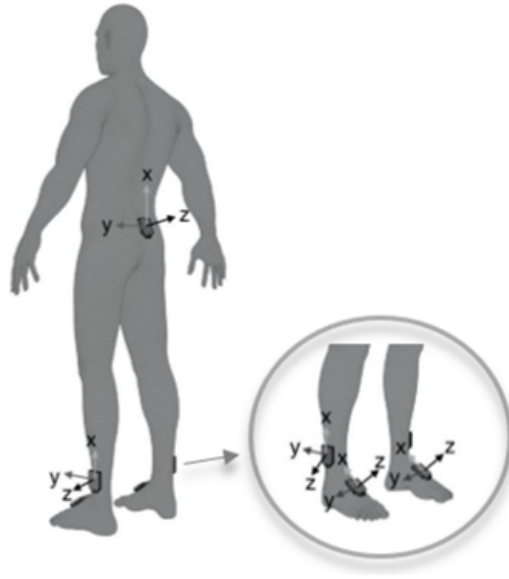


Figure 1.9: Example of the attachment of MIMUs on the different body location [18].

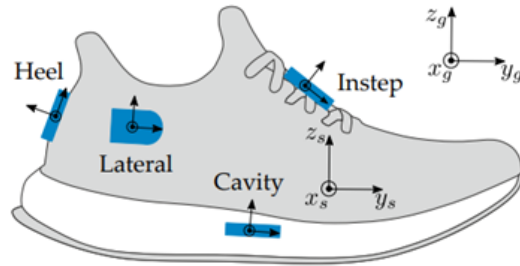


Figure 1.10: Visualisation of different sensor positions on a running shoe [19].

In this section, a detailed explanation of the components of a MIMU is presented.

Accelerometer

Accelerometers measure the *proper linear acceleration* a_p . The output of the accelerometer depends on the way it is mounted and on the motion it is subjected to. They can have one (uni-axial accelerometers) or two or three sensitive axis (tri-axial accelerometers). The most popular accelerometers on the market are uniaxial and triaxial. The *proper linear acceleration* a_p can be computed as the difference between the sensed acceleration a_s , that is, the rate of change of the

velocity of the sensor, and the gravity acceleration g . Thus, if the object is in free fall, the output of the measure will be 0 m/s^2 , while it will give $|\vec{g}| = 9.81 \text{ m/s}^2$ when it is stationary.

$$a_p = a_s - g \quad (1.1)$$

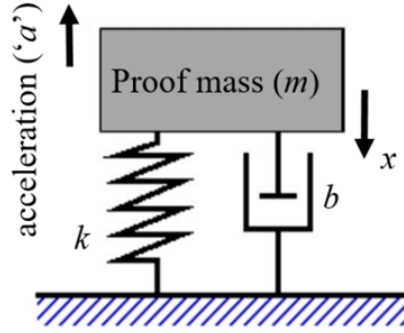


Figure 1.11: Accelerometer spring-mass-damper system[21].

An accelerometer can be modelled as a second-order spring-mass-damper system (Figure 1.11). When an acceleration (a) is applied to proof mass (m) suspended by springs with an elasticity constant (k) and a damping factor (b), then the force ($F_{applied}$) acting on the proof mass is given by:

$$F_{applied} = m \cdot a_{applied} \quad (1.2)$$

The force exerted by damping and springing in the system can be defined as follows:

$$F_{damping} = b\dot{x} \quad (1.3)$$

$$F_{spring} = kx \quad (1.4)$$

According to Newton's second law, the algebraic sum of the forces must be equal and opposite to the inertia of the body:

$$F_{applied} + F_{damping} + F_{spring} = m\ddot{x} \quad (1.5)$$

$$m\ddot{x} + b\dot{x} + kx = F_{applied} = m\ddot{x}_g = ma \quad (1.6)$$

Equation (1.6) is a non-homogeneous second-order differential equation. Its solution can be easily determined in the Laplace domain. The transfer function $H(s)$ of the system is given by:

$$ms^2x(s) + bsx(s) + kx(s) = F_{applied} = ma \quad (1.7)$$

$$s^2x(s) + \frac{b}{m}sx(s) + \frac{k}{m}x(s) = a(s) \quad (1.8)$$

$$H(s) = \frac{x(s)}{a(s)} = \frac{1}{s^2 + \frac{b}{m}s + \frac{k}{m}} = \frac{1}{s^2 + \frac{\omega_0}{Q}s + \omega_0^2} \quad (1.9)$$

Where ω_0 is the resonance frequency and Q is the quality factor:

$$\omega_0 = \sqrt{\frac{k}{m}} \quad (1.10)$$

$$Q = \frac{m\omega_0}{b} \quad (1.11)$$

Specifications

When choosing a device, certain specifications must be considered. Some of the main specifications that characterise an are listed [22]:

- **Sensitivity** [$\frac{mV}{g}$]: measures the minimum shift in the output corresponding to a change in the mechanical input and mathematically corresponds to the transfer function.
- **Bandwidth** [Hz]: quantifies the accelerometer's frequency range. Typically, a bandwidth of 40-60 Hz is sufficient to analyse human movement.
- **Zero-g voltage** [V]: specifies the expected voltage at 0 g.
- **Voltage noise density** [$\frac{\mu V}{\sqrt{Hz}}$]: Voltage noise changes with the inverse square root of the bandwidth: the faster the accelerometer provides readings, the worse the accuracy. Noise has a higher influence on the performance of the accelerometers when operating at lower g conditions with a smaller output signal.
- **Dynamic range** [g]: represents the maximum dynamic acceleration that can be measured accurately by the instrument.

Since accelerometers work in the low-frequency domain, a high resonance frequency is necessary to achieve a higher detection bandwidth. This specification can be obtained by reducing the size of the test mass and increasing the stiffness of the springs. However, as these variations can compromise the sensitivity of the device, a trade-off must be found.

$$Q = \frac{x}{a} \frac{m}{k} = \frac{1}{\omega_0^2} \quad (1.12)$$

Gyroscope

Gyroscopes measure the angular velocity of an object around its sensing axis. Gyroscopes can have one, two, or three detection axis. Angular velocity measurements are generally expressed in degrees per second. In combination with accelerometers, gyroscopes can be employed in several applications that need an integrated solution for inertial sensing and motion processing problems [23]. Depending on the direction, there are three types of angular rate measurements:

- Yaw: horizontal rotation on a flat surface when seen the object from above.
- Pitch: vertical rotation of an object seen from the front.
- Roll: the horizontal rotation of an object seen from the front.



Figure 1.12: Representation of Yaw, Pitch and Roll. Adapted from [24].

There are different commercially available classes of gyroscopes, but the more commonly used are mechanical and optical gyroscopes[25]. Due to the progress made in MEMS technology, miniature gyroscopes can become common.

Operating Principle

Classical gyroscopes operate based on the principle of the law of conservation of angular momentum, which states that the angular momentum of a system remains constant unless an external force acts upon it. When such an external force is applied, the object strives to maintain a fixed orientation with its axis pointing in the direction of rotation.

In Figure 1.13, the green disc represents a body that can rotate around its own axis, allowing for the application of a rotational force. Applying a force to the disc generates a moment known as the moment of force (τ , also referred to as torque). For instance, when the disc starts to rotate anticlockwise at a specific angular velocity (represented as ω), it creates an angular momentum (often denoted as L), which can be quantified using the following formula:

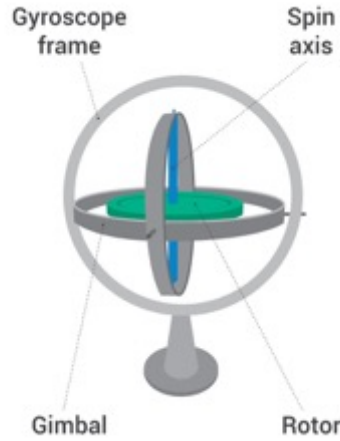


Figure 1.13: *Structure of a classic gyroscope. Adapted from [26].*

$$L = Ix\omega \quad (1.13)$$

Additionally, it is possible to express the torque (τ) acting on a system as the rate of change of angular momentum (L) with respect to time (t). In mathematical symbols, this relationship can be written as follows:

$$\tau = \frac{dL}{dt} \quad (1.14)$$

When there is no force acting on the system, the torque (τ) will be equal to zero, and as a result, the angular momentum (L) will remain constant.

In the presence of circular motion, the effect will be that the axis around which the system rotates will always attempt to align with the direction of rotation. Referring back to Figure 1.13, you can envision the moment of force pulling the vector representing angular momentum towards itself, thus inducing the rotation of the wheel.

The miniaturised gyroscopes, integrated into the MIMUs, depend on the Coriolis force, an apparent force that comes into play when an object moves on a rotating surface. From an external perspective, the object's path appears linear, but from a viewpoint tied to the rotating surface, which moves in tandem, the trajectory appears curved, as though influenced by a certain force. This phenomenon is known as the Coriolis force. The following equation defines mathematically the Coriolis force:

$$F_{Coriolis} = -2m(\omega \times v) \quad (1.15)$$

where m is the mass, ω the angular velocity of the object, and v the velocity of the mass relative to the object's motion. For example, consider a scenario where a mass is undergoing vibrations along the x-direction with a linear velocity v , and simultaneously, the gyroscope is undergoing rotation around the z-direction at an angular rate ω . In accordance with the Coriolis effect, the mass is also subjected to an apparent force that induces additional vibration in a direction perpendicular to the previous two, specifically the y-direction. The drift rate stands out as the most important parameter for gyroscopes, representing the occurrence where the gyroscope provides a nonzero reading when the anticipated value should be zero. Also, in the case of the gyroscopes, their output depends on the way they are mounted and on the motion they are subjected to.

Magnetometer

A magnetometer is a device that measures the magnetic field, specifically its magnetic strength and direction. The compass is the most popular magnetometer, which points in the direction of the Earth's magnetic north. It is possible to classify magnetometers into two categories: scalar magnetometers, which measure the magnitude of the magnetic field, and vectorial magnetometers, which detect the component along a certain axis and quantify the direction and strength of the magnetic field.

The measurement of the magnetic field components along its three axes provides for a univocal definition of the magnetic field vector at the measurement site. To obtain the magnetic field vector, a voltage proportional to its strength must be produced. It is based on the Lorentz force, which can be expressed with the equation:

$$F_L = q(v \times B) \tag{1.16}$$

where F_L is the Lorentz force, q is a charge moving with a certain speed v on a conductive surface with a constant magnetic field B is applied. The charge, driven by this force, starts moving transversally, causing the formation of an electric field E_{Hall} on the conductive surface, which results in the generation of an electric force, described in:

$$F = q(v \times B) + qE_{Hall} \tag{1.17}$$

In equilibrium conditions, it is possible to write the equation:

$$(v \times B) = -E_{Hall} \tag{1.18}$$

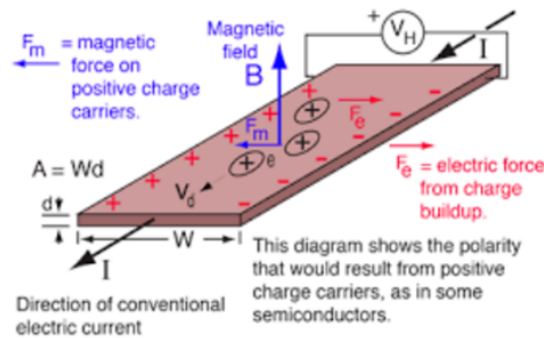


Figure 1.14: *Hall effect. Adapted from [27].*

The Hall effect, Figure 1.14, is the generation of a voltage differential (the Hall voltage V_H) across an electrical conductor that is transverse to an electric current in the conductor and perpendicular to an applied magnetic field. Magnetometers are particularly sensitive to ferro-magnetic disturbances, making them suitable for outdoor assessments but less for inside, where disturbances are more prevalent. Because of its shortcomings, the magnetometer is frequently neglected in gait analysis. In MIMUs, they are typically used in conjunction with gyroscopes and accelerometers. Just like the accelerometers and the gyroscopes, the output of the magnetometers depends on the position where they are mounted and on the motion performed.

Pressure insoles

Pressure insoles (PI) are devices used to measure and analyse the distribution of pressure on the feet during walking. They consist of thin, flexible sensor arrays that are inserted into the shoes, between the foot and the sole, and connected to a data acquisition system that records and analyses the pressure patterns [28]. Since they are portable and inexpensive, in-shoe instrumented devices are growing in popularity in the gait analysis field.

Capacitive, resistive, and piezoresistive sensors are some of the several types of pressure insoles. Resistive sensors rely on changes in resistance to detect pressure, whereas capacitive sensors assess changes in a thin film's capacitance in reaction to pressure. Piezoresistive materials, which are what are used in piezoresistive sensors, vary their resistance in response to pressure [29].

Several studies have been done to assess the precision and dependability of pressure insoles. According to research that examined various pressure insole types, capacitive insoles offered the most precise and dependable measures of pressure distribution while walking [29]. Further research [30] that utilised pressure insoles to

evaluate how footwear affected pressure distribution while walking discovered that soft-soled footwear reduced pressure under the forefoot and heel whereas hard-soled footwear raised pressure under the forefoot and midfoot. Running is a much more dynamic exercise than walking; thus, insoles experience higher pressure levels. This results in a faster degradation compared to their use during simple walking[31].



Figure 1.15: *Pressure Insoles from the INDIP system [32].*

A novel form of pressure insole with only sixteen sensing components was recently developed by Salis *et al.* [33]. These insoles have proven to be beneficial for gait analysis, enabling accurate temporal parameter estimations. These sensing components are built on force sensing resistors, which display resistance that is inversely proportional to the applied force. Next, voltage is created from the resistance. These PI have been validated for characterising gait by integrating them with MIMUs as part of a multi-sensor wearable system [32]. In Figure 1.15 are shown the pressure insoles from a multi-sensor system called the INertial module with DIstance Sensors and Pressure insoles (INDIP).

Chapter 2

State of the art for the estimation of running spatio-temporal parameters

2.1 Spatio-temporal parameters computation pipeline

Spatial parameters have been obtained using MIMUs via one of the following approaches: biomechanical models, machine learning methods, or integration methods.

- The biomechanical models are based on known models of human movement analysis. These methods could achieve good accuracy for calibrated cases and users. Therefore, they require distinct mathematical models from subject to subject and as the movement speed varies. Moreover, a calibration stage is needed for different subjects. They are useful for well-defined use cases: a known user and specific kinds of motion [34].
- The machine learning methods have the fundamental weakness of exhibiting considerable inter-subject variability, which implies that they need some degree of individualization [35].
- The integration methods reckon on a double integration of the gravity-removed acceleration. The first integration computed the velocity of the sensor over time, followed by the second integration, which resulted in the position of the sensor over time [35].

The third method is typically used to determine the displacement of the MIMU in gait analysis.

It can be stated that the computational pipeline for spatial parameter analysis in gait analysis is well-established [36]. The procedure of integration is frequently accompanied with drift, mostly caused by thermal-mechanical and electronic noise, which leads to an inaccuracy in the displacement estimates. It is beneficial to segment the signal such that it is not integrated throughout the entire length since the drift gets worse over time. It is also preferred that the period of integration time be shortened in order to take advantage of the cyclical nature of gait (or running gait) and avoid the adverse consequences of drift. On the other hand, this necessitates the detection of a known velocity moment in the cycle to be employed as the starting condition in the acceleration integration.

There exist multiple techniques to address the various steps, and these will be outlined in this section, describing both walking and running procedures. Determining spatial parameters from sensor signals during running can be considerably more difficult than during walking. In running, participants and the sensors affixed to them experience more pronounced movement, leading to significant accelerations and rapid shifts in sensor orientation. Notably, the intense impacts when the feet touch down during running can pose an additional hurdle for the double integration processes of acceleration that are frequently employed [37]. The situation becomes even more challenging when it comes to sprinting at higher speeds. The section that follows is an outline of the spatial parameter's computation pipeline utilising the MIMU.

2.1.1 Orientation estimation and gravity removal

Orientation estimation

The orientation of an object can be described in various ways, such as Direction Cosine Matrix (DCM), Euler angles, and Quaternions. DCM, which involves nine parameters, can be challenging to implement. Euler angles can suffer from gimbal lock issues, however, graphically, they are easy to interpret. Quaternions, with fewer parameters, give an effective mathematical notation for representing orientations and rotations of any objects for every dimensions. This stage involves determining the orientation or attitude of the MIMU sensor with respect to the Earth's coordinate system. To estimate the sensor's orientation in terms of pitch, roll, and yaw angles, sensor fusion algorithms that employ accelerometer, gyroscope, and magnetometer data can be used. In fact, individually, the MIMU's sensors are insufficient to deliver an accurate assessment in every scenario.

The accelerometer is unable to discern the difference between the acceleration caused by gravity and the external acceleration of the body. As a result, the accelerometer can only report sensor inclination information if gravity is the only acceleration present, which occurs when the body is stationary or heading at a

constant speed. Additionally, due to an accelerometer's information depended on the direction of gravity, it is unable to detect rotation around the vertical axis.

The gyroscope has significant biases that cause drift. In order to produce the orientation variation with regard to the beginning instant, it gives a 3D angular velocity with respect to the MIMU coordinate system that can be incorporated. Considering this, an absolute orientation could not be obtained by the gyroscope. Since the signals are impacted by biases and white noise, which cause a drift error that grows larger over time, it is impractical to estimate the orientation only using the gyroscope, especially if the utilised gyroscope is relatively cheap. Estimate mistakes are a result of biases, and they increase linearly with time. The accuracy of the gyroscope's relative orientation calculation degrades with longer integration times.

The magnetometer is heavily sensitive to ferromagnetic disturbances which would lead to unpredictable information. These problems are addressed by sensor fusion algorithms to estimate the orientation of the segment to which the inertial sensor is mounted more precisely. The basic concept is to remove one's weakness using other's strengths. A lot of sensor fusion algorithm have been developed over the years to mitigate the errors that occur in the estimation of the orientation. The sensor fusion algorithms frequently rely on mathematical techniques like Complementary Filters (CFs) and Kalman Filters (KFs). The CFs employs a very simple method that just needs less computing and is simple to implement. It is preferred for embedded systems because of this capability. Part of these algorithms have been developed directly for the human motion applications. The most popular CF algorithm is the Madgwick's one [38]. Iterative filters like the KF are effective but have a high computational complexity. The minimal memory need of the KF is a benefit. It works by correlating between current and predicted states[39].

Complementary Filters

Accelerometer, gyroscope, and magnetometer are incorporated in the MIMU. The primary sensors are the gyroscope and the accelerometer, while the correction sensor is the magnetometer. The accelerometer measures every force acting on the item, and because even minor forces can cause measurement errors, long-term measurements are accurate. Therefore, a low pass filter is required for correction in an accelerometer. High pass filter is required for gyroscopic data rectification because the integration process used in gyroscopic sensors takes place over time and results in long-term value drift. The CF was used to obtain exact data since it is simpler to build and comprises of both a low pass and a high pass filter [39].

There are different CFs algorithms that differs in how the information from accelerometers and magnetometers is used to correct the orientation drift due to angular rate integration. CFs demand minimal computational resources and

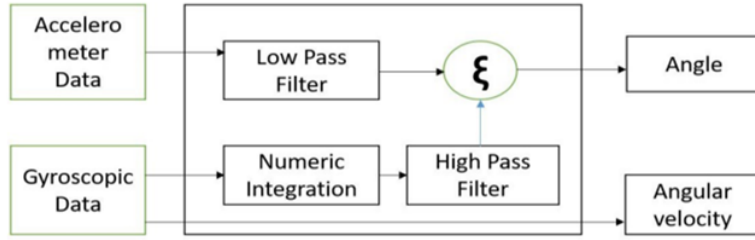


Figure 2.1: Block Diagram of complementary filter, from [39].

are typically characterized by their relative simplicity due to the reduced number of configuration parameters. They can also be executed on microprocessors integrated with MIMU [40]. However, since these methods rely on mathematical approximations of real-world behaviour, they inherently contain some degree of error.

Kalman Filters

Kalman filters (KFs) were proposed as an innovative stochastic approach of sensor fusion applicable in many fields [41]. KFs employ a stochastic method to a probabilistic determination of the outcome. This method attempts to get over the limitations of determinism. Since mathematical models are never perfect but simply approximations of reality, disturbances cannot be represented deterministically since some parameters relate to a certain amount of uncertainty. The goal of this technique is to replace the deterministic variables in the system with probability distribution functions. The KF operates by repeatedly correlating the observed and expected conditions. The system's present state is utilized to predict its future state. Since dynamic systems are always changing, KFs can be a good way to predict the future state with some degree of accuracy. The initial first state must be specified since the filter estimates future states based on the past ones[39]. KF uses correlation between prediction and what actually happened to make the prediction error. An advantage of KF is its memory is low, so it cannot save nothing but the previous value.

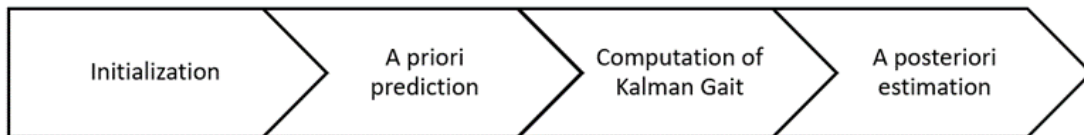


Figure 2.2: Diagram of Kalman filter steps.

The procedure is divided into four steps, depicted in Figure 2.2. Firstly, the

initial value is given, then the prediction step (a priori prediction), computing gain of the filter and then estimation is done (a posteriori estimate). At last, it calculates the error covariance[39].

There are different typologies of KFs, the main ones are the Linear KFs and the Extended KFs (EKF).

The Linear KF is used to assess the state of a linear dynamic system in the presence of noise. As new observations become available, it updates its estimates sequentially since it acts in a recursive manner. The state estimate and the error covariance matrix are the filter's two primary components. Based on the dynamics of the system, the filter predicts the subsequent state and combines these predictions with actual measurements to enhance the state estimate. When dealing with linear system dynamics and Gaussian noise, the KF is quite useful. In terms of the mean squared error criteria, it offers the best approximation of the system state[42].

The EKFs is a KF extension that may be used with nonlinear dynamical systems. Systems are frequently not strictly linear in real-world situations, and nonlinear functions can better capture the dynamics. To make these nonlinear functions suitable for the traditional KF architecture, the EKF linearises them using Taylor series expansion. The EKF functions similarly to the Linear KF but updates the state estimate and error covariance matrix using linearised dynamics. Despite being often employed for nonlinear systems, the EKF has certain drawbacks, such as the presumption that the system's uncertainty can be precisely represented by a Gaussian distribution even after nonlinear changes[42].

Comparison between Complementary Filters and Kalman Filters

According to [43], the key benefits of CFs are their reduced computational cost and the ability to fine-tune just one or a few parameters, whereas the strengths of KFs relate to the algorithm's flexibility, which gives more latitude in the development of state and noise models. Furthermore, because they are recursive filters, KFs are suitable for scenarios that call for estimates every time a new measurement becomes available. Since the KF just saves the prior value, it has the benefit of requiring relatively little memory and, in many situations, being more accurate than CFs [39]. KFs, on the other hand, need extensive parameter tweaking, significant computational expense, and complexity. The linear regression iterations, fundamental to the Kalman process, demand sampling rates which can far exceed the subject motion bandwidth[38]. Considering their advantages of simpler implementation and lower computational costs, CFs appear to be a viable option and are thus preferred in the context of embedded systems [39].

Gravity removal

Since the accelerometer signals are referenced by the sensor's coordinate system, they must be represented in terms of the world coordinate frame in order to be able to subtract the vector gravity from the signals. Thus, to transform the global reference, the accelerometer data are rotated by quaternions. In a world coordinate system, gravity is described as a vector with a z component of 9.81 m/s^2 . To isolate the linear acceleration associated with motion, the gravity component must be subtracted from the accelerometer results. This process allows dynamic acceleration information to be extracted.

$$a^G(t) = a_W(t) - \begin{bmatrix} 0 & 0 & 9.81 \frac{\text{m}}{\text{s}^2} \end{bmatrix} \quad (2.1)$$

Where $a^G(t)$ is the gravity-free acceleration in the global frame and $a_W(t)$ is the raw acceleration in the global frame.

2.1.2 Zero Velocity Update (ZUPT)

In gait analysis, the motion information acquired from MIMU mounted on the feet is crucial for understanding individual gait cycles. However, this application faces a common challenge related to inertial navigation: unbounded errors in position and velocity due to sensor artefacts. Typically, low-cost inertial navigation systems (INSs) exhibit a position error that increases proportionally to the cube of the operation time. This means that, with the current performance of low-cost inertial sensors, free inertial navigation is only feasible for short time intervals, usually on the order of a few seconds.

To address this issue, constraints can be imposed on the navigation solution by utilising information about the dynamics of the system. One common approach is to take advantage of knowledge about the time intervals when the system is in a stationary phase, maintaining a constant position and attitude. This strategy, known as "zero-velocity updates" (ZUPT), is effective in limiting error growth, as during ordinary gait, the foot periodically returns to a stationary state [44].

The implementation of ZUPT can vary depending on the specific application but is generally classified as either "hard" or "soft" updates. In foot-mounted inertial sensor-based pedestrian navigation systems, where the accumulated motion of the foot over multiple steps is of interest, "soft" ZUPT are commonly used. This approach combines information about when the system experiences zero velocity with a model that predicts how position, velocity, and attitude errors evolve over time. These estimates of accumulated errors are then used to correct the navigation solution and calibrate the navigation algorithm[45]. Conversely, in gait analysis, where the focus is on the motion of the foot during individual gait cycles rather than the cumulative motion over multiple cycles, "hard" ZUPT

are more typical. These updates are considered "hard" because they reset the position, velocity, yaw, roll, and pitch to zero when the system undergoes a ZUPT[46].

The estimation of spatial parameters frequently employs an inertial navigation system (INS) that applies a ZUPT, and it makes use of the fact that the foot is typically stationary during normal gait to limit the rise of the system's position inaccuracy. The determination of the time epochs during which the MIMU is stationary (and therefore that the speed is close to zero) is necessary for the usage of ZUPT[47]. The ZUPT is widely used in gait analysis.

There are contrasting viewpoints and it is frequently stated in articles that studying for the ZUPT exam for the course requires in-depth research. For example, Zrenner *et al.* [35] claims that the assumption of stationarity may not hold during running at high speed. However, Ruiter *et al.* [37] affirms that even in maximal sprinting there is a short time window in the early stance phase (during amortisation) immediately following touch-down, where sensor velocity will be (close to) zero and therefore stationarity can be assumed.

2.1.3 Double integration and Drift Removal

The gravity-free acceleration signal in world coordinates $a^G(t)$ needs to be integrated twice with respect to time to estimate the foot's displacement.

$$v(t) = \int_0^t a^G(t)dt + v_0 \tag{2.2}$$

$$x(t) = \int_0^t v(t)dt + x_0 \tag{2.3}$$

However, these estimates are corrupted by a drift. To mitigate this, the acceleration is not integrated throughout the entire recording period but only within a restricted interval based on the integration points identified. The recognition of the ZUPT intervals is essential for determining the integration points. Following a review of the literature, three distinct methods for defining the integration moment were identified. The first approach selects the integration points as the ZUPT interval's midpoints[48]. Rossanigo *et al.* identify the ZUPT interval's end as the chosen instants of integration[36]. Finally, the last method involves selecting the minimum of the kinetic energy within the ZUPT interval [49]. Additionally, the velocity is adjusted by enforcing it to be zero during each flat foot period interval.

Drift Removal

The displacement estimations are inaccurate due to drift, which is mostly brought on by thermal-mechanical and electrical noise. To overcome this problem, there is a need to enhance the accuracy of double integration. Various solutions have been adopted in the literature to mitigate this problem. Many authors employ the Linear De-drifting approach. After the correction performed with ZUPT, there will still be some drift between resets. Assuming a constant bias in each of the accelerometer axes allows to define the velocity drift. At this point, it is possible to apply linear de-drifting to the resultant velocity because constant bias in acceleration causes a linearly rising inaccuracy in velocity after integration[50].

$$v(t) = \int_{t_0}^{t_1} (a(t)dt + v_0) - d_v(t) \quad (2.4)$$

Where, $d_v(t)$ is the estimated drift. After that, position is determined by integrating the de-drifted velocity signal.

Another drift removal technique is the subtraction of the mean of the acceleration that theoretically lead to the same results as the Linear De-drifting approach.

Zok *et al.* [51] implemented a method that involves not only direct integration but also a time-reversed integration (referred to as reverse integration). As a result, this integration technique is called Direct and Reverse Integration (DRI). The acceleration signals used in this process are both gravity-compensated and mean-compensated. The DRI consists of three phases:

- **Direct Integration:** the signal is double integrated ($d(t)$)
- **Reverse Integration:** the original signal is integrated inversely in time using reverse double integration ($r(t)$)
- **Weighting:** time-dependent weight function $w(t)$ varying from 0 to 1 is used to weight the sum of the two integrated curves.

The final integrated displacement is:

$$DRI(t) = r(t)w(t) + d(t)(1 - w(t)) \quad (2.5)$$

where w is the weighting function which is forced to vary from 0 to 1 as follows:

$$w(t) = \frac{s(t) - s(t_B)}{s(t_E) - s(t_B)} \quad (2.6)$$

where $s(t)$ is a function chosen in order that in the middle of the interval $(t_E - t_B)$, the weighting function is equal to 0.5 and is symmetric with respect to the central point such as the weight is evenly distributed between $d(t)$ and $r(t)$.

Since the inaccuracy introduced by the noise existing in the original signal into the double integration increased with time, samples of the double integrated signal that were closer to t_B were more dependable than those closer to t_E . The simplest form of $s(t)$ would be a linear function ($s(t) = t$) but an "s-shaped" function such as the following perform better:

$$s(t) = \tan\left(\frac{1}{\beta} \frac{2t - t_E}{2t_E}\right) \quad (2.7)$$

where the β factor controls the steepness of the "s-shaped" curve. The value $\beta = 0.1$ was suggested by the author as a satisfactory trade-off between a discontinuous step function (when β tends to 0) and a quasi-linear function (when β is greater than 1).

2.1.4 Estimation of Stride Velocity and Stride Length

The parameters of interest are defined stride by stride. In this study, these parameters are defined in the x-y plane for each i -th stride.

The stride velocity (SV) is defined as the norm of the antero-posterior and medio-lateral components of velocity (v) obtained from the integration of the acceleration between two Mid-stance instants:

$$SV_i = \sum_{n_i} \sqrt{v_x(n)^2 + v_y(n)^2} \quad (2.8)$$

The stride length (SL) is defined in the same manner as the SV, but it utilises the displacement (d) obtained from the double integration of acceleration:

$$SL_i = \sqrt{endDisplacement_{x_i}^2 + endDisplacement_{y_i}^2} \quad (2.9)$$

where n is the sample number of the i -th stride.

2.2 Issues and Challenges

As was already established, the greater movement in motions makes everything more difficult when it comes to running analysis. In this section, the main issues and challenges to address in order to obtain a reliable estimation of spatial parameters during running action will be summarised following the pipeline order described above.

The primary obstacle is encountered in the estimation of orientation. If the estimated orientation is not correct, it could be difficult to isolate the linear acceleration associated with motion from the acceleration data. The gravity

component must be subtracted from the accelerometer results in order to proceed to the next step of the pipeline and perform the integration. If gravity cannot be effectively removed, then it gets integrated, leading to incorrect values of velocity and displacement. The sensor fusion algorithms used for orientation estimation involve numerous parameters that need to be configured through experimentation. These parameters have a significant impact on performance.

Moreover, there is a lack of clarity in the literature regarding the utilisation of the various existing zero-velocity detectors in the analysis of running. In fact, the performances of ZUPT detectors are often tested for specific running speeds, and their generalisability for different running paces is overlooked. Regarding this matter, for fixed-threshold methods, finding this threshold can be challenging due to the variability present among running speeds. Also, the search for this threshold incurs a high time cost.

Also, there is no uniformity in the literature regarding the choices of integration instants for the double integration that has to be used.

The real integration mechanism of acceleration presents another challenge to be faced. At this point, drifting brought on by thermal, mechanical, and electrical noise is a serious problem. The ideal method needs to be discovered in order to reduce drift's impact on the estimation of the parameters of interest.

Chapter 3

Materials and Methods

3.1 Experimental protocols

3.1.1 Amateurs protocol - 14 km/h

Ten male participants (all male, age: 32.3 ± 9.9 years, height: 172.5 ± 4.3 cm, weight: 69.4 ± 4.9 kg, shoe size: from 38 to 42 (EU)) were enrolled. Every participant was required to do different 90-second treadmill running trials at 14 km/h with 8 different shoe models. The subjects were required to meet the following criteria:

- between the ages of 18 and 50 years old;
- recreational rearfoot striker runners;
- familiar with the treadmill system;
- injury-free for at least three months preceding the acquisition;
- able to run effortlessly for 55 minutes.

Each subject wore a foot-mounted MUMU (mod: Opal v2, APDM, Portland, USA. Technical specifications: 3D accelerometer range is up to ± 16 g, 3D gyroscope range is up to ± 2000 $^\circ$ /s, 3D magnetometer range is up to ± 8 Gauss. [52]), sampling at 200 Hz, attached to the feet's arches above the shoes with a strap, as well as retro-reflective markers from the stereophotogrammetric system, which was the gold standard ([53] - [54]). In Figure 3.1, an example of equipment is shown.



Figure 3.1: *Subject wearing an inertial sensor on the instep of each shoe, below the red tape, and retro-reflective markers.*

3.1.2 Sprinters protocol - from 19 km/h to 29 km/h

Data collection for the sprinters occurred on an official outdoor running track. Seven injury-free senior category track and field athletes, specialised in the discipline of running and engaging in a minimum of three training sessions per week, were recruited for the study (5 male and 2 female, age: 22.4 ± 2.1 years, height: 174.4 ± 8.1 cm, weight: 65.9 ± 13.2 kg, shoe size from 38 to 45 (EU)). After a period of warming up, each athlete was asked to perform fifteen 50-meter sprint trials along the lane of an official track at their maximal speed. The averaged speeds over the 50-m path ranged from 19 km/h to 29 km/h. All participants wore an INDIP multisensory system [32] sampled at 200 Hz. The INDIP MUMU has the following technical specifications: 3D accelerometer range is up to ± 16 g, 3D gyroscope range is up to ± 2000 $^\circ$ /s, 3D magnetometer range is up to ± 50 Gauss. The MUMU was attached to the shoelaces of each shoe, while the pressure-sensitive insoles (mod. YETI, 22le Srl, Padua, Italy, eight pressure sensors; element area = 310 mm; force threshold = 5 N) were inserted in the shoes.

The pressure insoles were considered the gold standard for temporal events ([33],[54],[55],[56]). In the setup, there was also a sensor attached to the lower limb, which was not used in this study. In Figure 3.2, an example of wearable equipment is shown.

For each trial, a video was recorded using a GoPro HERO10 (sampling frequency equal to 240Hz), enabling a resolution of 2.7k (2704 by 1520 pixels) at a wide angle.

The athletes ran for 50 metres, but only the last 40 metres were captured by the camera. The camera was positioned 20 metres from the finish line and displaced transversally by 15 metres, as depicted in Figure 3.3. The timing was measured via video and via a hand chronometer. The MUMUs system and the video recordings were synchronised.

The video recording was used as a gold standard for spatial parameters.

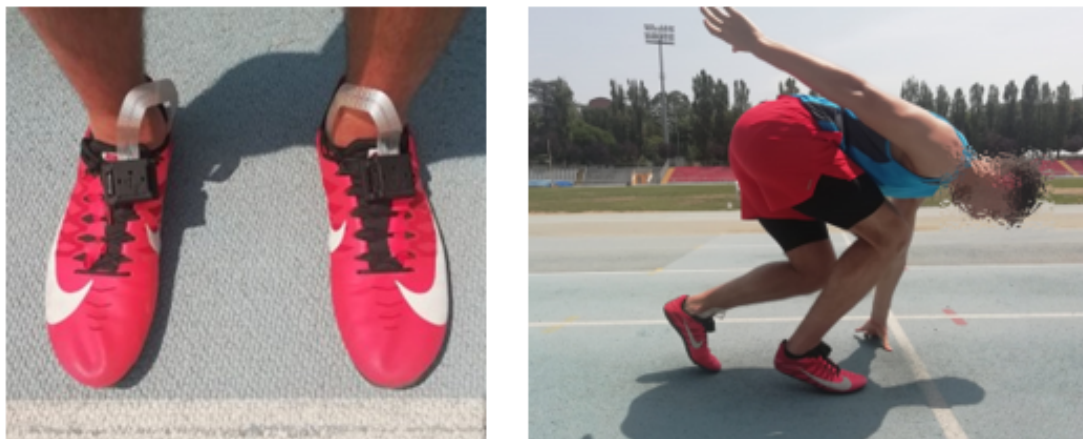


Figure 3.2: Subject wearing INDIP system including a MUMU and a pressure insole per shoe.

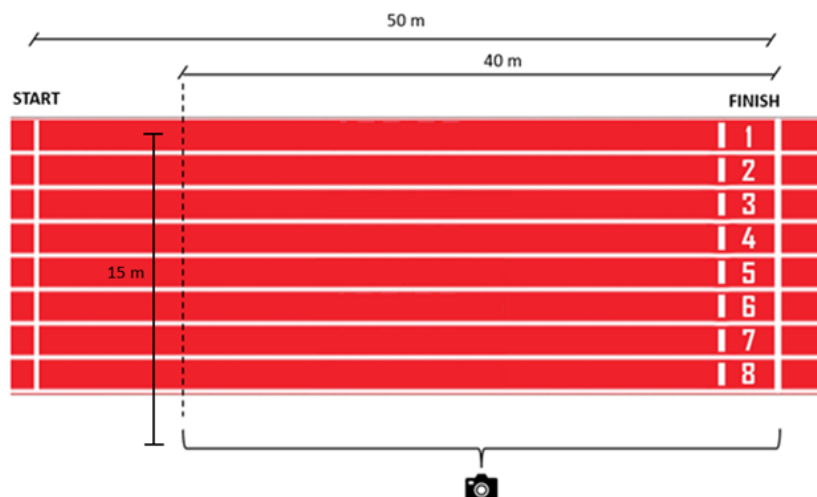


Figure 3.3: Camera placement scheme.

3.2 Spatio-temporal parameter estimation with a non-optimised pipeline

In this section, a schematic representation of the baseline pipeline for the estimation of stride velocity and length is provided. The stages of the pipeline [36] applied to the MIMU data are:

- Realignment of the z-axis along the gravity: to ensure independence from

the subject’s positioning and the type of footwear, the z-axis of the MIMU sensor is realigned along the gravity direction when the subject is in an initial standing phase.

- **Zero-velocity Updates (ZUPT)**. It is necessary to integrate acceleration over a shorter interval compared to the total recording period. This is achieved by identifying a range in which the foot’s velocity is presumed to be zero, corresponding to when the foot is in contact with the ground. Within this interval, specific instants for integration are selected. This technique is known as Zero-Velocity Update (ZUPT), and its purpose is to correct any accumulated errors over time. The zero-velocity detector captures the stationary state of the MIMU if a specifically defined function T , based on angular rate and/or accelerations, is less than the detection threshold γ ($T < \gamma$). In the baseline pipeline, reported in orange in the dashed box in Figure 3.5, the ZUPT intervals were investigated using the fixed threshold Angular Rate energy Detector (ARE) implemented by Skog *et al.* ([13],[32]) and the **identification of the integration instants** for the double integration of the acceleration was computed at the 50% of the ZUPT interval found using the ARE method ([48]).
- The **estimation of the orientation** was performed using the Madgwick’s algorithm with the Valenti’s initialisation algebraic quaternion and relied on the selection of an adequate β value, that for the baseline pipeline was of 0.0019 rad/s ([36],[38],[57]).
- **Stride-by-stride double integration of the gravity-free acceleration** led to the estimation of the Spatio-parameters of interest:

$$v(t) = \int_0^t a^G(t)dt + v_0 \quad (3.1)$$

$$x(t) = \int_0^t v(t)dt + x_0 \quad (3.2)$$

the residual drift removal is accomplished using the direct and reverse integration (DRI) ([36],[51]).

- The estimation of stride velocity and stride length in this work was performed referring to the local sensor frame at the first frame of the running trial (t_0) (Figure 3.4).

The stride velocity (SV) and the stride length (SL) were calculated on the the horizontal x_0 - y_0 plane for each i -th stride:



Figure 3.4: Exemplary diagram highlighting the first frame of the running trial (t_0).

$$SV_i = \sum_{n_i} \sqrt{v_x(n)^2 + v_y(n)^2} \quad (3.3)$$

$$SL_i = \sqrt{endDisplacement_{x_i}^2 + endDisplacement_{y_i}^2} \quad (3.4)$$

where n is the sample number of the i -th stride.

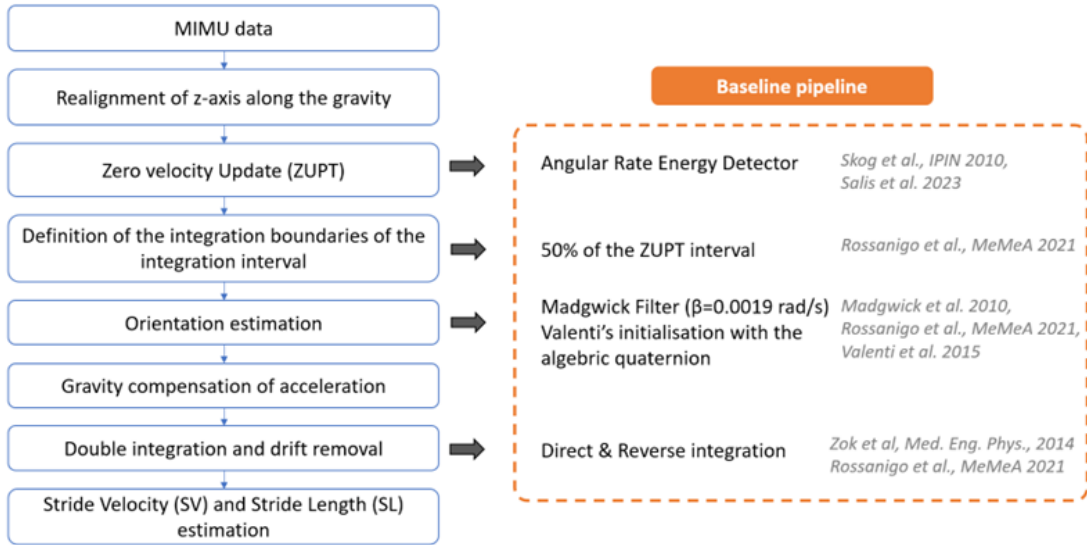


Figure 3.5: Block diagram summarising the stages of the pipeline, explicitly showing, on the right, the algorithms employed in the baseline pipeline.

Figure 3.5 summarise the stages of the pipeline emphasising the algorithm used in each phase in the baseline.

3.3 Optimisation of the state-of-the-art methods for the estimation of running stride velocity and stride length

This section describes all the methods implemented and investigated in this thesis, optimising each stage of the pipeline.

At each optimisation step, the other methods and associated parameters of the pipeline remained constant, as in the baseline. However, the optimal options that were found were applied to each subsequent decision.

The minimisation of errors in stride velocity and stride length was used as the criterion for choosing the algorithm to optimise the pipeline.

3.3.1 Zero Velocity detectors

The initial investigation focused on determining the most suitable detector for ZUPT for running analysis. There is a lack of clarity in the literature regarding the utilisation of the various existing detectors in the running context. In fact, the performances of ZUPT detectors are often tested for specific running speeds, and method generalisability for different running paces is overlooked ([58], [54]). Although there are several detectors used in gait analysis, not all of them are employed in the analysis of running gait. In this study, each detector found in the literature was implemented and compared, applying them to different types of running [59]. In this section, there is a comprehensive list of the different types of detectors that are used for the analysis of walking and/or running.

In general, the zero-velocity detector captures the stationary state of the MIMU if a specifically defined function T is less than the detection threshold γ :

$$T < \gamma \tag{3.5}$$

To determine whether the MIMU is stationary from the output of the accelerometers or gyroscopes, a variety of detectors have been presented in the literature. The goal of the zero-velocity detector is thus to identify, given the measurement sequences, whether the MIMU is moving or stationary during a period consisting of $W \in N$ observations between the time instants n and $n + W - 1$. The equations of the detectors present in the literature are listed, where $y_n^a \in \mathbb{R}^3$ denote the measured specific force vector and angular rate vector at time instant $n \in N$, respectively.

Below the formulas for the T functions of the various detectors are reported:

- **Stance Hypothesis Optimal Detector (SHOE)**, that based on accelerations and angular velocities:

$$T = \frac{1}{W} \sum_{k=n}^{n+W-1} \frac{1}{\sigma_a^2} \|y_k^a - g \frac{\bar{y}_n^a}{\|\bar{y}_n^a\|}\|^2 + \frac{1}{\sigma_\omega^2} \|y_k^\omega\|^2 \quad (3.6)$$

- **Angular Rate Energy Detector (ARE)**, that considers only angular velocities:

$$T = \frac{1}{W} \sum_{k=n}^{n+W-1} \|y_k^\omega\|^2 \quad (3.7)$$

- **Acceleration Moving Variance Detector (MV)**, that relies only on accelerations:

$$T = \frac{1}{W} \sum_{k=n}^{n+W-1} \|y_k^a - \bar{y}_k^a\|^2 \quad (3.8)$$

- **Acceleration Magnitude Detector (MAG)**, that considers only accelerations:

$$T = \frac{1}{W} \sum_{k=n}^{n+W-1} (\|y_k^a\| - g)^2 \quad (3.9)$$

where $\sigma_a^2 \in \mathbb{R}^1$ and $\sigma_\omega^2 \in \mathbb{R}^1$ denote the variance of the measurement noise of the accelerometer and gyroscope, respectively. Moreover, $\|a\|^2 = a^T a$ and \bar{y}_n^a denotes the sample mean, i.e.,

$$\bar{y}_n^a = \frac{1}{W} \sum_{k=n}^{n+W-1} y_k^a \quad (3.10)$$

The noise variances σ_a^2 and σ_ω^2 were taken into account only for the SHOE detector, which depends on both accelerations and angular rate. The ratio shows the differences between the information from the gyroscopes and accelerometers when there are disturbances. The above-mentioned detectors exploit the information of inertial signals. However, it is possible to combine the information obtained from the accelerometer and from the gyroscope with the output of a pressure insole, as proposed in [60]. The T function in this case adds a parameter to the SHOE detector, as is shown in the following equation:

$$T = \frac{1}{W} \sum_{k=n}^{n+W-1} \frac{1}{\sigma_a^2} \|y_k^a - g \frac{\bar{y}_n^a}{\|\bar{y}_n^a\|}\|^2 + \frac{1}{\sigma_\omega^2} \|y_k^\omega\|^2 + \frac{1}{\sigma_\rho^2} \|y_k^\rho - \rho_{max}\| \quad (3.11)$$

where $\sigma_\rho^2 \in \mathbb{R}^1$ is the noise variances of the pressure sensor, $y_k^\rho \in \mathbb{R}^3$ is the pressure at time k and ρ_{max} represents the maximum value reached by the pressure sensor.

Table 3.1: *Threshold values for the ZUPT detectors.*

Detectors	Units of measurement for function T	Thresholds for 14 km/h	Thresholds for 19-29 km/h
SHOE	$(m/s^2)^2 + (deg/s)^2$	7	15
ARE	$(deg/s)^2$	$0.3 * 10^5$	$0.5 * 10^5$
MV	$(m/s^2)^2$	0.002	0.004
MAG	$(m/s^2)^2$	0.5	1

Each detector had a different threshold, as the function T that is calculated considers different variables depending on the mathematical expression. These thresholds are strongly influenced by running speed. The optimal threshold value was determined through iterative trial-and-error approaches. The values found for both datasets via iterative method are reported in the Table 3.1.

It should be noted that employing a fixed threshold for ZUPT detection might carry the risk of either missing some support phases or incorrectly identifying support phases when they are not present. Moreover, the threshold γ is determined through numerous trials dependent on variables like speed, subject characteristics, and specific situations. Threshold-based approaches can be sensitive to differences in gait patterns, running surfaces, sensor placement and running speed.

Therefore, Rossanigo *et al.* [36] proposes a parametric method based on gyroscope energy to detect ZUPT events in gait analysis. This new method seeks segments within the support phase with the lowest mean value of the T function to define quasi-ZUPT intervals. Since the probability of the foot's support phase occurring is very low in the first or last 10% of the support phase, these segments are discarded. Within the remaining part of each support phase, a moving average of the T function is calculated, and a sliding window is used to find the interval corresponding to the lowest mean value of the T function. This interval becomes the quasi-ZUPT interval. The length of the sliding window is set to 30% of the entire support phase[36]. In summary, this method offers better adaptability to individual variations.

This parametric method developed for gait analysis was optimised for running analysis. In running analysis, it is possible to adjust the length of the moving window used to search for the minimum of the function T since the speed in running is higher respect to walking. In fact, the length of the sliding window has been reduced compared to the original method because a shorter ground contact phase is expected. This optimisation is a crucial aspect of the algorithm, as running dynamics differ from walking and require parameter adjustments for accurate results.

Following a thorough review of the literature, it can be asserted that for running

analysis, the most widely employed ZUPT detectors are the one based on angular velocity, denoted as Angular Rate Energy detector (ARE), and the approach that combines accelerometer and gyroscope information, referred to as Stance Hypothesis Optimal Detector (SHOE). Furthermore, there is evidence of the utilisation of the Acceleration Magnitude Detector (MAG) detector and the approach that combines inertial signals with pressure signals. However, the Acceleration Moving Variance Detector (MV) method and the parametric threshold-based approach from Rossanigo *et al.* [36] have not been employed in running analysis.

Table 3.2: Overview of the literature on the use of the ZUPT detectors in running analysis.

Detectors found in literature	Use in running analysis
SHOE	Brahms <i>et al.</i> [3] Wang <i>et al.</i> [61] Bailey <i>et al.</i> [50] Zrenner <i>et al.</i> [35].
ARE	Li <i>et al.</i> [62] Zhang <i>et al.</i> [63]
MV	-
MAG	Ren <i>et al.</i> [64]
Parametric method	-

Checks on ZUPT Intervals

The ZUPT intervals found by threshold-based detectors were double-checked. Indeed, various inspections were performed to refine the start and stop instants for ZUPT intervals during running analysis to improve the reliability [32]. Firstly, an inspection was performed to determine whether there was at least one ZUPT interval between two consecutive swing phases. If not, a ZUPT interval was inserted in the middle of the gap. The subsequent check performed involved evaluating the temporal distance between successive start and stop instances of the same ZUPT interval to avoid excessively brief durations. Moreover, ZUPT intervals were synchronised with corresponding initial contact (IC) events. This alignment ensures that ZUPT intervals match the runner’s gait cycle accurately. Overall, these checks were performed to fine-tune the ZUPT intervals, ensuring that they accurately captured the periods of zero velocity during running.

Validation on ZUPT Intervals

To test the accuracy of the ZUPT detectors, the two type of available reference instrumentations, SP and PI data, were employed to provide high-precision reference data for comparison, being silver standard in this analysis. After a visual inspection, the percentage of overlap (ZUPT overlap %) between the estimated MIMU-based ZUPT intervals and the ones obtained with the silver standards was performed. The ZUPT overlap % was estimated as the intersection between the ZUPT intervals obtained with the silver standards and the MIMU-based ZUPT estimated with the detectors.

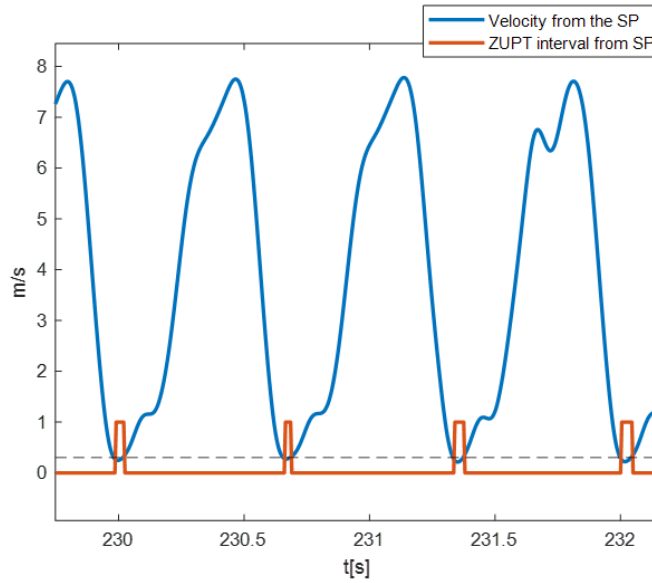


Figure 3.6: *Extraction of the ZUPT intervals from the SP.*

Comparison with stereophotogrammetric system

For the validation of ZUPT intervals using data obtained from SP the velocity norm of the markers attached to the foot-mounted MIMU was calculated. The goal was to identify the instants of stationarity as the intervals in which the velocity norm was below an arbitrary threshold. Brahms *et al.* defined the value of this threshold at 0.2 m/s [3] (Figure 3.6).

Comparison with pressure insoles

For the validation of ZUPT intervals using data obtained from sensitive-pressure insoles, a pressure-based detector was implemented following the one proposed by

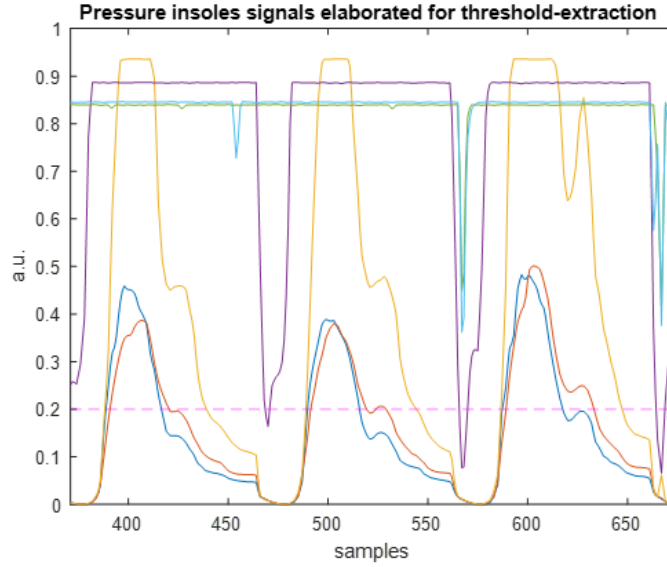


Figure 3.7: Extraction of the ZUPT intervals from the PIs.

Ma *et al.* [60]:

$$T = \frac{1}{\sigma_\rho^2} \|y_k^\rho - \rho_{max}\| \quad (3.12)$$

The reference ZUPT interval is defined where the elaborated pressure signals that form the function T are less than the threshold γ (0.2 a.u.). During the zero velocity intervals, $\|y_k^\rho - \rho_{max}\|$ is nearly zero, while it assumes a substantial value during motion intervals (Figure ??).

ZUPT instants

The majority of studies using foot-worn MIMUs to estimate stride velocity and/or stride length reduce the integration interval to a single stride defined by two consecutive ZUPT instants, hence minimising signal drift [37].

3.3.2 Selection of integration boundaries

The recognition of the ZUPT interval is essential for determining the integration points. In this work four definitions of the ZUPT instants were implemented. The first approach selects the integration points as the ZUPT interval's midpoints [48]. In the second one, Rossanigo *et al.* identify the ZUPT interval's end as the chosen instant of integration [36]. Finally, the last method involves selecting the minimum of the function T within the ZUPT interval [49]. Furthermore, a new proposed

method involves selecting the integration instant corresponding to the minimum of the moving average of the gyroscope norm within the ZUPT interval. This assumes that if the angular rate norm is sufficiently low, then it is possible to assume the foot stationarity. The selection of integration intervals is advantageous because it serves the purpose of evaluating stride-by-stride parameters. These intervals are crucial not only for resetting orientation but also as endpoints for integration, both from acceleration to velocity and from velocity to displacement.

3.3.3 Orientation estimation and gravity removal

The quaternions have been selected as the preferred method of representing the orientation since they need few parameters and are more effective in 3-D representation of orientation.

According to Section 2.1.1, in the comparison of the complementary filters (CFs) and the Kalman filters (KFs), CFs are preferred when an application calls for simpler implementation, less expensive computing, and fewer parallel processing steps. As previous states, the most used algorithm in human motion applications is the Madgwick's one. In fact, for this reason, this is the method employed in this work to estimate orientation. This is a CF that employs a quaternion representation of orientation. It can be used with IMUs as well as MIMUs, and it gives the user the option of estimating orientation only using the accelerometer and gyroscope or also adding the information from the magnetometer. Integrating the angular rate and then correcting this value using readings from the accelerometer (and magnetometer) constitutes the fundamental method for determining the orientation from the MIMU data. To perform this, the direction of the gyroscope measurement error is computed as a quaternion derivative using the accelerometer and magnetometer data in an optimised gradient-descent algorithm[65]. The greatest advantage of this filter is that include a single adjustable parameter β . The key parameter (β) is associated with zero-mean gyroscope measurement errors. It determines the weighting assigned to Earth's vectors (gravity and magnetic field) as a multiplicative factor of the gyroscope measurement error. Thus, a higher β implies greater emphasis on accelerometer and magnetometer signals. To provide specifics, the final estimate, which describes the orientation of Earth's coordinate system (ECS) relative to the MIMU coordinate system, coinciding with the local coordinate system (LCS), combines two separately found quaternions. One is obtained from the angular velocity provided by the gyroscope, and the other from accelerometer and magnetometer signals. The algorithm can be summarized as follows:

- Quaternion estimation from the integration of angular rate

$${}^E_L \hat{q}_{\omega,t} = ({}^E_L \hat{q}_{\text{est},t-1} + \frac{1^E}{2^L} \hat{q}_{\text{est},t-1} \times \omega_t^L) \Delta t \quad (3.13)$$

where ω_t^L is the angular measurement at time t , Δt is the sampling period and ${}^E_L \hat{q}_{\text{est},t-1}$ is the previous estimate of orientation.

- Optimal estimate of the Earth's vector-based quaternion obtained aligning the gravity and the magnetic field expressed in ECS with their observations referred to LCS. This is accomplished by minimizing an objective function, which is defined as the disparity between the components of Earth's vector in the LCS and the components rotated in the ECS. The objective function itself is formed by combining two separate objective functions derived from accelerometer and magnetometer signals

$$\nabla f = J_{g,b}^T({}^E_L \hat{q}_{\text{est},t-1}, \hat{b}^E) f_{g,b}({}^E_L \hat{q}_{\text{est},t-1}, \hat{a}^L, \hat{b}^E, \hat{m}^L) \quad (3.14)$$

where f is the objective function, \hat{m}^L and \hat{a}^L stand for \hat{s}^L , while \hat{b}^E stands for \hat{d}^E . Indeed, \hat{m}^L represents the normalized magnetometer measurement expressed in the LCS, while \hat{a}^L represents the normalized accelerometer measurement. Additionally, \hat{b}^E denotes the magnetic field in the ECS.

- Sensor fusion step in which the two previous estimates are merged in a weighted average

$${}^E_L \hat{q}_{\text{est},t} = {}^E_L \hat{q}_{\text{est},t-1} + \Delta t ({}^E_L \dot{q}_{\omega,t} - \beta \frac{\nabla f}{\|\nabla f\|}) \quad (3.15)$$

This estimate is the final orientation estimate, β represent the factor related to the divergence rate of the quaternion coming from the integration of the angular rate.

- Compensation of magnetic distortion serves to minimise magnetic disturbances that affect the heading component of the orientation. This compensation helps maintain the accuracy of the heading information despite environmental magnetic interference.
- Gyroscope bias drift compensation involves estimating and mitigating the bias in the gyroscope measurements by applying a low-pass filtering method to reduce errors in the rate of change of orientation over time. This helps improve the overall precision and reliability of the orientation data obtained from the gyroscope.

In figure 3.8 the block diagram representation of the complete orientation estimation algorithm for Madgwick's complete orientation filter including magnetic distortion and gyroscope drift compensation is depicted.

Embracing this filter offers several advantages, including the requirement to adjust just one parameter β , which is determined by gyroscope measurement errors,

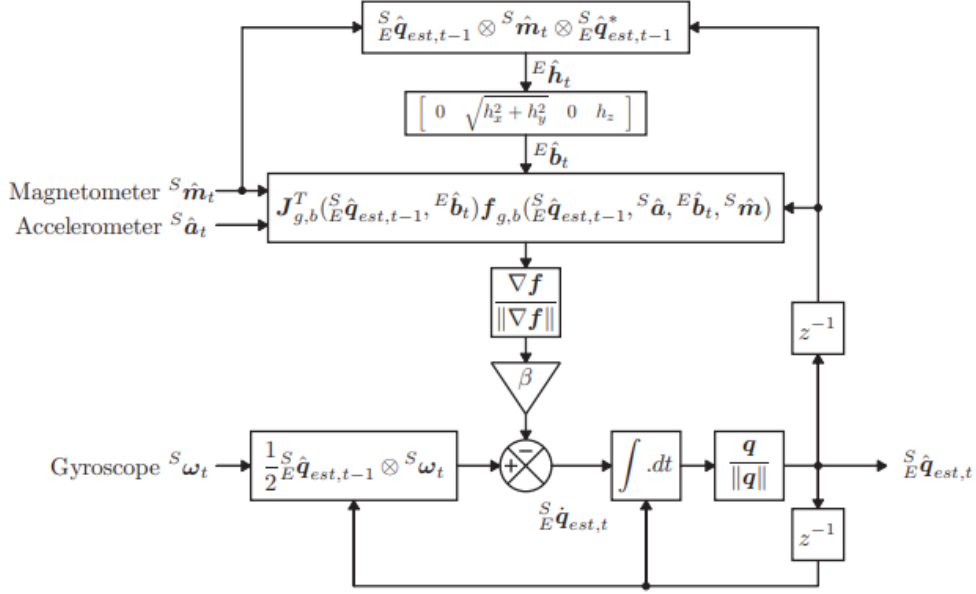


Figure 3.8: Block diagram representation of the complete orientation estimation algorithm for Madgwick's complete orientation filter including magnetic distortion and gyroscope drift compensation.

and a significant reduction in computational burden thanks to the utilisation of an analytically derived Jacobian matrix for error calculation.

The determination of the optimal value for β is accomplished through fine-tuning.

Quaternion Initialisation influence

The Madgwick algorithm is based on a loop in which a new orientation is determined from the one from the previous step for each time step. Therefore, it is crucial to consider how to select the first initial quaternion \mathbf{q}_0 , which enables the loop to start. The initialisation influences the period of initial convergence of the filter.

In this thesis work, two initialisation methods proposed in the literature were compared: Valenti *et al.* [57] and Suzuki *et al.* [66]. It is worth noting that Suzuki's method was specifically introduced in the context of running analysis.

Valenti *et al.* [57] proposed a sensor fusion algorithm that use the acceleration and magnetic field data in combination. If magnetic disturbances are present, the algorithm utilises acceleration information, while in case of absence of disturbances, both information are used. At the core of Valenti's algorithm, there is a fundamental assumption that must be upheld. This assumption is that the body segment where the MIMU is attached remains stationary before any motion begins. Based on

this hypothesis, a method for initialising quaternions is required that does not depend on gyroscope data. This is because, in a static condition, the gyroscope cannot detect any changes in orientation through angular velocity. Nevertheless, in static conditions, the accelerometer and magnetometer remain valuable sources of information for estimating orientation by sensing Earth’s vectors.

This algorithm exclusively considers observations related to the Earth’s magnetic field and operates by considering two distinct fields: gravity and the magnetic field. It relies on determining the inverse rotation that allows the measured quantities, specifically the accelerometer signal (a^L) and the magnetometer signal (m^L), both expressed in the LCS, to be referenced to the ECS. In the ECS, the x-axis aligns with magnetic north, while the z-axis aligns with gravity. The resolution equations for this approach are as follows:

$$R({}_L^E q)a^L = g^E \quad (3.16)$$

$$R({}_L^E q)m^L = h^E \quad (3.17)$$

These two equations serve to mathematically represent the core concept of rotating the sensor vector readings into the Earth-Centered System (ECS). Nevertheless, it is important to note that this system is overdetermined, which means it lacks a unique solution. To address this, certain measures are taken to impose predefined global components. So, it is possible to determine the rotation matrix responsible for this transformation, and consequently, the quaternion as well. To reduce the system’s degree of freedom, a constraint is introduced. This constraint requires that the magnetic reading, denoted as h^E must fall within the half-plane ${}^E \Pi_{zx} +$. This half-plane comprises all the points in the x-z plane with non-negative x coordinates.

$$R({}_L^E q)m^L = h^E \in {}^E \Pi_{zx} + \quad (3.18)$$

${}_L^E q$ can be decomposed into two quaternions, q_{acc} and q_{mag} .

Observing the gravity and magnetic vectors in the two reference frames allows the findings of the quaternions that perform the transformation between the two representations, q_{acc} and q_{mag} respectively.

$$R(q_{acc}) \begin{bmatrix} 0 \\ 0 \\ 1 \end{bmatrix} = \begin{bmatrix} a_x \\ a_y \\ a_z \end{bmatrix} \quad (3.19)$$

q_{acc} is found and used to rotate the magnetometer signal m_L .

$$R^T(q_{acc})m^L = h^E \quad (3.20)$$

In the scenario where h^E exhibits non-zero components exclusively in the x and z directions, the rotation resulting from this quaternion does not influence the

pitch and roll components. Consequently, when magnetic disturbances are present, their impact is confined to the heading direction, without introducing errors or corruption in the roll and pitch components.

$$\frac{E}{L}q = q_{acc} \times q_{mag} \quad (3.21)$$

Madgwick's filter employs quaternions that represent the rotation from the LCS to ECS. On the other hand, Valenti's discussed algorithm deals with the inverse quaternion, which represents the rotation from the ECS to the LCS. Consequently, the quaternion we derived earlier must be conjugated (referred to as $\frac{E}{L}q^*$ before it is utilised in the initial iteration of Madgwick's filter.

Suzuki *et al.* [66] proposed a method that first estimates the orientation of the IMU and the trajectory of the foot. This estimate is then utilised to correct the Euler angles, assuming that the runners are running straight on level ground in one cycle, and that the mediolateral and vertical displacement of the foot at each mid-stance should be zero. To transform the local data into ECS, the roll angle ϕ and a temporary pitch angle θ of the IMU at the mid-stance instant (MS_i) were determined using the following procedure:

$$\phi_{MS_i} = \arctan\left(\frac{-a_y}{\sqrt{a_x^2 + a_z^2}}\right) \quad (3.22)$$

$$\theta_{MS_i} = \arctan\left(\frac{a_x}{a_z}\right) \quad (3.23)$$

where a_x , a_y and a_z are respectively the medio-lateral, antero-posterior and vertical component of the measured acceleration at MS_i .

However, since the yaw angle ϕ could not be accurately estimated from the acceleration data, it was provisionally set to zero at this stage. After the MS_i , the orientation of the IMU was determined by integrating the measured angular velocity until the occurrence of the next mid-stance moment (MS_{i+1}). The measured acceleration data was then transformed into the ECS using the calculated quaternion. The foot trajectory was subsequently computed through the integration of the acceleration, which had been corrected for gravitational effects, using the following procedure:

$$v = v_0 + \int_{MS_i}^{MS_{i+1}} a^g dt \quad (3.24)$$

$$p = p_0 + \int_{MS_i}^{MS_{i+1}} v dt \quad (3.25)$$

where a^g represents the acceleration with the gravitational component removed, v stands for the velocity, and p represents the position of the foot in the global coordinate system. The initial values for velocity (v_0) and position (p_0) are both

set to zero. Considering the assumption that runners move in a straight line on level ground within one cycle, the lateral and vertical displacements of the foot at MS_{i+1} should ideally be zero. Therefore, the yaw angle was determined based on the foot's position at MS_{i+1} using the following calculation:

$$\phi_{MS_i} = \arctan\left(\frac{p_y}{p_x}\right) \quad (3.26)$$

where p_y and p_x are the medio-lateral and antero-posterior positions of the foot at MS_{i+1} .

Likewise, the pitch angle was recalculated based on the foot's position at MS_{i+1} . Due to the non-linearity in the relationship between the pitch angle and the vertical position at MS_{i+1} , a gradient descent method was employed to compute the pitch angle that results in a zero vertical position at MS_{i+1} . The initial pitch angle for this calculation was defined as follows:

$$\theta'_{MS_i} = \arctan\left(\frac{p_z}{\sqrt{p_x^2 + p_y^2}}\right) + \theta_{MS_i} \quad (3.27)$$

The calculated Euler angles are subsequently converted into quaternions for use in the Madgwick algorithm during initialisation.

Since Valenti's initialisation method can either consider or not consider magnetometer information, while Suzuki's method does not use it, the comparison was conducted without utilising the magnetometer in both cases.

Optimisation of Madgwick parameter

As a multiplicative factor of the gyroscope measurement error, β really determines how much weight to give to the information of the Earth's vectors (gravity and magnetic field). In the presence of magnetic disturbances, the recorded local magnetic field is not accurately detected. Therefore, the higher β the higher the weight given to accelerometer and inaccurate magnetometer signals. The optimal β value is achieved through iterative trial and error approaches with and without the use of the magnetometer data ([67],[68]). Initially, several values were explored starting from the one used for gait analysis (i.e., 0.0019 rad/s). In a preliminary investigation, 20 β values were explored with a wide range, ranging from 0.001 to 1 in increments of 0.05. Subsequently, 5 more values have been investigated, ranging from 0.0001 to 0.001 in increments of 0.0002. Then, the vicinity of the β value that yielded the minimum error in terms of stride velocity and stride length was explored, ranging from 0.0065 to 0.01 in increments of 0.0005. Therefore, the optimal value was obtained through error minimisation.

Reliability check of integration instants

In this estimation pipeline, orientation is re-initialised at each integration instant to reduce the drift in the orientation estimation. To use the algebraic initialisation by Valenti *et al.* [57] the assumption of foot stationarity must hold valid. No references were found in the literature regarding the reliability check of integration instants. The norm of gyroscope and accelerometer data were moving averaged. To determine the reliability, specific criteria must be imposed for these norms at each integration instant. A technique that compares the norm values at the specified integration instant with a threshold value (one each for acceleration and angular velocity) was proposed.

To establish these thresholds, an overlap analysis was conducted across all trials and subjects for the ZUPT intervals of both the gold standard and those derived from the parametric detector. The mean and standard deviation of the norms of the moving averages within the overlap interval were then calculated.

This process is carried out separately for the two datasets that are collected at different speeds. Running speed affected the thresholds on the acceleration and angular velocity. In addition, in sprinting, unlike treadmill running, the pace varied.

Table 3.3: Experimentally determined threshold values for acceleration and angular velocity based on stride duration intervals.

Stride Duration (s)	Acceleration threshold (m/s^2) ²	Angular velocity threshold (deg/s)
>0.60	23	293
0.57 - 0.60	31	470
0.54 - 0.57	40	520
0.50 - 0.54	44	670
<0.54	46	690

For the dataset at 14 km/h it was possible to define unique values for these two thresholds. By evaluating these parameters among subjects, it was possible to extract the values of the thresholds (162 deg/s for the angular velocity and 9 m/s for the acceleration). For the dataset that ranges from 19 to 29 km/h, a different approach was adopted. In this case, the duration of the preceding step was evaluated to understand at what speed the runner was moving and to select the most suitable threshold accordingly. This allowed for the assignment of a different threshold, which depended on the individual’s duration during that stride. It is important to emphasise that behind this process, experimental thresholds derived from available data are used (Table 3.3).

If the ZUPT instant was considered not reliable, the orientation was not re-initialised at that point.

3.3.4 Methods for velocity drift removal

Displacement estimations are inaccurate due to residual drift. To overcome this problem, various solutions have been adopted in the literature to enhance the accuracy of double integration. Many authors employ these three different velocity drift removal methods:

- Linear De-Drifting of the velocity [50]
- Subtraction of the mean of the acceleration before integrations[69]
- Direct and Reverse Integration (DRI) [51]

These methods have been implemented to verify their equivalence.

3.3.5 Validation procedures

Amateurs protocol – 14 km/h

By taking the derivative of the marker trajectories obtained through the SP, it is possible to extract the velocity profile. Therefore, with access to foot marker trajectories, a reference for velocity could be derived. The marker-derived velocities were subjected to low-pass filtering using a fourth-order Butterworth filter with a cutoff frequency of 10 Hz to enhance the quality of the signal, as reported in [66]. The reference stride velocity was calculated as the norm of the antero-posterior and medio-lateral components of the marker-derived velocity. The reference stride length was calculated as the norm of the antero-posterior and medio-lateral components of the trajectory of markers positioned above the MIMU.

Sprinters protocol – from 19 km/h to 29 km/h

The GoPro HERO10 image is usually affected by barrel distortion, the typical look of a wide-angle lens (Figure ??), and for this reason is not possible to implement a simple pixel to meters proportion.

To overcome this issue, a lens correction was performed. In the setup, cones were strategically placed in fixed positions to facilitate subsequent reference points. The correction of distortions was carried out using a Python code that can be found in the GitHub [70] This enabled the use of "undistorted" images aligned along the horizon line to establish known references for measurements [71]. After the lens correction a set number of pixels reflect the same real-world length, so it



Figure 3.9: *Typical look of a wide angle lens.*

is possible to perform a simple pixel to distance proportion to calculate the stride length. Given x as stride length in pixels, and y as stride length in meters:

$$y = \frac{x \cdot 40m}{3424px} \quad (3.28)$$

where 3424 is the number of pixel equal to the image width, showing 40 meters. At this point, an ad-hoc algorithm was implemented to perform a manual labelling process to identify the foot position at three different instants:

- Initial Contact;
- Midstance Instant;
- Final Contact.

The SL was calculated as the distance between two midstance phases of the same foot. The SV at this point was evaluated using the stride lengths derived from the labelling and the interval of time between one midstance point (MS_{i+1}) and the precedent one (MS_i):

$$SV_i = \frac{SL_i}{MS_{i+1} - MS_i} \quad (3.29)$$

3.3.6 Metrics for the pipeline assessment

At each step of the pipeline, multiple algorithms were compared, and the selection of the optimal one was based on minimising errors of the estimated parameters compared to the available references (SP for the dataset at 14 km/h and PIs and video for the sprint dataset). The metrics evaluated at each step of the algorithm are:

- **Mean Error (ME)**, that represent the average signed difference between the values of the estimated and the reference parameter of interest:

$$ME = \frac{1}{N} \sum_{i=1}^N (y_i - \hat{y}_i) \quad (3.30)$$

Where y_i and \hat{y}_i denote respectively the target and predicted values of the parameter and N is the total number of the parameter's values. %ME is calculated as well:

$$ME = \frac{1}{N} \sum_{i=1}^N \left(\frac{y_i - \hat{y}_i}{\hat{y}_i} \right) * 100 \quad (3.31)$$

- **Mean Absolute Error (MAE)**, that represent the average unsigned difference between the values of the estimated and the reference parameter of interest:

$$MAE = \frac{1}{N} \sum_{i=1}^N |y_i - \hat{y}_i| \quad (3.32)$$

The %MAE is also computed:

$$MAE = \frac{1}{N} \sum_{i=1}^N \left| \frac{y_i - \hat{y}_i}{\hat{y}_i} \right| * 100 \quad (3.33)$$

- **Root Mean Squared Error (RMSE)**, that measure the root mean square difference between the N estimated values and the N corresponding reference values:

$$RMSE = \frac{1}{N} \sum_{i=1}^N \sqrt{(y_i - \hat{y}_i)^2} \quad (3.34)$$

These metrics were computed for running stride velocity and stride length. Afterward, the average of the metrics across subjects is computed.

Chapter 4

Results

Errors in the evaluation of stride length and stride velocity were obtained through the differences between the inertial-based estimates and the reference parameters provided by the gold standards (i.e., the SP or video recordings from the GoPro camera). In this section the ME, MAE and RMSE in the estimation of SV and SL are reported for each dataset (i.e., both at 14 km/h and during sprinting). For both datasets, the overall averaged values have been evaluated. Furthermore, since the speed was not fixed in sprinting, of the mean velocity (MV) was analysed in this dataset. Results obtained for each metric are expressed in terms of mean \pm standard deviation. In all the following tables values between brackets denote the percentage errors.

4.1 Spatio-temporal parameter estimation with the baseline pipeline

The starting point of this work was the baseline pipeline for the estimation of the stride length, optimised for walking applications [36]. The main steps and associated parameters of the baseline pipeline were:

1. reorientation of the vertical sensor axis with the gravity during standing;
2. ARE ZUPT detector [13];
3. definition of the integration instants at the 50% of each ZUPT interval [36];
4. orientation estimation through Madgwick's filter using $\beta=0.0019$ rad/s [38];
5. orientation initialisation using the algebraic quaternion [57]
6. double integration of the accelerations through DRI [51].

Dataset at 14 km/h

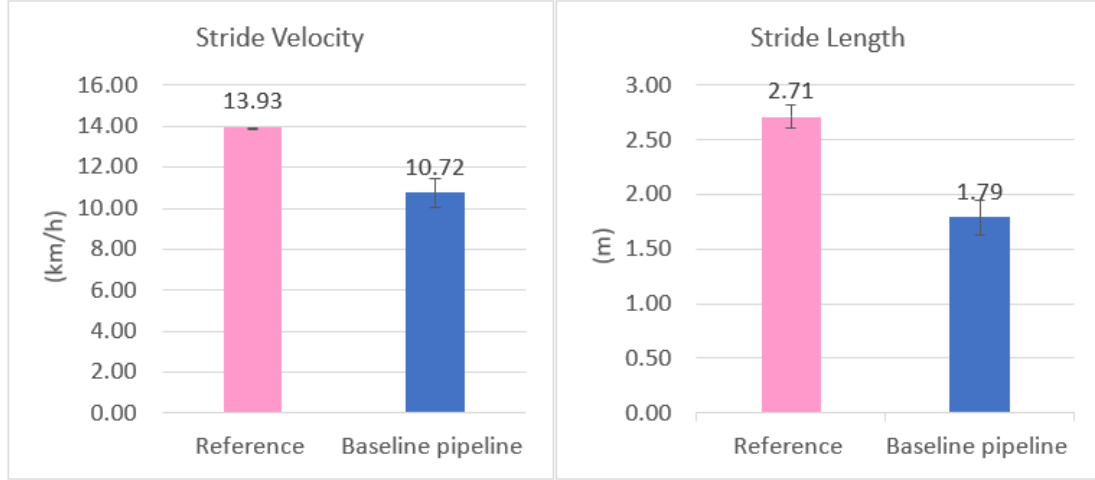


Figure 4.1: Comparison between SV and SL derived from the SP and those obtained from the MIMU with the baseline pipeline.

In Figure 4.1, there is a comparison between the averaged reference SL and SV values given by SP and the averaged values obtained from the MIMU sensor data using the basic pipeline for the data at 14 km/h. In this case the threshold utilised for the ARE detectors was $0.3 \cdot 10^5 \text{ deg/s}$, that was obtained through investigations.

Table 4.1: Summary of the results obtained with the non-optimised pipeline for the dataset at 14 km/h.

	Stride Velocity Errors			Stride Length Errors		
	ME (km/h)	MAE (km/h)	RMSE (km/h)	ME (m)	MAE (m)	RMSE (m)
Baseline Pipeline	-2.78 ± 0.68 (-19.69%±5.14%)	2.78 ± 0.68 (19.69%±5.14%)	2.78 ± 0.68	-0.92 ± 0.04 (-34.87%±2.02%)	0.92 ± 0.04 (34.87%±2.02%)	0.92 ± 0.04

The SV errors between the reference and the estimated are computed in Table 4.1 using the baseline pipeline, the RMSE error was 2.75 km/h for SV and 92 cm for SL and the MAE% was about 19% for the SV and about 35% for the SL.

In Figure 4.2 there is a representation of the displacement estimated with the baseline pipeline. The black curve represents the displacement in the horizontal plane, while the blue one is the vertical component.

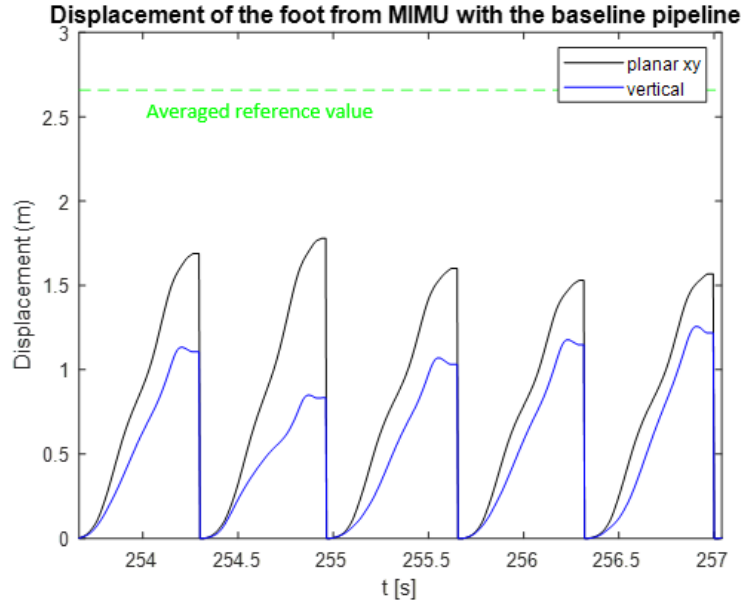


Figure 4.2: Displacement estimated with the baseline pipeline, where the black curve represents the displacement in the horizontal plane x - y and the blue curve represents the vertical component. The dashed green line represents the averaged reference value provided by the SP.

Dataset at 19-29 km/h

In this dataset, the velocity is not constant but varied between 19 km/h and 29 km/h. Therefore, the MV over the trial is evaluated and compared with the reference. This reference speed was calculated straightforwardly as the distance covered (50 meters) divided by the time recorded with the stopwatch.

In the bar chart in Figure 4.3 it is possible to compare the results. The threshold employed for this dataset for the detection of the ZUPT intervals with the ARE method was $0.5 * 10^5 \text{deg/s}$, obtained through trials and errors process.

Secondly, a comparison between SV and SL parameters derived from the Go-Pro recordings and those obtained from the MIMU with the baseline pipeline (Figure 4.4).

Table 4.2 shows the results obtained in terms of SV and SL computed for sprint velocities.

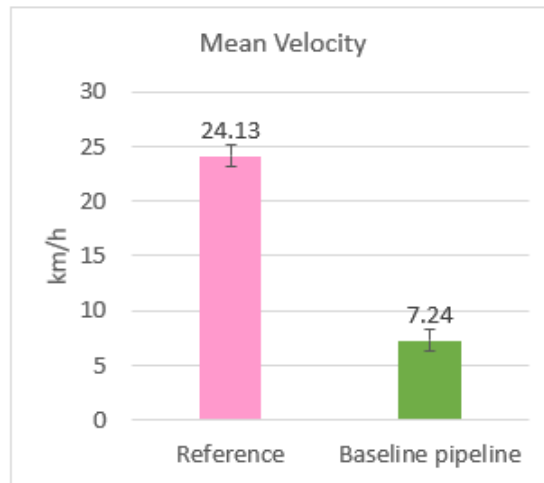


Figure 4.3: Comparison between the MV obtained from the reference and from the MIMU with the baseline pipeline, among the 7 subjects, for the dataset at 19-29 km/h.

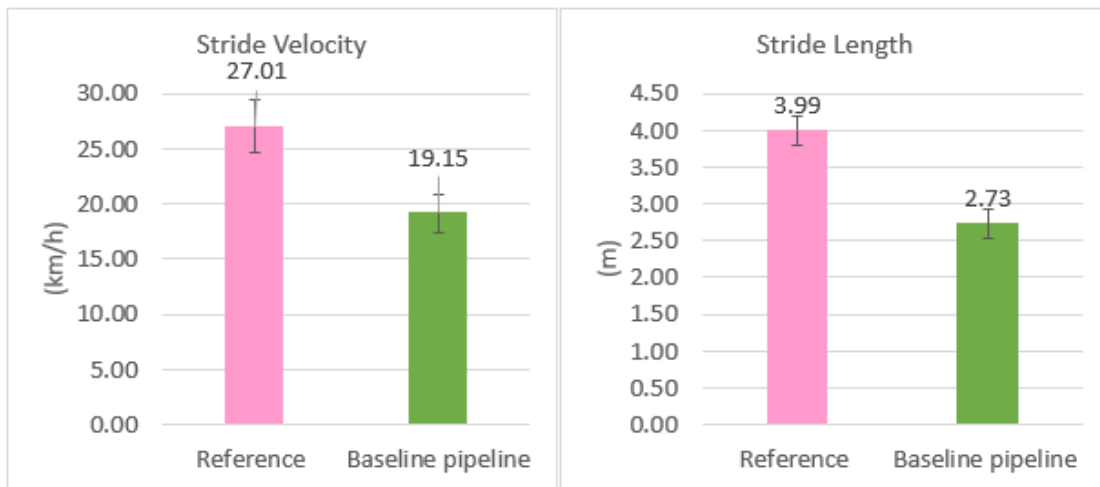


Figure 4.4: Comparison between SV and SL derived from the GoPro and those obtained from the MIMU with the baseline pipeline, among 7 subjects, for the dataset at 19-29 km/h.

Table 4.2: Summary of the results obtained with the non-optimised pipeline for the dataset at 19-29 km/h.

	Stride Velocity Errors			Stride Length Errors		
	ME (km/h)	MAE (km/h)	RMSE (km/h)	ME (m)	MAE (m)	RMSE (m)
Baseline	-7.38 ± 2.06	7.38 ± 2.06	7.38 ± 2.06	-1.27 ± 0.35	1.27 ± 0.35	1.27 ± 0.35
Pipeline	$(-22.31\% \pm 4.27\%)$	$(-22.31\% \pm 4.27\%)$	7.38 ± 2.06	$(-31.12\% \pm 7.33\%)$	$(-31.12\% \pm 7.33\%)$	1.27 ± 0.35

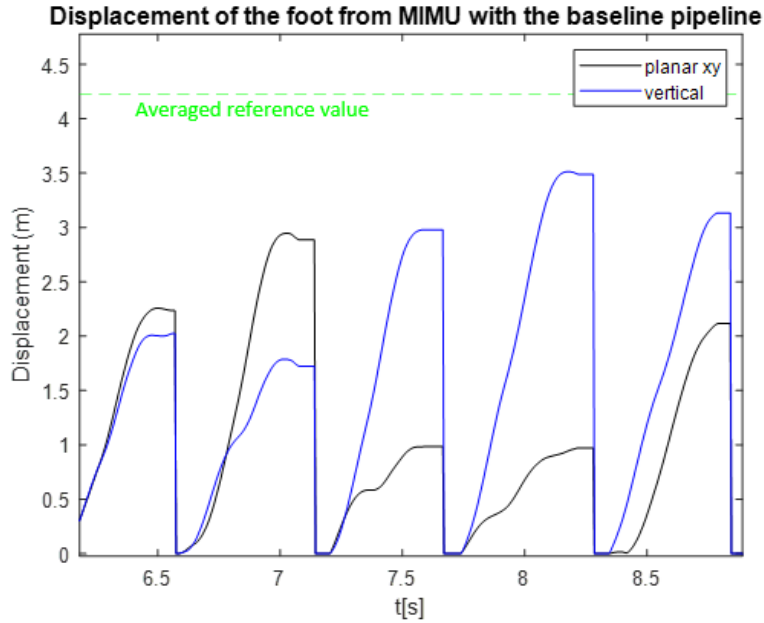


Figure 4.5: Displacement estimated with the baseline pipeline, where the black curve represents the displacement in the plane x - y and the blue curve represents the vertical component. The dashed line represents the reference value provided by the GoPRO.

4.2 Optimisation of the state-of-the-art methods for the estimation of running speed and stride length

In this section, the results at each optimisation step of the pipeline are presented. Results for both datasets are presented step by step.

4.2.1 Zero Velocity detectors

In the first optimisation step, a comparison is conducted among ZUPT detectors to understand the impact of this choice on the estimation of the parameters of interest. Comparative graphs are provided, illustrating the estimated ZUPT intervals obtained from the different detectors in relation to the reference Gold Standard. For the same signal, the estimated ZUPT intervals are plotted alongside their corresponding T values. These graphs serve for visual comparisons.

Dataset at 14 km/h

For the constant speed dataset at 14 km/h, the graphical results obtained from different ZUPT detectors are reported (from Figure 4.6 to Figure 4.10). The ZUPT detectors employed in the comparison are from Skog et al. [13] (Angular Rate Energy Detector (ARE), Stance Hypothesis Optimal Detector (SHOE), Acceleration Moving Variance Detector (MV), Acceleration Magnitude Detector (MAG)) and from Rossanigo et al.[36] (the parametric detector).

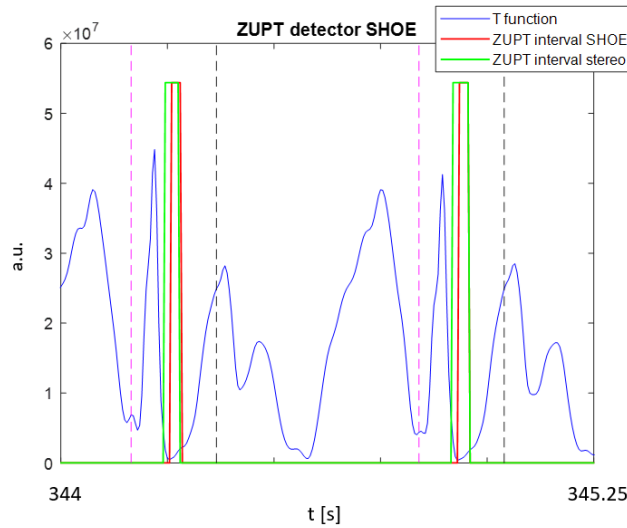


Figure 4.6: *SHOE ZUPT intervals vs SP ZUPT intervals.*

The visual inspection allowed for the exclusion of some of the detectors analysed (i.e., MAG and MV). Hence, it was decided to proceed with the comparison using the remaining detectors. In the Table 4.3, the results of the assessment of the overlap between estimated ZUPT intervals and intervals found using SP is reported. A ZUPT overlap was defined as the percentage of samples of a found ZUPT interval, obtained from MIMU data, that were included also in the corresponding reference ZUPT interval.

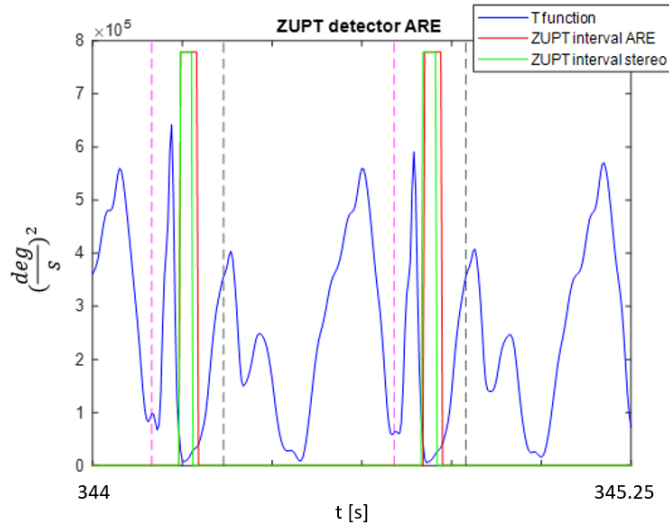


Figure 4.7: ARE ZUPT intervals vs SP ZUPT intervals.

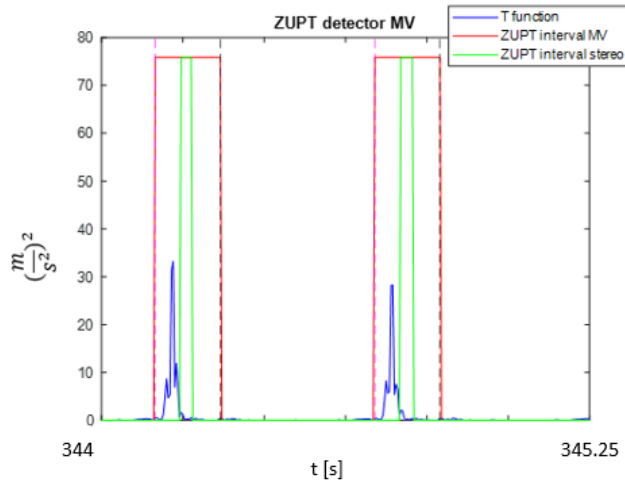


Figure 4.8: MV ZUPT intervals vs SP ZUPT intervals.

The percentage of overlap between the estimated ZUPT interval and the reference is above 95.5% for all three detectors selected.

The bar charts in Figure 4.11 display the average values of SV and SL across all subjects, comparing the reference values with those obtained using the pipeline with the variation of the employed ZUPT detector.

In Table 4.4, the values of the calculated metrics for each of the selected ZUPT detectors are reported.

Thanks to the graph in Figure 4.12 of displacements in the horizontal plane

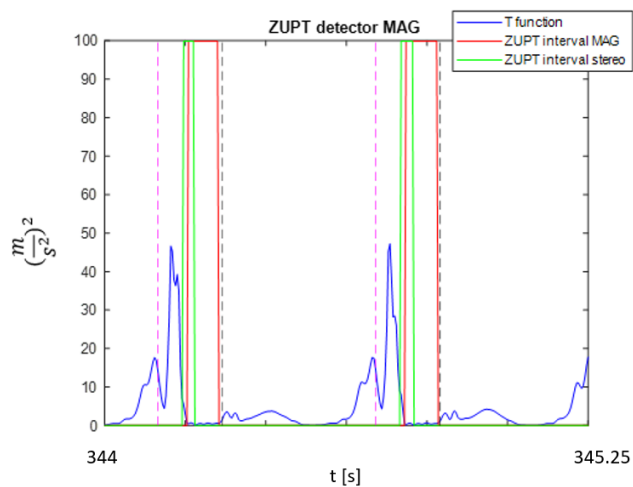


Figure 4.9: *MAG ZUPT intervals vs SP ZUPT intervals.*

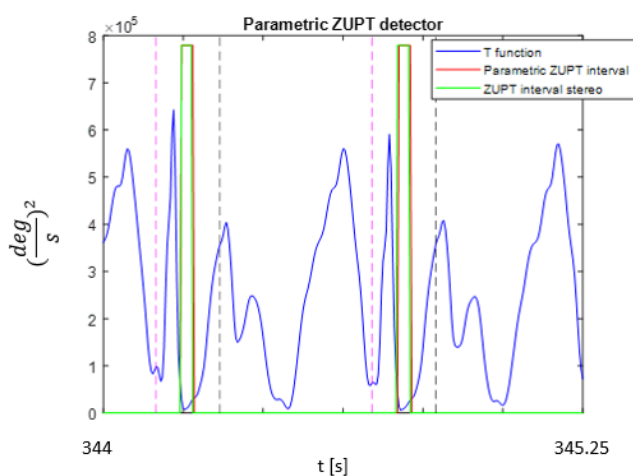


Figure 4.10: *MAG ZUPT intervals vs SP ZUPT intervals.*

calculated using different ZUPT detectors, it can be observed how the choice of the detector influences the estimation. The result of using the detector present in the baseline pipeline (ARE) is shown in blue, while the red and violet curves represent the trend of displacement in the x-y plane using the SHOE and parametric detectors, respectively.

Table 4.3: Results of the percentage overlap between estimated ZUPT intervals and those obtained from the SP.

Detectors	Overlap %
Skog et al. 2010 (SHOE)	96.3 % \pm 3.1%
Skog et al. 2010 (ARE)	95.5% \pm 2.6%
Rossanigo et al. 2021	95.4% \pm 3.4 %

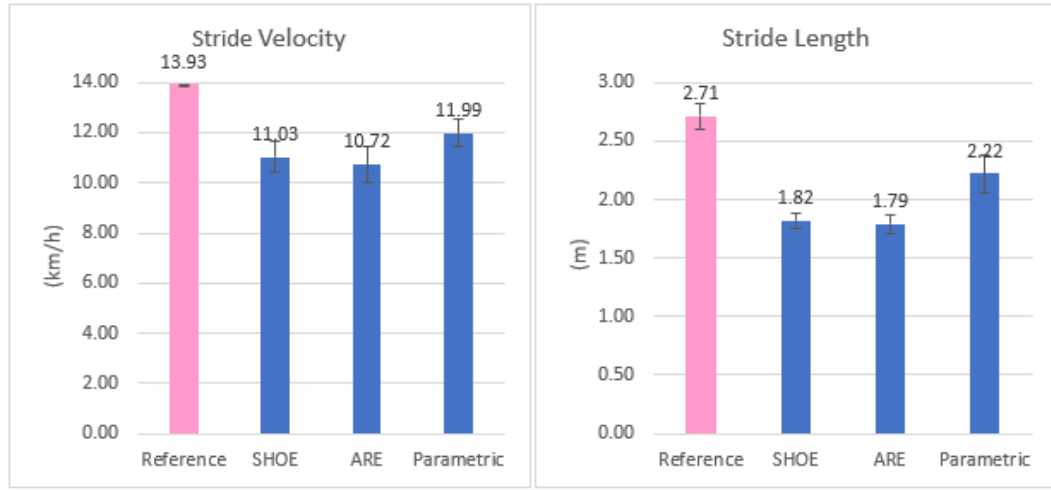


Figure 4.11: Comparison between SV and SL derived from the SP and those obtained from the MIMU utilising different ZUPT detectors.

Dataset at 19-27 km/h

Similarly, for the sprinting dataset, graphs comparing ZUPT intervals obtained with different detectors and against the gold standard of pressure-sensitive insoles are presented (Figure 4.13-4.18). For this dataset, where pressure sensors data are available, the result of the detector proposed by Ma et al. [60] is also reported.

The visual inspection allowed for the exclusion of some of the detectors analysed also for this dataset (i.e. MV and MAG). In addition, it was decided to retain detectors that rely solely on information from the inertial sensors. In the table below, the results of the assessment of the overlap between estimated ZUPT intervals and intervals found using pressure data from the insoles is reported.

The bar charts (Figure 4.19) illustrate the SV and SL across subjects. These charts compare the reference values with those derived from the pipeline using different ZUPT detectors. The thresholds employed for the ARE and SHOE detectors are $0.5 \cdot 10^5 \text{ deg/s}$ and 15 respectively.

Table 4.4: Results regarding the SV and SL at the ZUPT detector optimisation phase of the algorithm for the dataset at 14 km/h.

Detectors	Stride Velocity Errors			Stride Length Errors		
	ME (km/h)	MAE (km/h)	RMSE (km/h)	ME (m)	MAE (m)	RMSE (m)
Skog et al. 2010 (SHOE)	-2.38 ± 0.61 (-17.07%±4.62%)	2.38 ± 0.61 (17.07%±4.62%)	2.38 ± 0.61	-0.89 ± 0.05 (-32.80%±2.07%)	0.89 ± 0.05 (32.80%±2.07%)	0.89 ± 0.05
Skog et al. 2010 (ARE)	-2.78 ± 0.68 (-19.69%±5.14%)	2.78 ± 0.68 (19.69%±5.14%)	2.78 ± 0.68	-0.92 ± 0.04 (-34.87%±2.02%)	0.92 ± 0.04 (34.87%±2.02%)	0.92 ± 0.04
Rossanigo et al. 2021	-1.94 ± 0.58 (-13.89%±4.13%)	1.94 ± 0.58 (13.89%±4.13%)	1.94 ± 0.58	-0.48 ± 0.12 (-17.85%±4.74%)	0.48 ± 0.12 (17.85%±4.74%)	0.48 ± 0.12

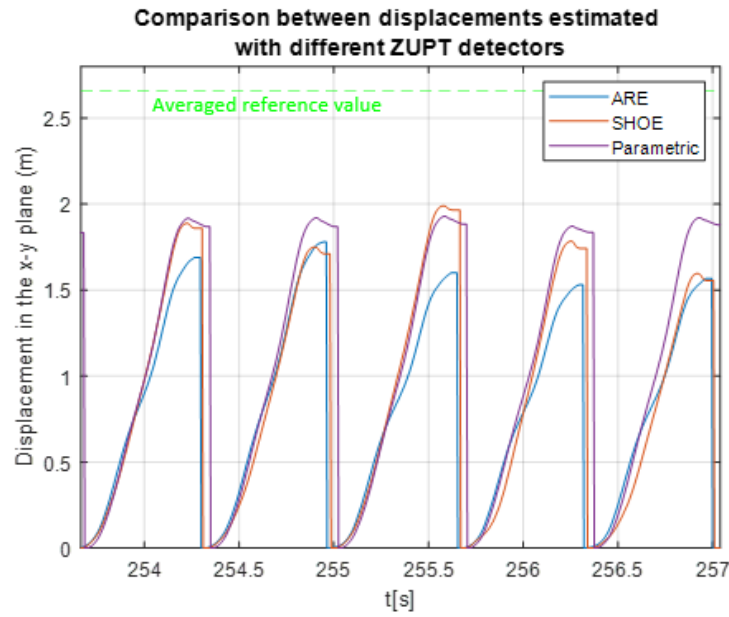


Figure 4.12: Comparison between displacement estimated with different ZUPT detectors. The dashed line represents the reference value provided by the SP.

In Table 4.6, the comparison between metrics for the sprint running dataset is reported.

In Figura 4.20, there is a comparison between the displacements calculated with various detectors.

4.2.2 Selection of integration boundaries of the integration interval

Once the choice of the ZUPT interval detector type was made, the evaluation of the choice of integration instant for both datasets was performed. The tested

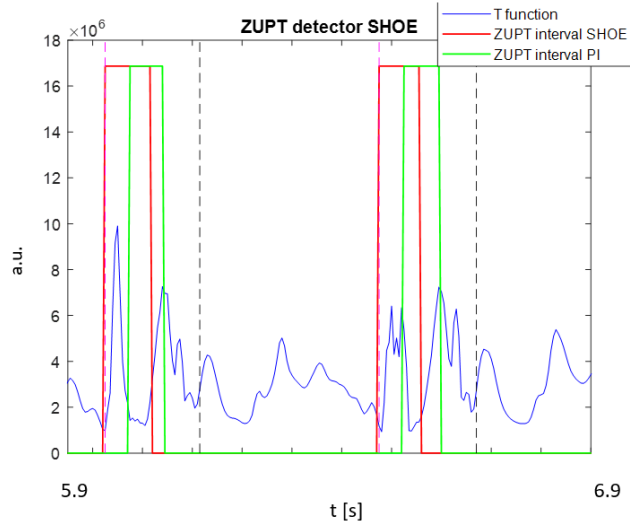


Figure 4.13: *SHOE ZUPT intervals vs Pressure Insoles ZUPT intervals.*

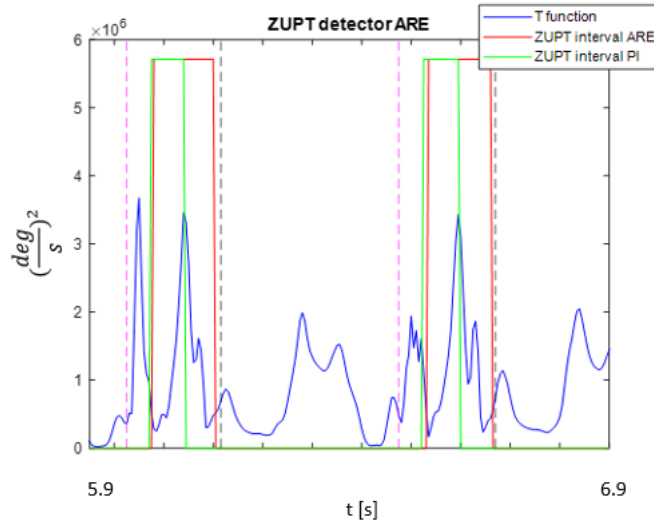


Figure 4.14: *ARE ZUPT intervals vs Pressure Insoles ZUPT intervals.*

definitions of the integration instants were:

- the 50% of the ZUPT interval [48],
- the end of the ZUPT interval [36],
- the minimum of the angular energy within the ZUPT interval [49],

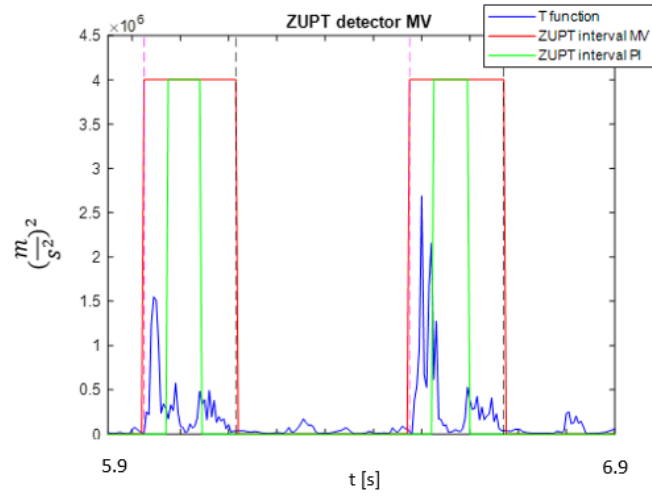


Figure 4.15: *MV ZUPT intervals vs Pressure Insoles ZUPT intervals.*

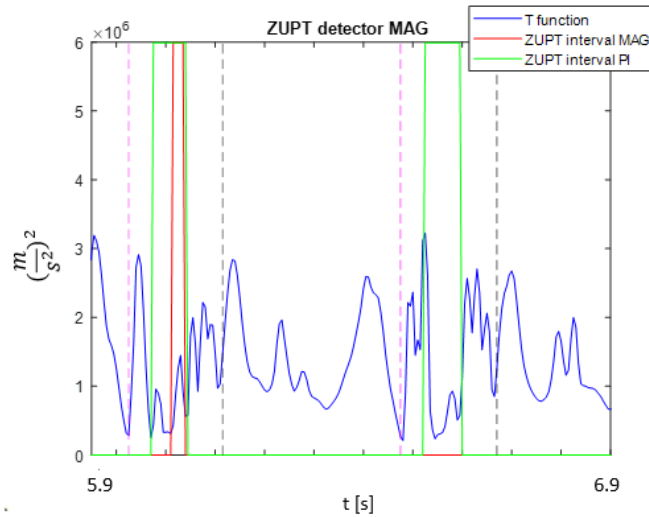


Figure 4.16: *MAG ZUPT intervals vs Pressure Insoles ZUPT intervals. In the second interval. It is noticeable how the MAG detector fails to detect the zero-velocity update (ZUPT) interval.*

- the minimum of the moving averaged angular rate norm within the ZUPT interval.

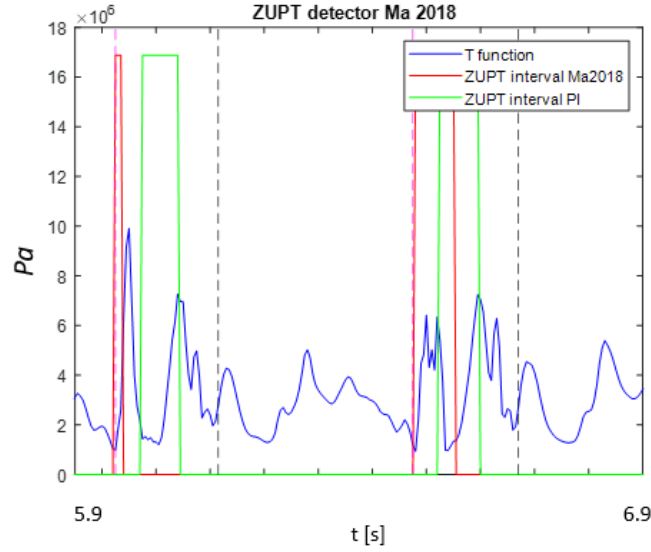


Figure 4.17: *Ma et al. 2018 ZUPT intervals vs Pressure Insoles ZUPT intervals.*

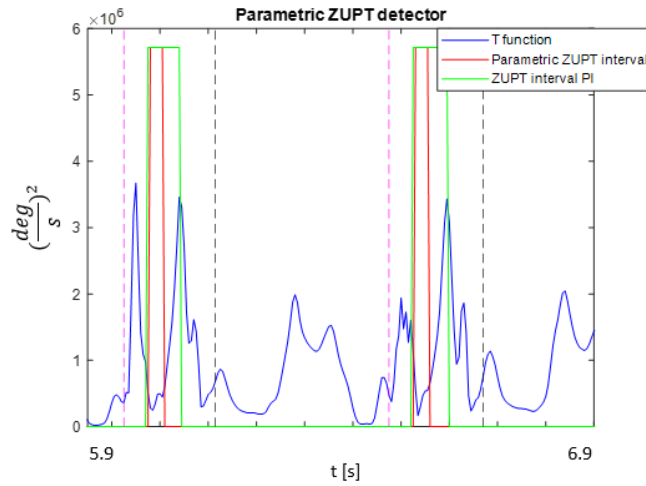


Figure 4.18: *Parametric ZUPT intervals vs Pressure Insoles ZUPT intervals*

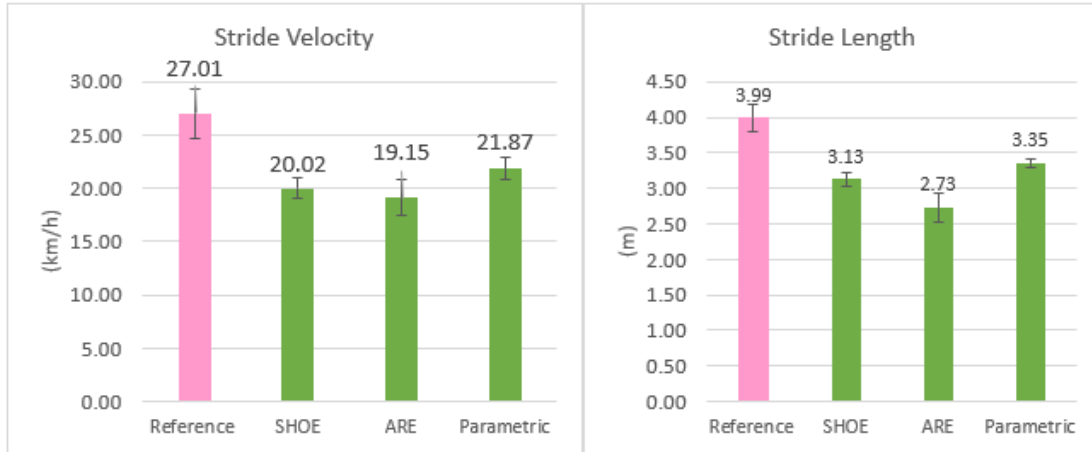
Dataset at 14 km/h

The bar charts in Figure 4.12 illustrates the average values of SV and SL across all subjects, comparing the reference values with those obtained using the pipeline while varying the employed definition of integration boundaries for the integration.

For the four definitions of integration instants, the numerical values of the calculated metrics are presented in Table 4.7.

Table 4.5: *Overlap% between estimated ZUPT intervals and the reference*

Detectors	Overlap %
Skog et al. 2010 (SHOE)	95.7 % \pm 3.5%
Skog et al. 2010 (ARE)	97.2% \pm 1.0%
Rossanigo et al. 2021	95.5% \pm 2.0%

**Figure 4.19:** *Comparison between SV and SL derived from the GoPro and those obtained from the MIMU utilising different ZUPT detectors.*

Dataset at 19-29 km/h

Also for this dataset, a comparison between the definitions of the integration instants for both SV and SL is shown in Figure 4.3. In Table 4.8, the results in terms of ME, MAE, and RMSE for SV and SL are reported as a function of the definition of the integration instant.

4.2.3 Orientation estimation

In this section, the results of the optimisation processes for the orientation estimation step of the pipeline are presented.

Quaternion Initialisation influence

To calculate the stride-by-stride orientation, the orientation was re-initialised at each integration instant. In this section, the results of the comparison between two initialisation methods, Valenti et al.[57], used in the baseline pipeline, and Suzuki et al. [66], are presented for both datasets.

Table 4.6: Results regarding the SV and SL at the ZUPT detector optimisation phase of the algorithm for the dataset at 19-29 km/h.

Detectors	Stride Velocity Errors			Stride Length Errors		
	ME (km/h)	MAE (km/h)	RMSE (km/h)	ME (m)	MAE (m)	RMSE (m)
Skog et al. 2010 (SHOE)	-6.50 ± 2.21 (-22.90%±5.38%)	6.50 ± 2.21 (22.90%±5.38%)	6.50 ± 2.21	-0.93 ± 0.25 (-21.76%±4.10%)	0.93 ± 0.25 (21.76%±4.10%)	0.93 ± 0.25
Skog et al. 2010 (ARE)	-7.38 ± 2.06 (-22.31%±4.27%)	7.38 ± 2.06 (22.31%±4.27%)	7.38 ± 2.06	-1.27 ± 0.35 (-31.12%±7.33%)	1.27 ± 0.35 (31.12%±7.33%)	1.27 ± 0.35
Rossanigo et al. 2021	-4.55 ± 1.49 (-16.70%±4.34%)	4.55 ± 1.49 (16.70%±4.34%)	4.55 ± 1.49	-0.64 ± 0.16 (-16.10%±3.56%)	0.64 ± 0.16 (16.10%±3.56%)	0.64 ± 0.16

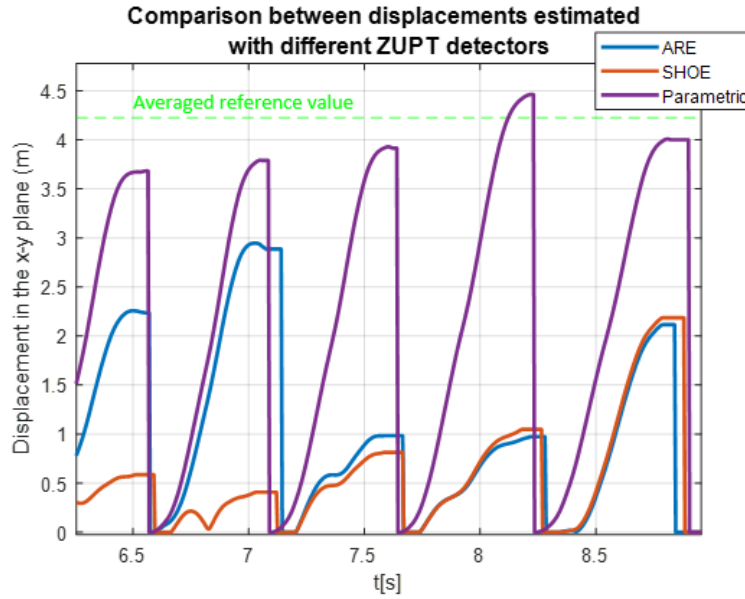


Figure 4.20: Comparison between displacement estimated with different ZUPT detectors. The dashed line represents the averaged reference value provided by the GoPro.

Dataset at 14 km/h

In Figure 4.24, there is a graphic representation of the quaternions obtained with the Valenti et al.[57] method and the Suzuki et al.[66] one.

In the bar diagrams below, it is possible to confront the stride-by-stride parameters derived from the gold standards and those extracted from the pipeline that uses the MIMU signals with different initialisations.

A numerical comparison is presented in Table 4.9 showing an RMSE value of 1.77 km/h for SV with Valenti's method and a value of 2.83 km/h with the Suzuki



Figure 4.21: Comparison between the SV and SL derived from the SP and those obtained from the MIMU utilising different definitions of integration instant for the integration intervals.

one. In the case of SL, the RMSE is almost 40 cm for Valenti, while it is 64 cm for Suzuki.

In Figure 4.26, where the curves of the displacement calculated with the two initialisation methods are shown, it is noted that the red curve representing the displacement with Suzuki et al. [66] initialisation is lower than that obtained with Valenti et al.[57].

Table 4.7: Results regarding the SV and SL with the four definitions of integration instants, for the dataset at 14 km/h.

Definition of Integration Instants	Stride Velocity Errors			Stride Length Errors		
	ME (km/h)	MAE (km/h)	RMSE (km/h)	ME (m)	MAE (m)	RMSE (m)
50% of ZUPT interval	-1.94 ± 0.58 (-13.89%±4.13%)	1.94 ± 0.58 (13.89%±4.13%)	1.94 ± 0.58	-0.48 ± 0.12 (-17.85%±4.74%)	0.48 ± 0.12 (17.85%±4.74%)	0.48 ± 0.12
End of ZUPT interval	-2.75 ± 0.57 (-19.77%±4.10%)	2.75 ± 0.57 (19.77%±4.10%)	2.75 ± 0.57	-0.65 ± 0.12 (-24.26%±4.89%)	0.65 ± 0.12 (24.26%±4.89%)	0.65 ± 0.12
Min of kinetic energy	-2.07 ± 0.65 (-14.82%±4.65%)	2.07 ± 0.65 (14.82%±4.65%)	2.07 ± 0.65	-0.51 ± 0.13 (-19.01%±5.11%)	0.51 ± 0.13 (19.01%±5.11%)	0.51 ± 0.13
Min of angular rate norm	-1.45 ± 0.45 (-10.40%±3.20%)	1.45 ± 0.45 (10.40%±3.20%)	1.45 ± 0.45	-0.39 ± 0.09 (-14.48%±3.41%)	0.39 ± 0.09 (14.48%±3.41%)	0.39 ± 0.09

Table 4.8: Results regarding the SV and SL with the four definitions of integration instants, for the dataset at 19-29 km/h.

Definition of Integration Instants	Stride Velocity Errors			Stride Length Errors		
	ME (km/h)	MAE (km/h)	RMSE (km/h)	ME (m)	MAE (m)	RMSE (m)
50% of ZUPT interval	-4.55 ± 1.49 (-16.70%±4.34%)	4.55 ± 1.49 (16.70%±4.34%)	4.55 ± 1.49	-0.64 ± 0.16 (-16.10%±3.56%)	0.64 ± 0.16 (16.10%±3.56%)	0.64 ± 0.16
End of ZUPT interval	-4.88 ± 1.55 (-16.97%±5.18%)	4.88 ± 1.55 (16.97%±5.18%)	4.88 ± 1.55	-0.71 ± 0.13 (-17.91%±3.32%)	0.71 ± 0.13 (17.91%±3.32%)	0.71 ± 0.13
Min of kinetic energy	-4.46 ± 1.49 (-15.82%±4.69%)	4.46 ± 1.49 (15.82%±4.69%)	4.46 ± 1.49	-0.68 ± 0.13 (-17.40%±3.20%)	0.68 ± 0.13 (17.40%±3.20%)	0.68 ± 0.13
Min of angular rate norm	-3.9 ± 1.37 (-14.33%±4.16%)	3.9 ± 1.37 (14.33%±4.16%)	3.9 ± 1.37	-0.58 ± 0.15 (-14.93%±3.69%)	0.58 ± 0.15 (14.93%±3.69%)	0.58 ± 0.15

Dataset at 19-29 km/h

The bar diagrams in Figura 4.28 summarises the comparison between the two initialisation methods among the subject for the dataset at 19-29 km/h.

The trend of the bar diagram is confirmed in Table 4.10, where the errors are reported.

Optimisation of Madgwick parameter β

In this section, the results in terms of RMSE corresponding to the investigated β values in terms of SV and SL, are reported. Several β values were tested during the study, but for the sake of brevity, the results of a subset of eight values varying from 0.00009 rad/s to 1 rad/s are reported to highlight the influence of this parameter. Regarding the use of the magnetometer, it was decided not to consider it to avoid the influence of disturbances observed during an initial data exploration.

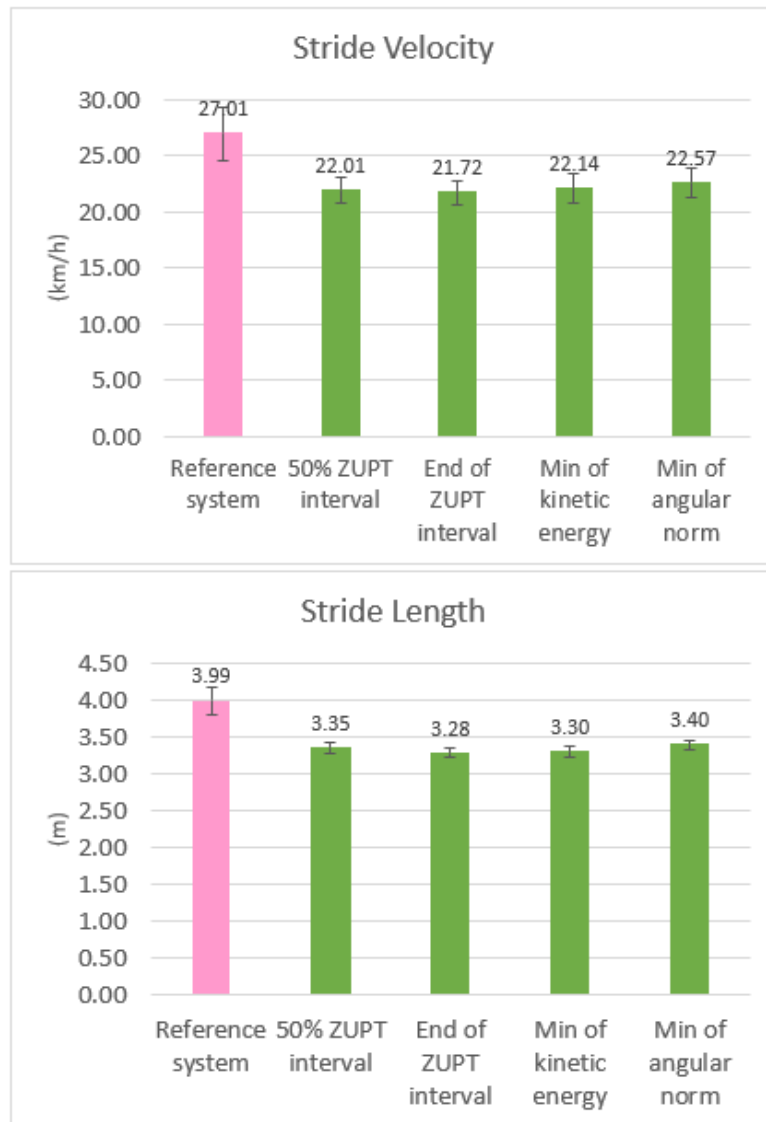


Figure 4.22: Comparison between the SV and SL derived from the GoPro and those obtained from the MIMU utilising different definitions of integration instant for the integration intervals.

Dataset at 14 km/h

The influence of Madgwick's β on SV and SL for the dataset at 14 km/h are reported focusing on the interval of interest, as reported in Figure 4.29 and Figure 4.30 .

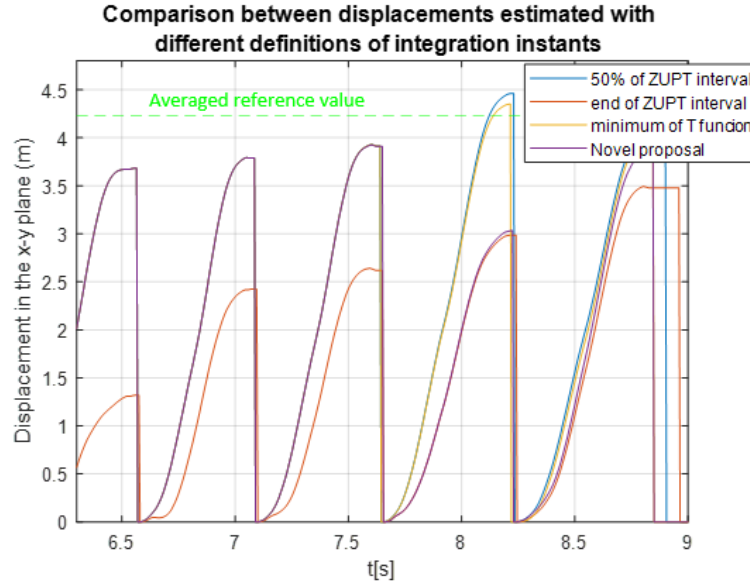


Figure 4.23: Comparison between the displacement estimated with different definitions of integration instants. The dashed line represents the reference value provided by the GoPro (dataset at 19-29 km/h). T function is based on the angular velocity.

Table 4.9: Results regarding the SV and SL with the different methods of initialization of the quaternion, for the dataset at 14 km/h.

	Stride Velocity Errors			Stride Length Errors		
	ME (km/h)	MAE (km/h)	RMSE (km/h)	ME (m)	MAE (m)	RMSE (m)
Valenti	-1.45 ± 0.45 (-10.40%±3.20%)	1.45 ± 0.45 (10.40%±3.20%)	1.45 ± 0.45	-0.39 ± 0.09 (-14.48%±3.41%)	0.39 ± 0.09 (14.48%±3.41%)	0.39 ± 0.09
Suzuki	-2.64 ± 0.99 (-18.94%±3.20%)	2.64 ± 0.99 (18.94%±3.20%)	2.64 ± 0.99	-0.64 ± 0.21 (-23.40%±7.59%)	0.64 ± 0.21 (23.40%±7.59%)	0.64 ± 0.21

Dataset at 19-29 km/h

The influence of Madgwick's β on SV and SL for the dataset of sprinting run are reported focusing on the interval of interest is reported in Figure 4.31 and Figure 4.32.

Reliability check of integration instants

In this section, the results obtained for both datasets are presented, including the addition of a reliability check for the integration instants.

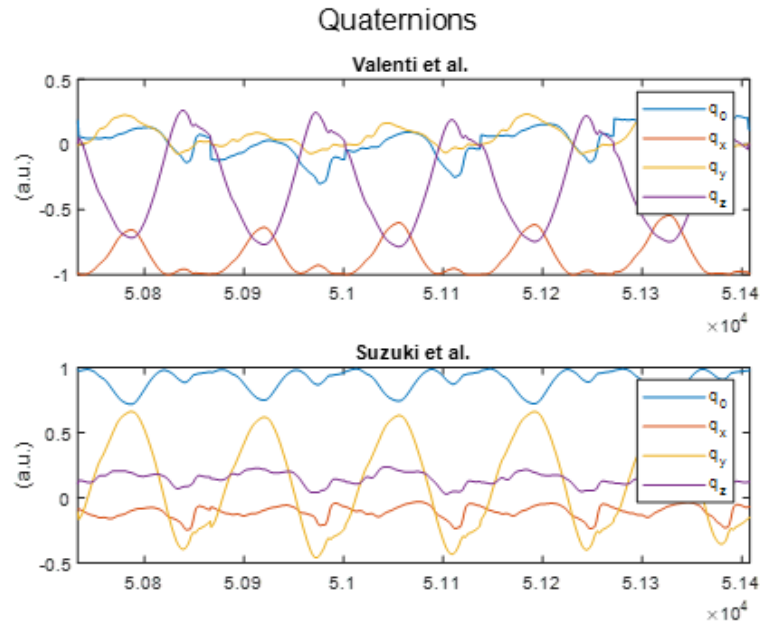


Figure 4.24: *Quaternions with different initialisation methods. q_0 is the scalar number.*

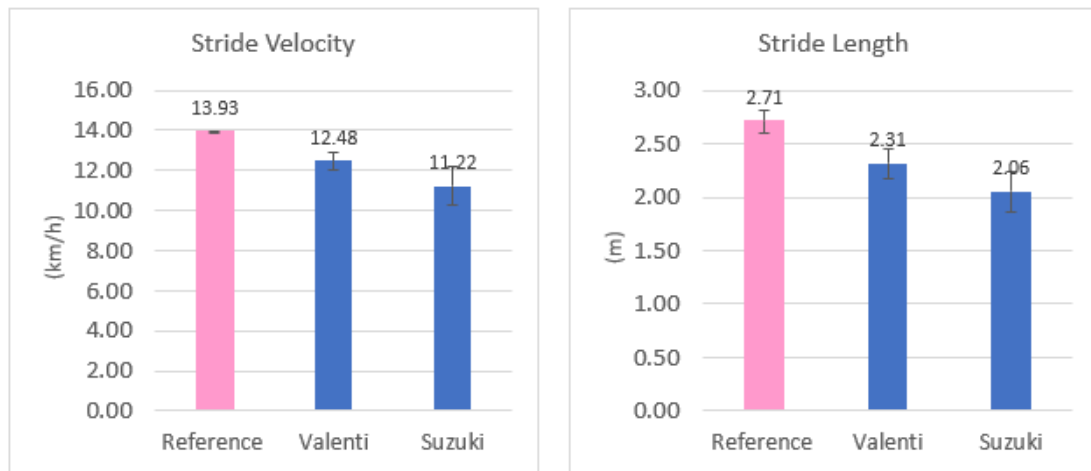


Figure 4.25: *Comparison between SV and SL derived from the SP and those obtained with different quaternion initialisation methods.*

Dataset at 14 km/h

In FigureFigure 4.33 the results of the reliability check of the integration instants in terms of SV and SV are reported.

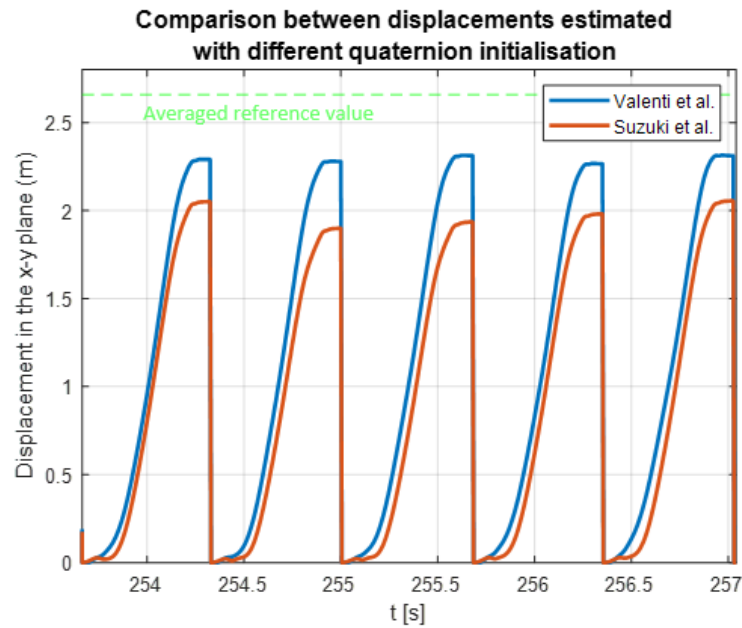


Figure 4.26: Comparison between displacements evaluated with different quaternion initialisations methods, at 14 km/h.

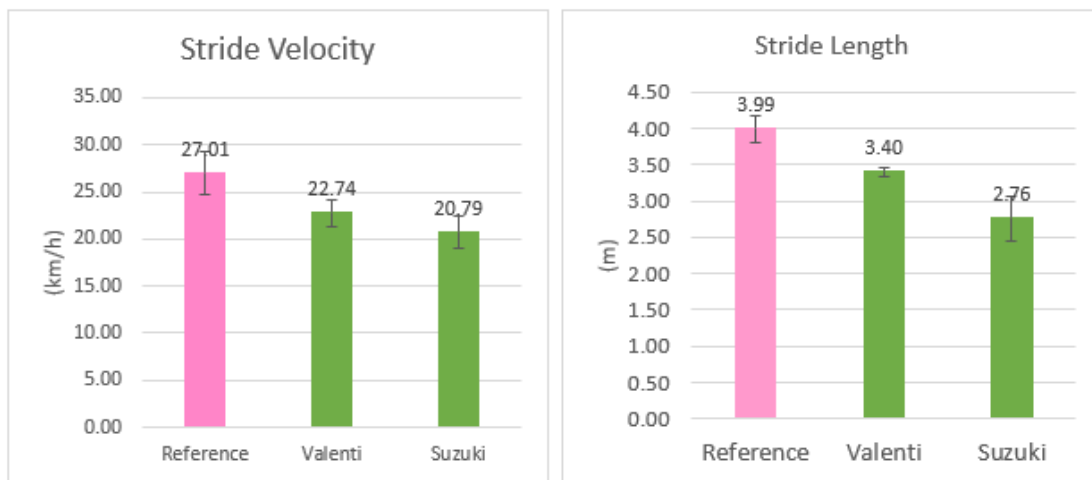


Figure 4.27: Results regarding the SV and SL with the different methods of initialisation of the quaternion, for the dataset at 19-29 km/h.

Dataset at 19-29 km/h

Performing this check resulted in significantly worse outcomes, leading to a deterioration of 31.4%.

Table 4.10: Results regarding the SV and SL with the different methods of initialisation of the quaternion, for the dataset at 19-29 km/h.

	Stride Velocity Errors			Stride Length Errors		
	ME (km/h)	MAE (km/h)	RMSE (km/h)	ME (m)	MAE (m)	RMSE (m)
Valenti	-3.9 ± 1.37 (-14.33%±4.16%)	3.9 ± 1.37 (14.33%±4.16%)	3.9 ± 1.37	-0.58 ± 0.15 (-14.93%±3.69%)	0.58 ± 0.15 (14.93%±3.69%)	0.58 ± 0.15
Suzuki	-5.34 ± 1.58 (-19.71%±1.58%)	5.34 ± 1.58 (19.71%±1.58%)	5.34 ± 1.58	-1.13 ± 0.27 (-29.51%±8.79%)	1.13 ± 0.27 (29.51%±8.79%)	1.13 ± 0.27

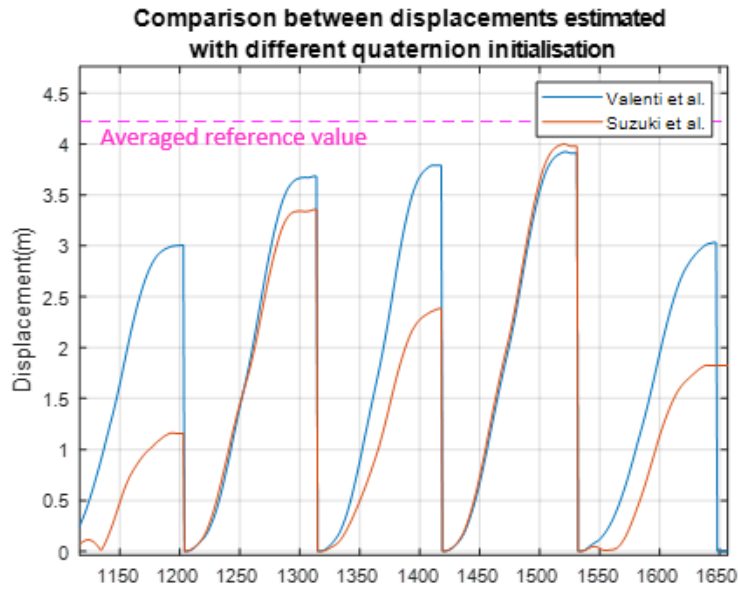


Figure 4.28: Comparison between displacements evaluated with different quaternion initialisations methods, at 19-29 km/h.

4.2.4 Methods for velocity drift removal

At the final stage of the pipeline optimisation process, once the previous choices have been made to improve the algorithm, a comparison is made between velocity de-drifting techniques:

- Direct and Reverse Integration (DRI)[51];
- Linear De-Drifting of the velocity[50];
- Subtraction of the mean of the acceleration before integrations [69].

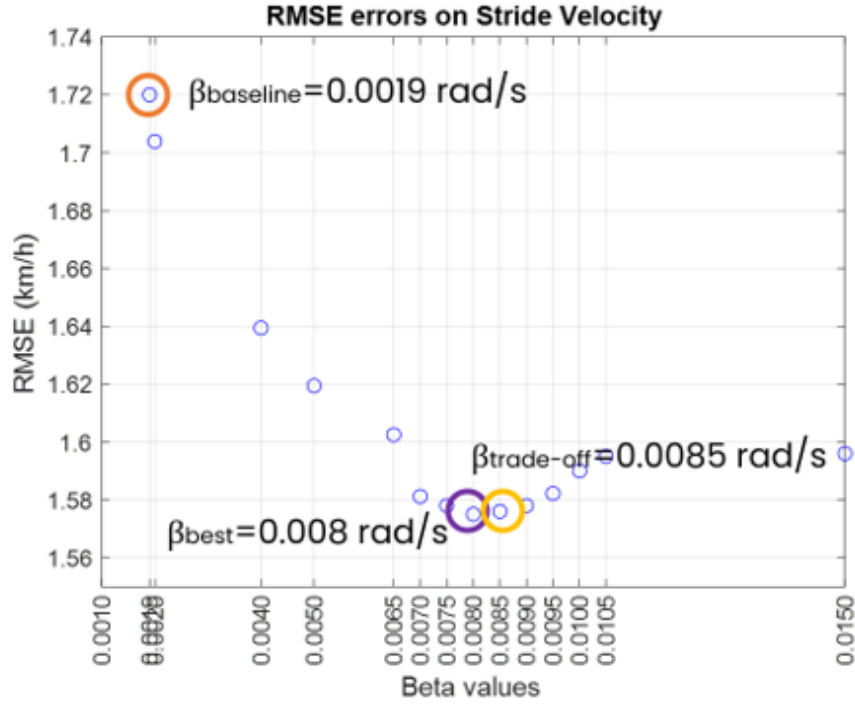


Figure 4.29: Influence of the β value on the RMSE error on SV, at 14km/h. In orange, the RMSE value is presented with the beta of the baseline pipeline, while in purple, the value minimising the RMSE error is shown. In yellow, the trade-off value between the two datasets is reported to achieve a unique value.

Dataset at 14 km/h

In Figure 4.34 the comparison between the three de-drifting techniques is reported in the bar graph.

In Table 4.11, there are the numerical values of the metrics estimated.

Table 4.11: Results regarding the SV and SL with the different de-drifting methods, for the dataset at 14 km/h.

	Stride Velocity Errors			Stride Length Errors		
	ME (km/h)	MAE (km/h)	RMSE (km/h)	ME (m)	MAE (m)	RMSE (m)
DRI	-1.45 ± 0.45 (-10.40%±3.20%)	1.45 ± 0.45 (10.40%±3.20%)	1.45 ± 0.45	-0.39 ± 0.09 (-14.48%±3.41%)	0.39 ± 0.09 (14.48%±3.41%)	0.39 ± 0.09
Linear De-Drifting	-1.45 ± 0.44 (-10.40%±3.20%)	1.45 ± 0.44 (10.40%±3.20%)	1.45 ± 0.44	-0.39 ± 0.09 (-14.48%±3.41%)	0.39 ± 0.09 (14.48%±3.41%)	0.39 ± 0.09
Removal of mean acc.	-4.55 ± 1.49 (-16.70%±4.34%)	4.55 ± 1.49 (16.70%±4.34%)	4.55 ± 1.49	-0.64 ± 0.16 (-16.10%±3.56%)	0.64 ± 0.16 (16.10%±3.56%)	0.64 ± 0.16

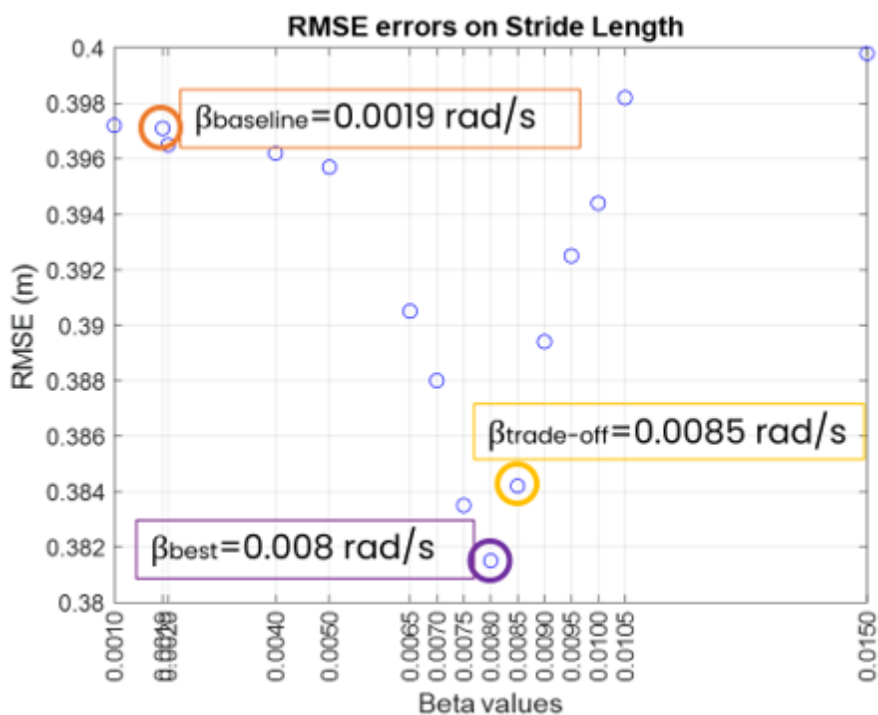


Figure 4.30: Influence of the β value on the RMSE error on SL, at 14km/h. In orange, the RMSE value is presented with the beta of the baseline pipeline, while in purple, the value minimising the RMSE error is shown. In yellow, the trade-off value between the two datasets is reported to achieve a unique value.

The graph in Figure 4.35 confirms the equivalence of the de-drifting methods.

Dataset at 19-29 km/h

In Figure 4.36 the comparison between the three de-drifting techniques is reported in the bar graph.

The numerical results of the metrics are reported in Table 4.12.

In Figure 4.37 the comparison between different methods of de-drifting is reported.

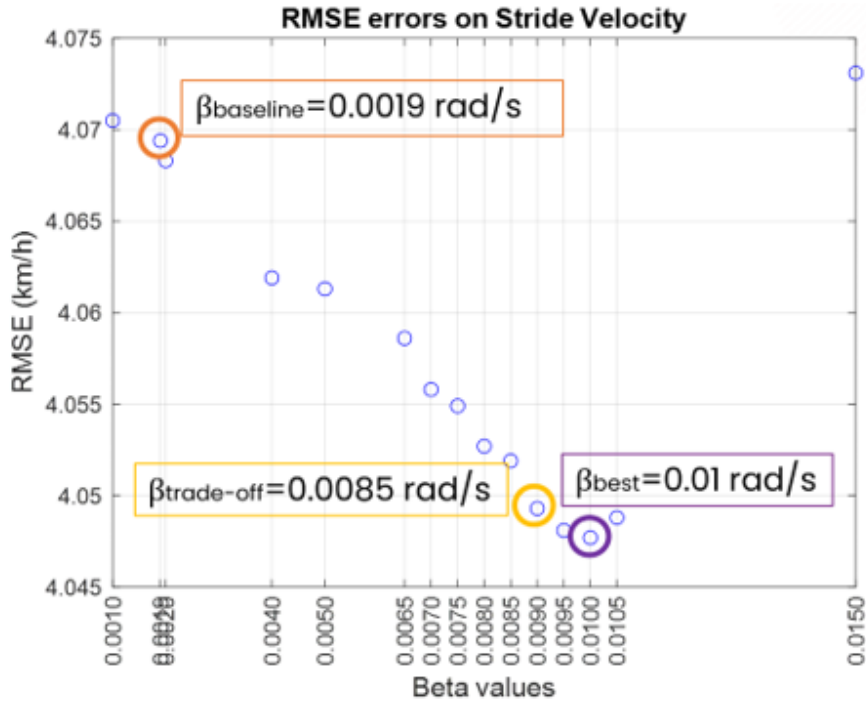


Figure 4.31: Influence of the β value on the RMSE error on SV, at 19-29 km/h. In orange, the RMSE value is presented with the beta of the baseline pipeline, while in purple, the value minimising the RMSE error is shown. In yellow, the trade-off value between the two datasets is reported to achieve a unique value.

Table 4.12: Results regarding the SV and SL with the different de-drifting methods, for the dataset at 19-29 km/h.

	Stride Velocity Errors			Stride Length Errors		
	ME (km/h)	MAE (km/h)	RMSE (km/h)	ME (m)	MAE (m)	RMSE (m)
DRI	-3.9 ± 1.37 (-14.33%±4.16%)	3.9 ± 1.37 (14.33%±4.16%)	3.9 ± 1.37	-0.58 ± 0.15 (-14.93%±3.69%)	0.58 ± 0.15 (14.93%±3.69%)	0.58 ± 0.15
Linear De-Drifting	-3.9 ± 1.37 (-14.33%±4.16%)	3.9 ± 1.37 (14.33%±4.16%)	3.9 ± 1.37	-0.58 ± 0.15 (-14.93%±3.69%)	0.58 ± 0.15 (14.93%±3.69%)	0.58 ± 0.15
Removal of mean acc.	-3.9 ± 1.37 (-14.33%±4.16%)	3.9 ± 1.37 (14.33%±4.16%)	3.9 ± 1.37	-0.58 ± 0.15 (-14.93%±3.69%)	0.58 ± 0.15 (14.93%±3.69%)	0.58 ± 0.15

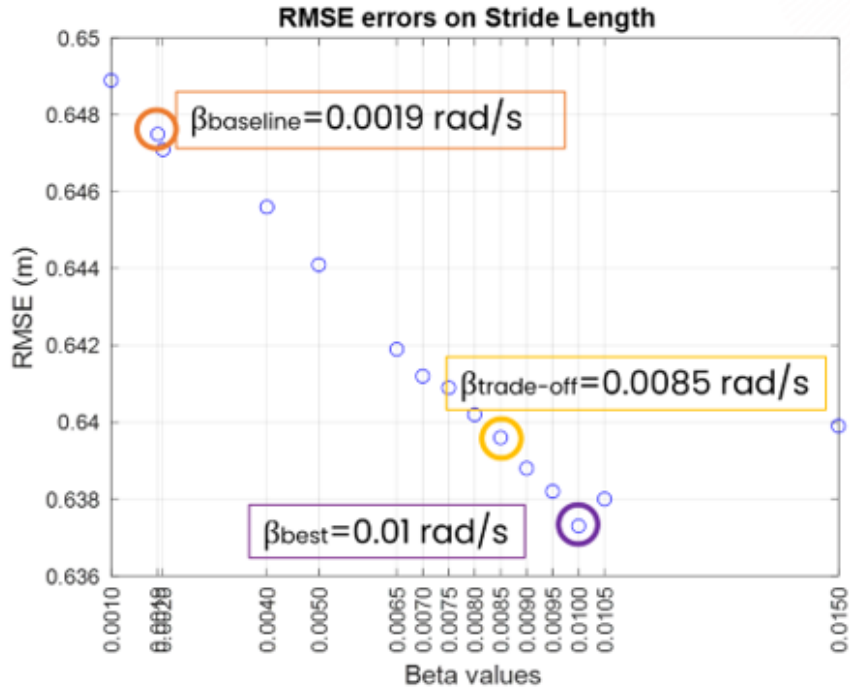


Figure 4.32: Influence of the β value on the RMSE error on SL, at 19-29km/h. In orange, the RMSE value is presented with the beta of the baseline pipeline, while in purple, the value minimising the RMSE error is shown. In yellow, the trade-off value between the two datasets is reported to achieve a unique value.

4.2.5 Comparison between the original pipeline and the optimised algorithm

Dataset at 14 km/h

To provide an overview of the difference between the results obtained with the baseline pipeline and the optimised one, the following charts are presented in Figure 4.38.

In the Table 4.13 it is possible to compare the metrics obtained at the beginning with those at the endpoint of the optimisation process of the pipeline presented in this study. With the baseline pipeline, there was an RMSE error of 2.75 km/h for SV, which decreased to 1.57 km/h with the optimised pipeline, while it went from 92 cm to 39 cm for SL from the baseline pipeline to the optimised one.

In Figure 4.39, the difference between the initial algorithm and the optimised one is notable.

At the end of the optimisation process of the spatio-temporal parameter estimation pipeline, Bland-Altman plots were used to assess the trend of errors among

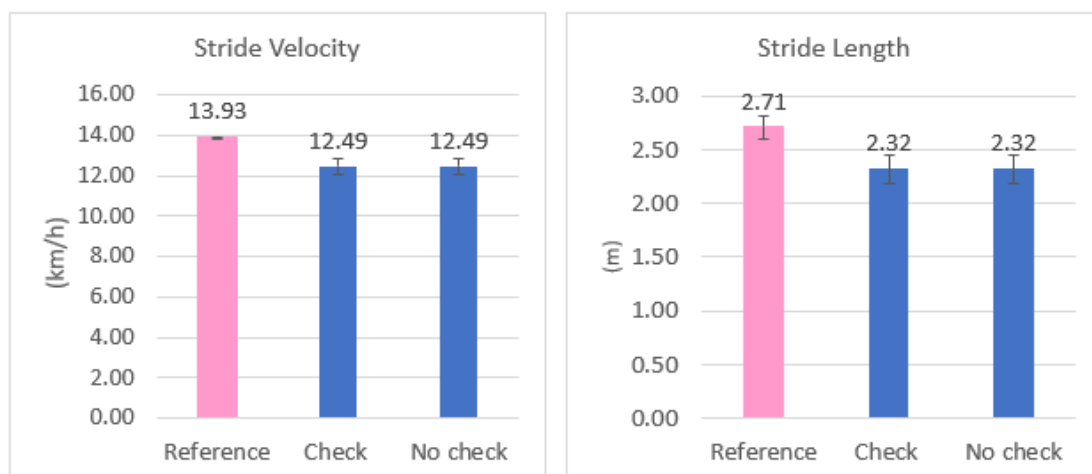


Figure 4.33: Comparison between the SV and SL derived from the SP and those obtained with and without the reliability check of the integration instants, for the dataset at 14km/h.

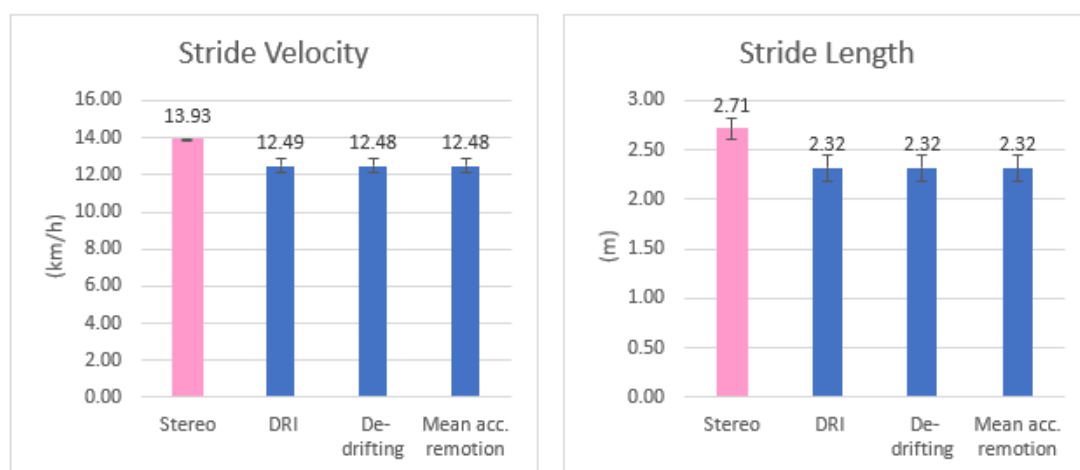


Figure 4.34: Comparison between SV and SL derived from the SP and those obtained with different de-drifting methods.

subjects.

In Figure 4.40, the comparison between the SV of all subjects in the dataset is presented, comparing SP with the use of the baseline pipeline.

In Figure 4.41, the comparison between the SV of all subjects in the dataset is presented, comparing SP with the use of the optimised pipeline.

Also for the SL, the Bland-Altman plot to assess the agreement between the

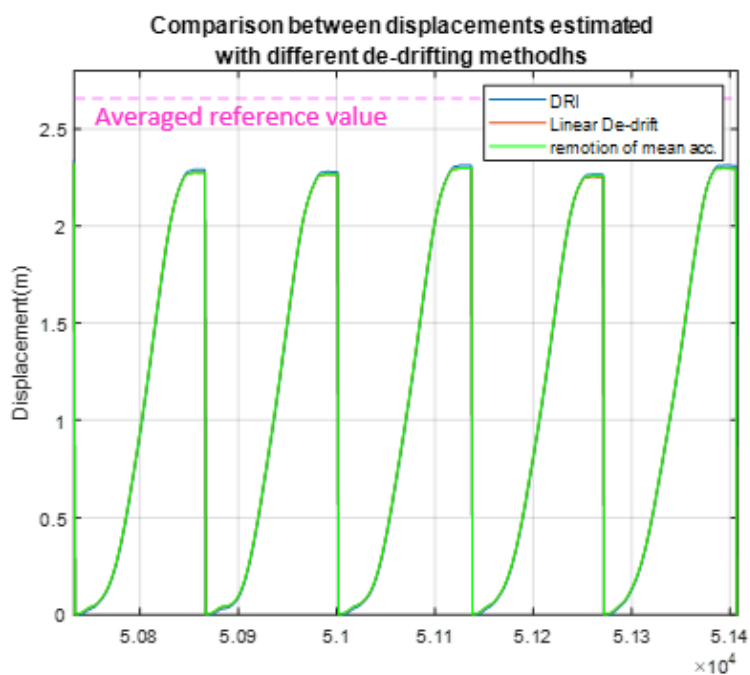


Figure 4.35: Comparison between displacements estimated with different de-drifting methods, for the dataset at 14km/h.

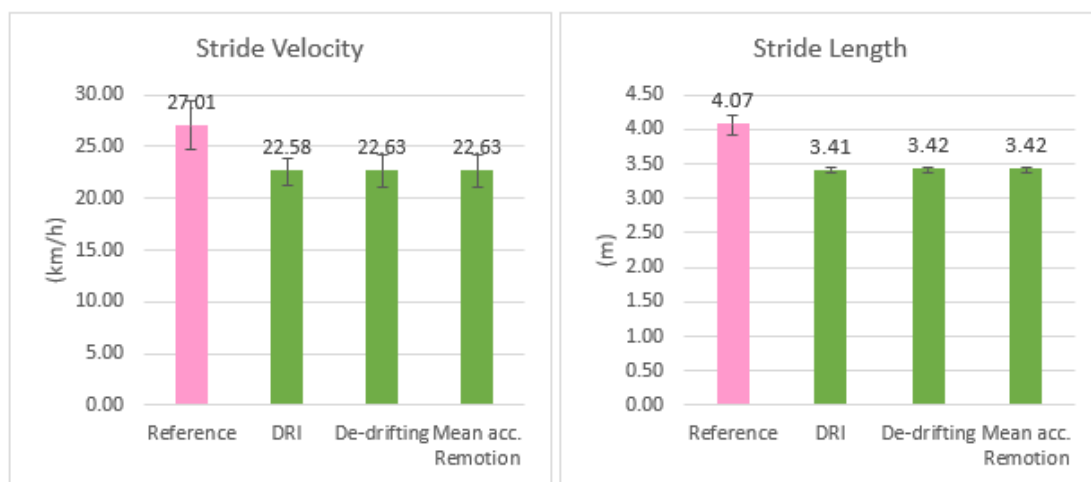


Figure 4.36: Comparison between SV and SL derived from the GoPro and those obtained with different de-drifting methods.

baseline pipeline and optimised one was depicted in Figure 4.42 and Figure 4.43 .

At this stage, it is possible also to evaluate the impact on the total trajectory in

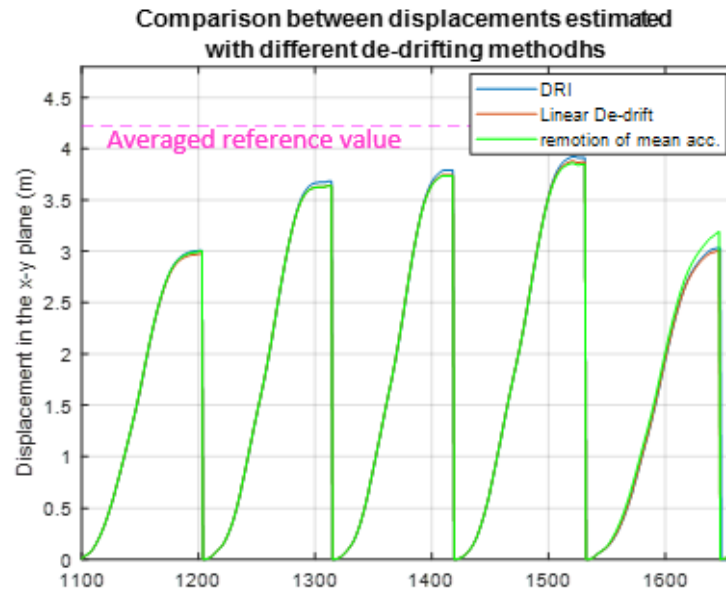


Figure 4.37: Comparison between displacements estimated with different de-drifting methods, for the dataset at 19-29 km/h.



Figure 4.38: Comparison between SV and SL derived from the SP, with the baseline and the optimised pipeline, for the dataset at 14 km/h.

the horizontal plane, as shown in figure 4.44.

Table 4.13: Results regarding the SV and SL with the different de-drifting methods, for the dataset at 14 km/h.

	Stride Velocity Errors			Stride Length Errors		
	ME (km/h)	MAE (km/h)	RMSE (km/h)	ME (m)	MAE (m)	RMSE (m)
Baseline Pipeline	-2.78 ± 0.68 (-19.69%±5.14%)	2.78 ± 0.68 (19.69%±5.14%)	2.78 ± 0.68	-0.92 ± 0.04 (-34.87%±2.02%)	0.92 ± 0.04 (34.87%±2.02%)	0.92 ± 0.04
Optimised Pipeline	-1.45 ± 0.45 (-10.40%±3.20%)	1.45 ± 0.45 (10.40%±3.20%)	1.45 ± 0.45	-0.39 ± 0.09 (-14.48%±3.41%)	0.39 ± 0.09 (14.48%±3.41%)	0.39 ± 0.09

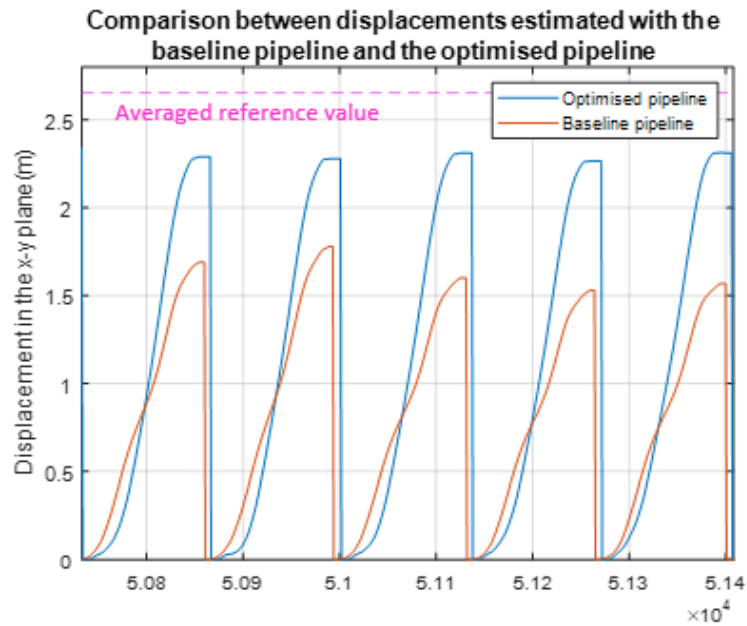


Figure 4.39: Comparison between the displacements at the initial stage of the optimisation process (in red) and those at the end (in blue).

Dataset at 19-29 km/h

At the end of the optimisation process, the MV over the trial is evaluated and compared with the MV found with the baseline pipeline and with the reference. In the bar chart in Figura 4.45 it is possible to compare the results.

Also, for the stride-by-stride calculated parameters, there is an overview of the change between the basic and optimised pipeline in Figure 4.46.

In Table 4.14 the numerical comparison in terms of ME, MAE and RMSE of the baseline and optimised pipeline is reported for this dataset. With the baseline pipeline, there was an RMSE error of 7.26 km/h for SV, which decreased to 3.97 km/h with the optimised pipeline, while it went from 1.27m to 0.58m for SL from

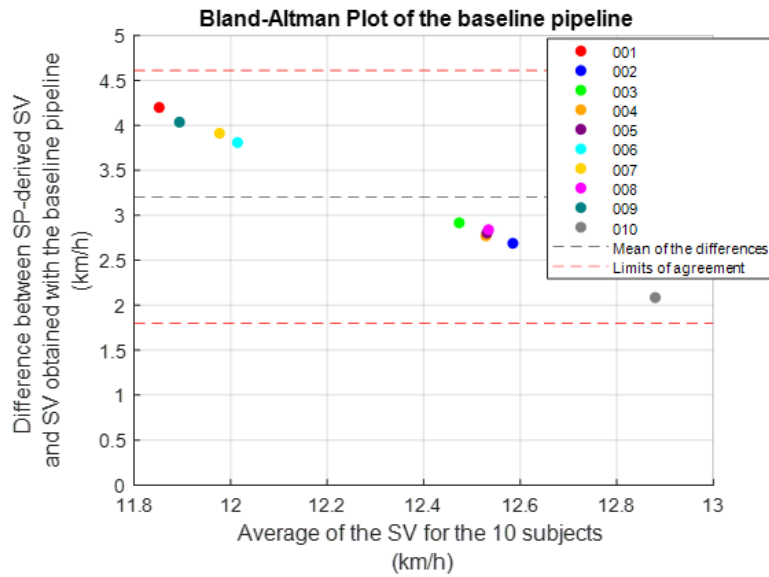


Figure 4.40: Bland Altman plot of all subjects in the dataset comparing SV from the SP and with the use of the baseline pipeline.

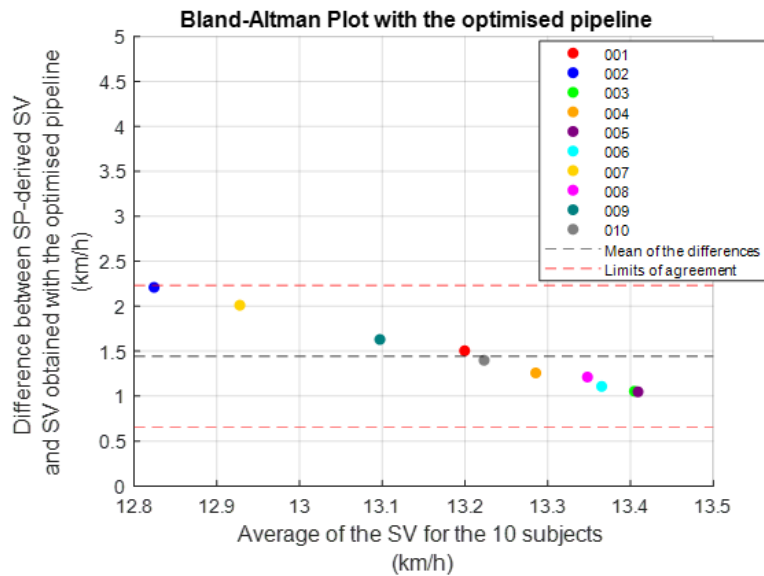


Figure 4.41: Bland Altman plot of all subjects in the dataset comparing SV from SP and with the use of the optimised pipeline.

the baseline pipeline to the optimised one.

In Figure 4.47 it is possible to compare the displacement in the x-y plane

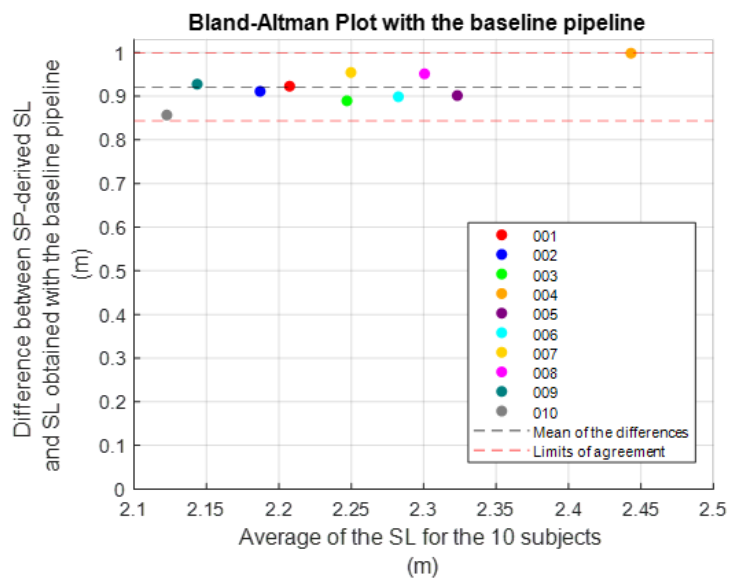


Figure 4.42: Bland Altman plot of SL of all subjects in the dataset comparing SP and the results of the baseline pipeline (dataset 14km/h).

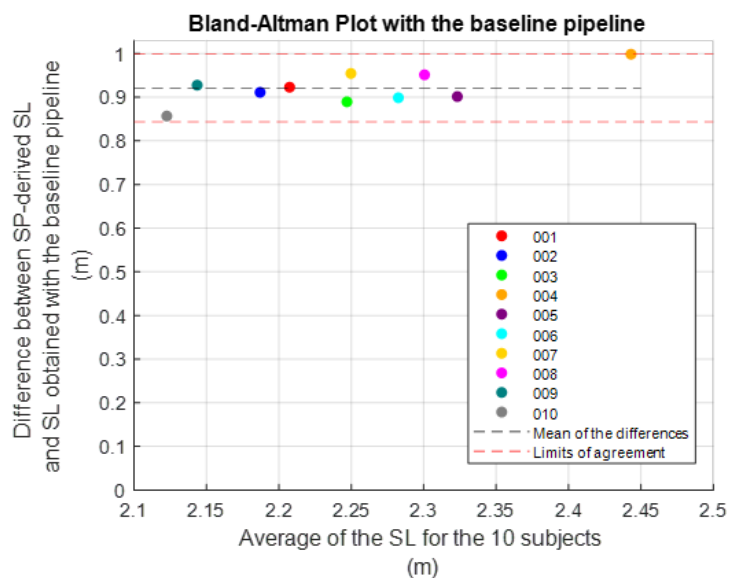


Figure 4.43: Bland Altman plot of SL of all subjects in the dataset comparing SP and the results of the optimised pipeline (dataset 14km/h).

estimated with the baseline pipeline and the optimised one.

The Bland-Altman plots are presented also for this dataset in terms of SV and

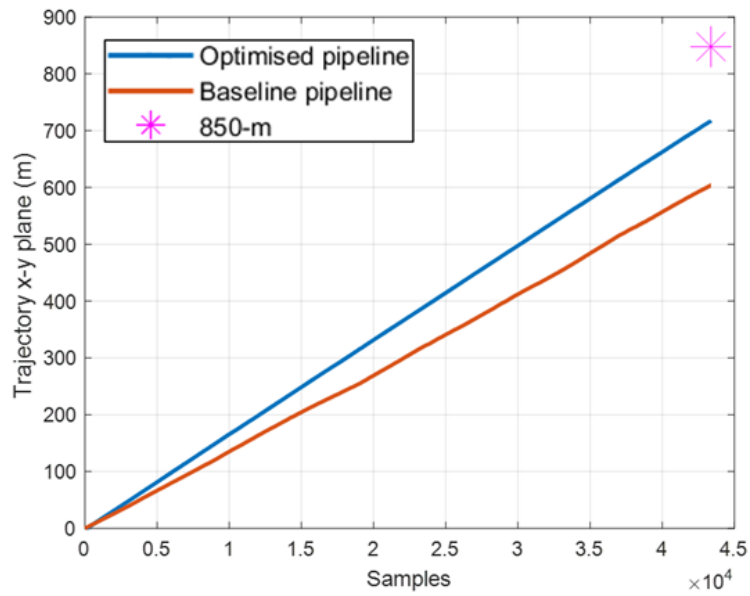


Figure 4.44: Comparison between the trajectories at the initial stage of the optimisation process (in red) and those at the end (in blu), for the dataset at 14 km/h.

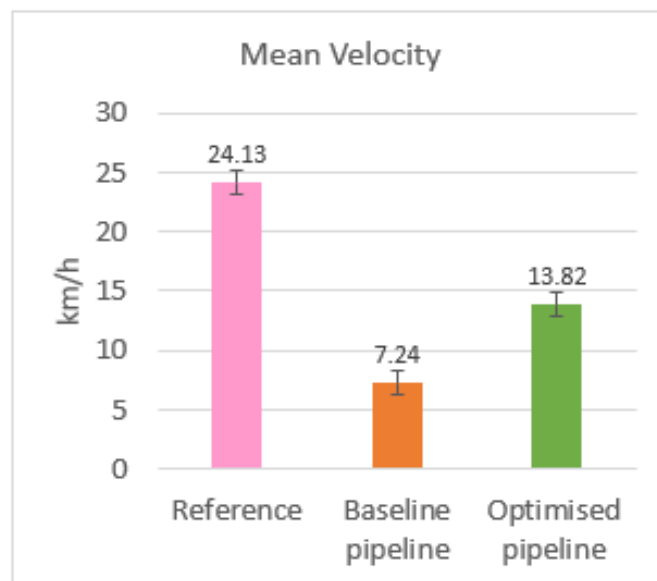


Figure 4.45: Comparison between MV, with the baseline and the optimised pipeline.

SL to evaluate the improvement between the baseline and optimised pipeline, across

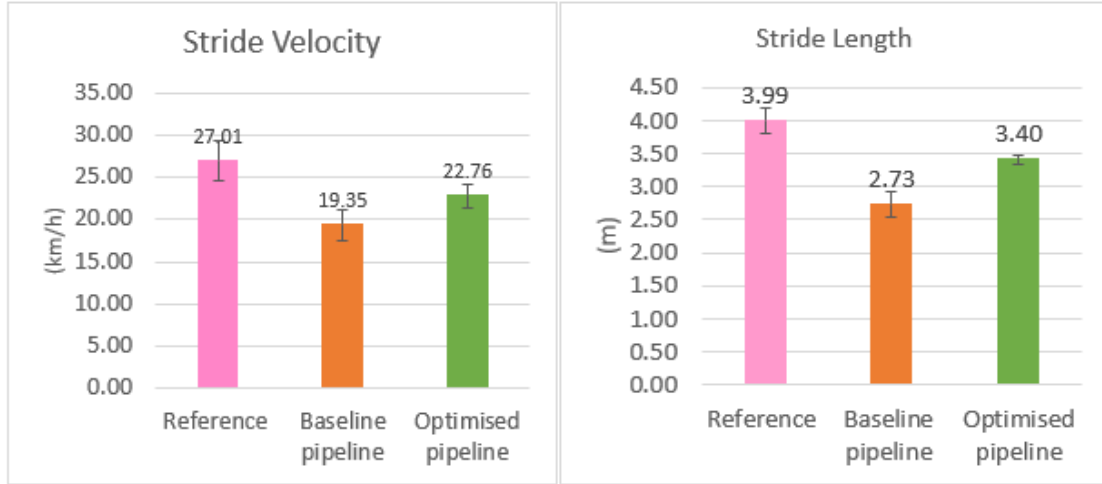


Figure 4.46: Comparison between SV and SL derived from the GoPro, with the baseline and the optimised pipeline.

Table 4.14: . Results regarding the SV and SL with the baseline and the optimised pipeline, for the dataset at 19-29 km/h.

	Stride Velocity Errors			Stride Length Errors		
	ME (km/h)	MAE (km/h)	RMSE (km/h)	ME (m)	MAE (m)	RMSE (m)
Baseline Pipeline	-7.38 ± 2.06 (-22.31%±4.27%)	7.38 ± 2.06 (-22.31%±4.27%)	7.38 ± 2.06	-1.27 ± 0.35 (-31.12%±7.33%)	1.27 ± 0.35 (-31.12%±7.33%)	1.27 ± 0.35
Optimised Pipeline	-3.9 ± 1.37 (-14.33%±4.16%)	3.9 ± 1.37 (14.33%±4.16%)	3.9 ± 1.37	-0.58 ± 0.15 (-14.93%±3.69%)	0.58 ± 0.15 (14.93%±3.69%)	0.58 ± 0.15

the 7 subject analysed (from Figure 4.48 to 4.51).

In general, in Figure 4.52 it is possible to compare the trajectory obtained with the baseline pipeline (in red) and the pipeline optimised in this work. The reference trajectory is the 50 meters that the runners covered in the trials.

4.3 Statistical Analysis

The t-test, a common statistical method, is typically utilised to examine whether there is a significant difference between two separate groups, particularly when the sample size is too small for more precise statistical analyses [72]. The t-test has been performed by taking into consideration the RMSE errors in terms of SV and SL obtained via the baseline pipeline and optimised pipeline over the two different speeds analysed. It relies on the hypothesis that the distributions of the data on which it is used is normal. The normality of data distribution was

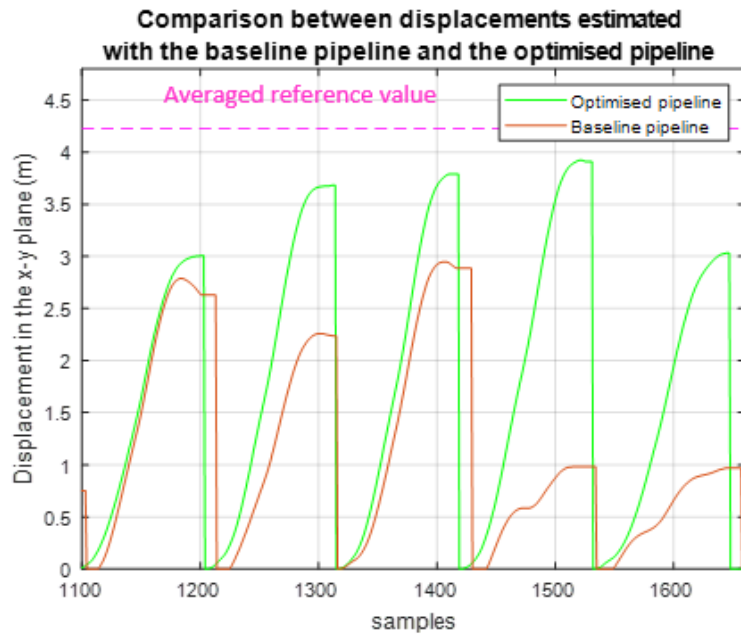


Figure 4.47: Comparison between the displacements at the initial stage of the optimisation process (in red) and those at the end (in green).

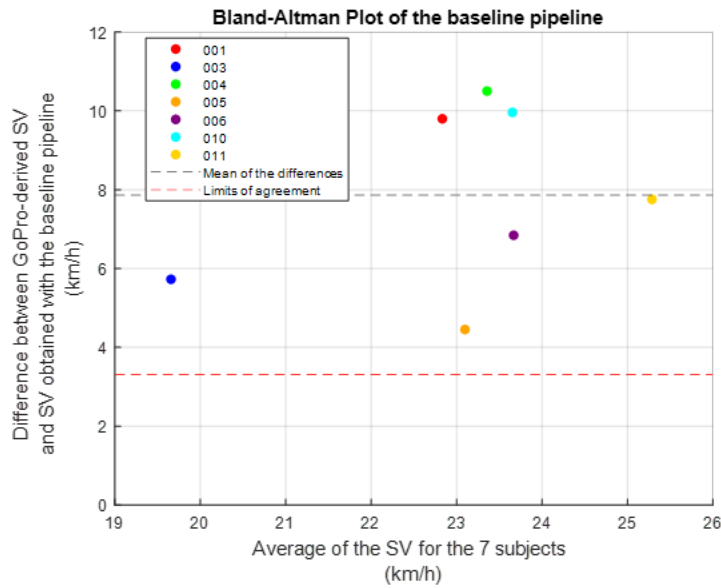


Figure 4.48: Bland Altman plot of SV of 7 subjects in the dataset comparing GoPro and the results of the baseline pipeline (dataset 19-29 km/h).

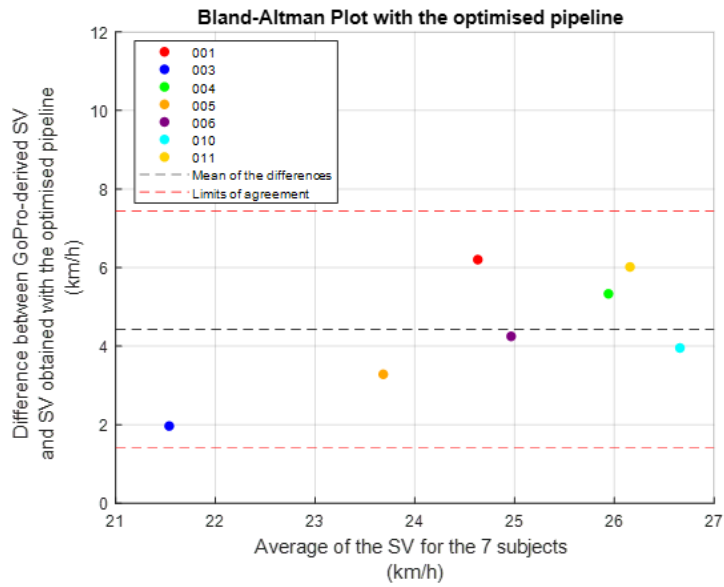


Figure 4.49: Bland Altman plot of SV of 7 subjects in the dataset comparing GoPro and the results of the optimised pipeline (dataset 19-29 km/h).

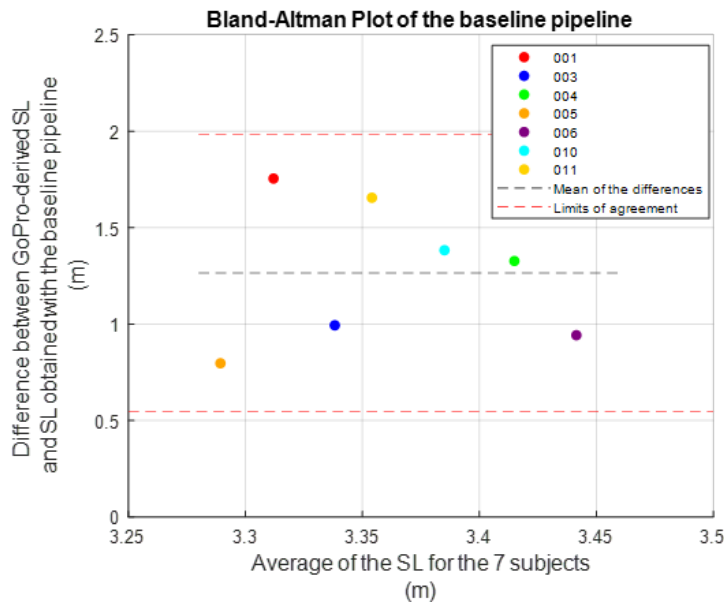


Figure 4.50: Bland Altman plot of SL of 7 subjects in the dataset comparing GoPro and the results of the baseline pipeline (dataset 19-29 km/h).

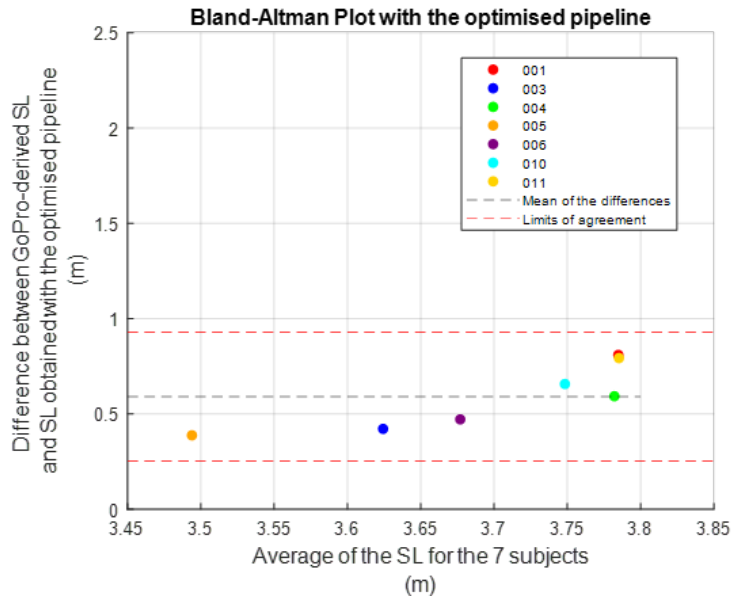


Figure 4.51: Bland Altman plot of SL of 7 subjects in the dataset comparing GoPro and the results of the optimised pipeline (dataset 19-29 km/h).

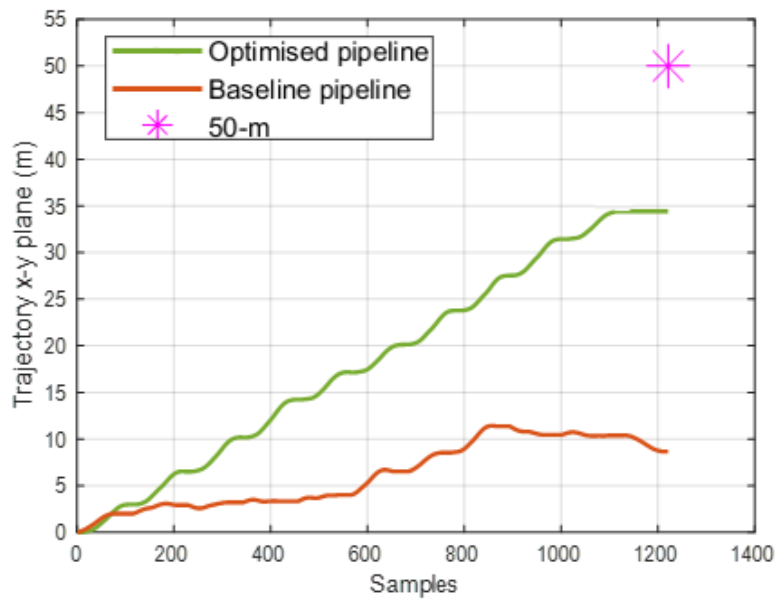


Figure 4.52: Comparison between the trajectories at the initial stage of the optimisation process (in red) and those at the end (in green), for the sprinting dataset.

investigated through Shapiro-Wilk test. As a result, the populations exhibited a normal distribution ($p < 0.05$), thus the t-test was suitable for the analysis. The aim for this test was to highlight whether the baseline and optimised pipeline returned statistically different results in terms of performance, which lead to the formulations of the two hypotheses to test:

- **H0**: null hypothesis, the methods are not different, $\bar{x}_1 - \bar{x}_1 = 0$
- **H1**: alternative hypothesis, the methods retain a statistical difference, $\bar{x}_1 - \bar{x}_1 \neq 0$

With \bar{x} being the grand means for the parameters of each population and 0 being the expected value for the null hypothesis, x_0 . Then the test statistic can be computed:

$$Test_{statistic} = \frac{(\bar{x}_1 - \bar{x}_1) - x_0}{\sqrt{\frac{s_1^2}{n_1} + \frac{s_2^2}{n_2}}} \quad (4.1)$$

The symbol s represents the overall standard deviation of the entire population, and n denotes its size. The resulting value needs to be compared to a p-value, which signifies the probability of the test result being accurate. For each chosen p-value, a corresponding confidence interval is established. The frequently employed p-value is 0.05, aligning with a 95% confidence interval. Speaking of the results, that are shown in Table 4.16, it can be noted that the value of the p-value is for both parameters lower than the chosen p-value (0.05) for all the speeds, leading to the conclusion that the null hypothesis can be rejected for all the parameters considered, thus a statistical difference between the two methods was detected.

Table 4.15: Statistical test results over the two dataset on SV and SL for evaluating the statistical differences between baseline and optimised pipeline.

	SV RMSE (km/h)			SL RMSE (m)		
	Baseline	Optimised	p-value	Baseline	Optimised	p-value
14 km/h	2.75	1.58	<0.01*	0.92	0.39	<0.01*
19-29 km/h	8.08	4.05	<0.01*	1.44	0.64	<0.01*

*significant difference ($p < 0.05$).

In addition, a t-test was conducted to assess whether the variation in speed influenced the results obtained in terms of RMSE error for SV and SL using the pipeline. For both parameters, a p-value lower than 0.05 was found, indicating that the speed has an impact on the outcome obtained with the optimised pipeline.

Table 4.16: *Statistical test results over the two dataset on SV and SL, for evaluating the statistical difference between the two dataset with the same optimised pipeline.*

	SV (km/h)			SL (m)		
	14 km/h	19-29 km/h	p-value	14 km/h	19-29 km/h	p-value
RMSE	1.58	4.05	0.003*	0.39	0.64	0.014*

*significant difference ($p < 0.05$).

Chapter 5

Discussion

In this study, an optimisation procedure for the estimation of SV and SL during running from wearable MIMUs was proposed [36]. In the literature different approaches for the estimation of those parameters have been proposed. However, the state-of-the-art methods have been largely tested on walking [[36], [33], [73] or specific running speed. In this work, each step of the most used pipeline for the estimation of SV and SL with inertial data was analysed with the aim to minimise the errors on the foot displacement and velocity at different running speeds (from 14 to 29 km/h). To quantify the improvement, the results using the baseline and the optimised pipeline were compared.

5.1 Performance of the baseline pipeline

First, the performance of the baseline pipeline for the estimation of the spatio-temporal parameters were assessed. Looking at the bar charts related to the SV and SL (Figura 4.1, Figura 4.4), it is evident that the baseline pipeline optimised for walking analysis [36] was not suitable for running as it heavily underestimated the parameters. Furthermore, the MV in sprinting estimated with the baseline pipeline is highly underestimated compared to the reference. At 14 km/h, as it can be seen in Table 4.1, SV shows RMSE errors of 2.75 km/h against an average reference speed of 14 km/h, with a MAE% of almost 20%. Regarding SL, errors are just below one meter, with an RMSE of 92 cm (and a MAE% ~35%), based on an average reference length of 2.7 m. For sprinting, there is an average underestimation of almost 7 km/h in the mean SV against a reference of the nominal SV provided by using the stopwatch, which is 24.3 km/h, obtaining a mean SV of 18.7km/h. Concerning stride-by-stride calculated errors, errors on SV estimation exceeded 7 km/h (with a MAE% of 21%), and SL was underestimated by 1.43 meters, against an average reference value of 4.05 m, with a MAE% exceeding 35% (Table

4.2). From the graph in Figure 4.2, the displacement evaluated at 14 km/h in the horizontal plane was underestimated, while the vertical displacement is heavily overestimated. In Figure 4.5, for the sprint running (19-29 km/h), this issue was amplified.

5.2 Performance of the optimised pipeline

5.2.1 Zero Velocity Detectors

In the literature, there is no ample agreement about the use of ZUPT in running ([35],[37]). For this reason, multiple methods have been implemented to detect intervals where foot can be assumed to be stationary. Therefore, the detectors most used in the literature were implemented, and the ZUPT intervals detected were compared with those obtained using the available references. Observing and the overlaps of the ZUPT intervals of the different implemented detectors and the reference ZUPT intervals, it was evident that the ARE [13] (i.e., the ZUPT detector used in the baseline pipeline), SHOE [13], and parametric detectors were comparable to the reference ([36]), while MV and MAG detectors over-estimated non-feasible ZUPT intervals using a fixed threshold ([13]). For this reason, the MV, MAG detectors [13] and the detector by Ma et al. [60] have been excluded from further analysis, their use is not recommended for running applications. For SHOE, ARE, and the parametric detectors, the overlap of the estimated ZUPT intervals with the reference ones was higher equal or higher than 95.5% (Table 4.3 and Table 4.5). ARE and SHOE depend on fixed thresholds detectors, and multiple attempts were conducted to determine sub-optimal thresholds for different speeds. The detector that minimised the errors on SV and SL was the parametric one. At 14 km/h, the MAE% error in SV decreased from 19% with the baseline pipeline to 14% (RMSE from 2.8 km/h to 2.1 km/h), while the SL error decreased from 35% to 18% (from 92 cm to 48 cm) (Table 4). In sprinting, the SV error decreased from 21% to 13% (from 7.3 km/h to 4.3 km/h), and the SL error decreased from 35% to 18% (from 1.43 m to 0.73 m) (Table 4.6). Furthermore, the parametric detector avoided the need for fine-tuning a fixed speed-dependant threshold, thus being a more robust solution across different speeds.

5.2.2 Selection of integration boundaries of the integration interval

Within ZUPT intervals, boundary conditions are selected for the double integration of the acceleration data. In the baseline pipeline, the integration instants were taken at 50% of the ZUPT interval [48], resulting in averaged underestimation of SV and SL equal to 13.9% and 17.8%, respectively for the dataset at 14km/h.

In the sprinter dataset, the errors were 14.1% and 17.8% for SV and SL. The attempts to define the integration instants at the end of the ZUPT interval [36] or at least kinetic energy [49] for both datasets did not improve the performances. The choice that minimised the SV and SL errors was the definition of the integration instants at the minimum of the norm of the moving averaged angular velocity within a ZUPT interval. With this novel definition of the integration boundaries the errors on SV and SL decreased by 3.5% and 3.2% reaching 1.76 km/h and 0.39 m, respectively.

5.2.3 Orientation estimation and gravity removal

The orientation estimation is for a key-point in assessing spatio-temporal parameters using MIMU. In this work, Madgwick filter was chosen for orientation estimation[11], since it enabled the tuning a single parameter. The results of the comparison between the quaternion initialisation method proposed by Valenti et al. [57] and the one proposed by Suzuki et al. [66], confirmed that the use of the algebraic quaternion by Valenti was advantageous, as in the baseline pipeline. Indeed, the use of Suzuki’s method degraded the performance both in terms of SV and SL estimation. The use of the magnetometer slightly decreased the performance in indoor trials, thus it was not involved in the orientation estimation. A fine-tuning of Madgwick’s β parameter for both analysed running speeds was performed. The baseline β value was 0.0019 rad/s, which was the optimal value for walking analysis [36] β values minimised the RMSEs on SV and SL were selected as the optimal values. At 14 km/h, the best β was 0.008 rad/s, while for the sprint running dataset, the optimal β was 0.01 rad/. To define a unique β that could be adopted in the entire tested speed range (14-29 km/h), a compromise β of 0.0085 rad/s was selected.

At this stage of the optimisation process, a method to assess the reliability of the foot stationary at the integration instants was implemented. The basic idea was to deem a stationary instant unreliable if the corresponding acceleration and angular rate values exceeded an empirical threshold depending on speed, thus the orientation re-initialisation did not take place. The use of these reliability checks did not yield a considerable improvement in results Therefore, this step required further investigation.

5.2.4 Results of the comparison of the methods for velocity drift removal

This analysis was conducted to confirm the equivalence among various techniques for de-drifting velocity. Indeed, no differences are observed in the results obtained with DRI[51], linear de-drifting[50], and removal of the mean acceleration value[69],

as it can be seen in Figure 4.34. It can be stated that the use of these techniques is equivalent at any running speed.

5.2.5 Final comparison between the baseline pipeline and the optimised pipeline

The overall optimised pipeline for calculating SV and SL enabled an improvement in the SV and SL estimation of 16.4%-22.2% and 29.6%-28.9% respectively.

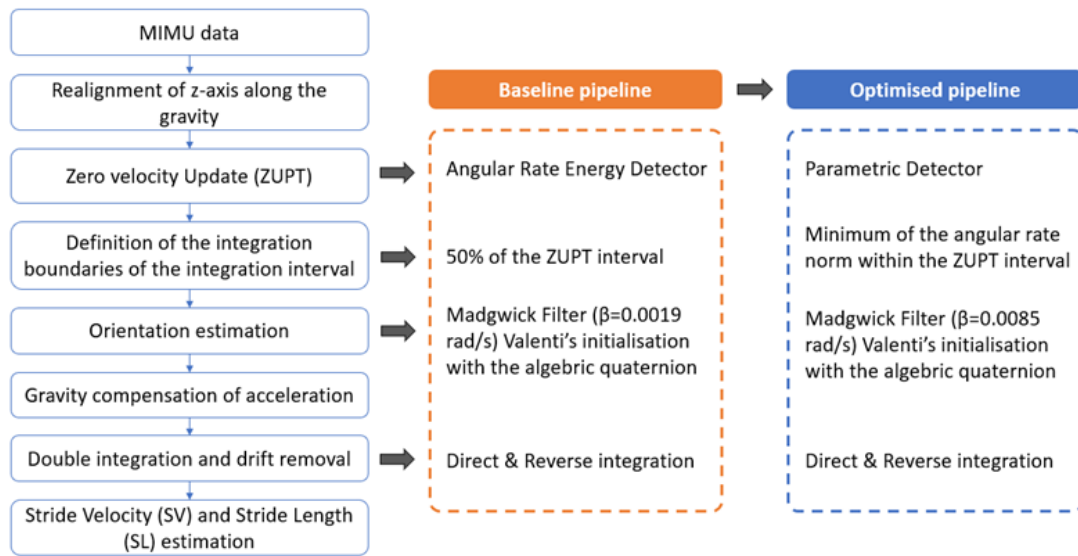


Figure 5.1: Block diagram summarising the stages of the pipeline, explicitly showing, on the right, the algorithms employed in the baseline and optimised pipeline.

Table 14 provides the results of the metrics estimated at 14 km/h, showing a reduction in RMSE error for SV from 2.75 km/h to 1.75 km/h and for SL from 92 cm to 39 cm. In sprinting, Table 15 shows a decrease in RMSE error from 7.26 km/h to 3.67 km/h for SV and from 1.43 m to 0.65 m for SL. For both datasets, the graphic representation of the displacement in the horizontal plane estimated with the baseline and optimised pipeline are reported in Figure 4.39 and Figure 4.46, with the respective averaged reference value from the Gold Standards utilised. In both datasets, it is noticeable that the horizontal displacement is closer to the reference when using the optimised pipeline. The Bland-Altman plots for SV and SL at the beginning and end of the optimisation revealed a significant reduction in the underestimation of both SV and SL within the whole running speed range (14-29 km/h) ($p < 0.05$).

The most influent step of the pipeline was the ZUPT detector, whose only optimisation led to an improvement of 11.8% for SV and 24.1% for SL at 14km/h, while an improvement of 13.5% for SV and 28.4% SL during sprinting. However, the errors obtained with the optimised pipeline were still high (equal to about 10.4%-14.3% on SV and 14.4%-16.2% on SL due to an orientation estimation that is still not optimal, that decreased the accuracy of gravity compensation leading to an underestimation of the displacement on the horizontal plane.

Thus, to attempt to address the issue, as future developments, some methods are suggested for investigation. The introduction of specialised reliability checks on the integration instants of integration for orientation estimations to improve accuracy. The implementation of Kalman filters (KFs) estimating foot orientation, velocity and displacement for a more comprehensive analysis. Developing methods to address the underestimation of horizontal velocity and displacement by leveraging the overestimation in the vertical dimension, considering the assumption of level running surfaces. Exploring the potential benefits of increasing the sampling frequency, particularly in sprinting evaluations.

Chapter 6

Conclusions

This study focused on the improvement of a state-of-the-art pipeline for foot displacement estimation optimising each step to minimise errors on SV and SL during running at different speeds (14-29 km/h). The study highlighted the importance of the optimisation procedure to target MIMU-based methods for the estimation of spatio-temporal parameters to a wide range of running speeds. The overall improvement was equal to 16.4% for SV and 29.6% for SL at 14 km/h, while 13.8% for SV and 30.4% for SL during sprinting. The suggested parametric ZUPT detector defined the ZUPT intervals on the moving average of the angular rate. Increasing the running speed, the initialisation of orientation became more critical. Therefore, it is recommended to calculate the algebraic quaternion at each minimum of the moving-averaged angular rate norm within the ZUPT interval, as the vertical axis is better aligned with gravity. In the orientation estimation process, Madgwick's β parameter demonstrated varying optimal values across different speeds. A suggested compromise value is 0.0085 rad/s. Even if the overall errors on SV and SL were significantly influenced by speed and still considerably high (10.3%- 14.3% and 14.4%- 14.8%), the proposed optimised pipeline represents a remarkable starting point for the analysis of spatio-temporal parameters during running at different speeds using foot-mounted magneto-inertial sensors. However, the orientation estimation is still not optimal, thus decreasing the accuracy of gravity compensation and leading to an underestimation of the displacement on the horizontal plane. Future work should focus on the improvement of the orientation estimation, assuming that the running is usually level ground.

Bibliography

- [1] Jay Schulkin. «Evolutionary Basis of Human Running and Its Impact on Neural Function». In: *Frontiers in Systems Neuroscience* 10 (2016). ISSN: 1662-5137. DOI: 10.3389/fnsys.2016.00059. URL: <https://www.frontiersin.org/articles/10.3389/fnsys.2016.00059> (cit. on p. 1).
- [2] Jack Taunton, Michael Ryan, D Clement, Don Mckenzie, D Lloyd-Smith, and Bruno Zumbo. «A retrospective case-control analysis of 2002 running injuries». In: *British journal of sports medicine* 36 (May 2002), pp. 95–101. DOI: 10.1136/bjism.36.2.95 (cit. on p. 1).
- [3] C. Markus Brahms, Yang Zhao, David Gerhard, and John M. Barden. «Stride length determination during overground running using a single foot-mounted inertial measurement unit». In: *Journal of Biomechanics* 71 (2018), pp. 302–305. ISSN: 0021-9290. DOI: <https://doi.org/10.1016/j.jbiomech.2018.02.003>. URL: <https://www.sciencedirect.com/science/article/pii/S0021929018300885> (cit. on pp. 1, 39, 40).
- [4] G. Balestra V. Agostini and M. Knaflitz. «Segmentation and classification of gait cycles». In: *IEEE Transactions on Neural Systems and Rehabilitation Engineering* 22 (Sept. 2014), pp. 946–952. DOI: 10.1109/TNSRE.2013.2291907. (cit. on p. 3).
- [5] Markus Zrenner. «From Raw to Big Data in Endurance Running : Application of Data Science Techniques for Knowledge Creation from Wearable Sensor Data». PhD thesis. Jan. 2022. DOI: 10.25593/978-3-96147-539-1 (cit. on p. 3).
- [6] M. E. Kasmer, X.-C. Liu, K. G. Roberts, and J. M. Valadao. «Foot-strike pattern and performance in a marathon». In: (2018) (cit. on p. 3).
- [7] T. F. Novacheck. «The biomechanics of running». In: *Gait & Posture* 7.1 (1998), pp. 77–95 (cit. on p. 4).

- [8] Sheila A. Dugan and Krishna P. Bhat. «Biomechanics and analysis of running gait.» In: *Physical medicine and rehabilitation clinics of North America* 16 3 (2005), pp. 603–21. URL: <https://api.semanticscholar.org/CorpusID:13474687> (cit. on pp. 4, 5).
- [9] Gazzoni Marco and Botter Alberto. «Slide del corso di Bioingegneria della Riabilitazione». Politecnico di Torino (cit. on pp. 7–9).
- [10] Kathleen Lamkin-Kennard and Marko Popovic. «Sensors: Natural and Synthetic Sensors». In: Apr. 2019, pp. 81–107. ISBN: 9780128129395. DOI: 10.1016/B978-0-12-812939-5.00004-5 (cit. on p. 9).
- [11] Frazier DM. Dingwell JB Davis BL. «Use of an instrumented treadmill for real-time gait symmetry evaluation and feedback in normal and trans-tibial amputee subjects». In: 2 (1996), pp. 101–110. DOI: doi:10.3109/03093649609164426 (cit. on p. 10).
- [12] *Optojump*. URL: <http://www.optojump.com/cos-e-optojump.aspx> (cit. on p. 11).
- [13] I. Skog, P. Händel, J. O. Nilsson, and J. Rantakokko. «Zero-velocity detection- An algorithm evaluation». In: *IEEE Trans Biomed Eng* 57.11 (Nov. 2010), pp. 2657–2666. DOI: 10.1109/TBME.2010.2060723 (cit. on pp. 12, 34, 52, 57, 92).
- [14] Rachel E. Horenstein, Cara L. Lewis, Siobhan Yan, Amy Halverstadt, and Sandra J. Shefelbine. «Validation of magneto-inertial measuring units for measuring hip joint angles». In: *J Biomech* 91 (June 2019), pp. 170–174. DOI: 10.1016/j.jbiomech.2019.05.029 (cit. on p. 12).
- [15] Martina Bertoli, Andrea Cereatti, Diana Trojaniello, and et al. «Estimation of spatio-temporal parameters of gait from magneto-inertial measurement units: multicenter validation among Parkinson, mildly cognitively impaired and healthy older adults». In: *Biomed Eng Online* 17.1 (May 2018), p. 58. DOI: 10.1186/s12938-018-0488-2 (cit. on p. 12).
- [16] Valentina Camomilla, Elena Bergamini, Silvia Fantozzi, and Giuseppe Vannozzi. «Trends Supporting the In-Field Use of Wearable Inertial Sensors for Sport Performance Evaluation: A Systematic Review». In: *Sensors* 18 (Mar. 2018), p. 873. DOI: 10.3390/s18030873 (cit. on p. 12).
- [17] Ryu Nagahara, Masashi Kameda, Jonathan Neville, and Jean-Benoit Morin. «Inertial measurement unit-based hip flexion test as an indicator of sprint performance». In: *J Sports Sci* 38.1 (Jan. 2020), pp. 53–61. DOI: 10.1080/02640414.2019.1680081 (cit. on p. 12).

- [18] Giuseppe Pacini Panebianco, Maria Cristina Bisi, Rita Stagni, and Silvia Fantozzi. «Analysis of the performance of 17 algorithms from a systematic review: Influence of sensor position, analysed variable and computational approach in gait timing estimation from IMU measurements». In: *Gait Posture* 66 (Oct. 2018), pp. 76–82. DOI: 10.1016/j.gaitpost.2018.08.025 (cit. on p. 13).
- [19] Markus Zrenner, Anne Küderle, Niklas Roth, Ulf Jensen, Benjamin Dümmler, and Björn M. Eskofier. «Does the position of foot-mounted IMU sensors influence the accuracy of spatio-temporal parameters in endurance running?» In: *Sensors (Switzerland)* 20.19 (Oct. 2020), pp. 1–21. DOI: 10.3390/s20195705 (cit. on pp. 12, 13).
- [20] Ben J. Horsley et al. «Does Site Matter? Impact of Inertial Measurement Unit Placement on the Validity and Reliability of Stride Variables During Running: A Systematic Review and Meta-analysis». In: *Sports Medicine* 51.7 (July 2021), pp. 1449–1489. DOI: 10.1007/s40279-021-01443-8 (cit. on p. 12).
- [21] Zainul Mohammed, I. (Abe) M. Elfadel, and Mona Rasras. «Monolithic multi degree of freedom (MDoF) capacitive MEMS accelerometers». In: *Micromachines* 9.11 (2018). DOI: 10.3390/mi9110602 (cit. on p. 14).
- [22] Matthew J. Mathie, Andrew C. F. Coster, Nigel H. Lovell, and Branko G. Celler. «Accelerometry: Providing an integrated, practical method for long-term, ambulatory monitoring of human movement». In: *Physiological Measurement* 25.2 (2004). DOI: 10.1088/0967-3334/25/2/R01 (cit. on p. 15).
- [23] Riccardo Antonello and Roberto Oboe. «MEMS Gyroscopes for Consumers and Industrial Applications». In: June 2011. ISBN: 978-953-307-170-1. DOI: 10.5772/17689 (cit. on p. 16).
- [24] Y. S. Meng and Y. H. Lee. «Study of shadowing effect by aircraft maneuvering for air-to-ground communication». In: *AEU - International Journal of Electronics and Communications* 66.1 (Jan. 2012), pp. 7–11. DOI: 10.1016/j.aeue.2011.04.006 (cit. on p. 16).
- [25] V. M. N. Passaro, A. Cuccovillo, L. Vaiani, M. De Carlo, and C. E. Campanella. «Gyroscope technology and applications: A review in the industrial perspective». In: *Sensors (Switzerland)* 17.10 (Oct. 2017), p. 2284. DOI: 10.3390/s17102284 (cit. on p. 16).
- [26] CEVA-DSP. *Exploring the Application of Gyroscopes*. [Online; accessed il tuo accesso qui]. URL: <https://www.ceva-dsp.com/ourblog/exploring-the-application-of-gyroscopes/> (cit. on p. 17).

- [27] *Hall Effect*. <http://hyperphysics.phy-astr.gsu.edu/hbase/magnetic/Hall.html> (cit. on p. 19).
- [28] E. Martini and altri. «Pressure-sensitive insoles for real-time gait-related applications». In: *Sensors (Switzerland)* 20.5 (Mar. 2020). DOI: 10.3390/s20051448 (cit. on p. 19).
- [29] Abdul Razak, Aladin Zayegh, Rezaul Begg, and Yufridin Wahab. «Foot Plantar Pressure Measurement System: A Review». In: *Sensors (Basel, Switzerland)* 12 (Dec. 2012), pp. 9884–9912. DOI: 10.3390/s120709884 (cit. on p. 19).
- [30] Fahni Haris, Ben-Yi Liao, Yih-Kuen Jan, Veit Babak Hamun Akbari, Yanuar Primanda, Kuan-Han Lin, and Chi-Wen Lung. «A Review of the Plantar Pressure Distribution Effects from Insole Materials and at Different Walking Speeds». In: *Applied Sciences* 11.24 (2021). ISSN: 2076-3417. DOI: 10.3390/app112411851. URL: <https://www.mdpi.com/2076-3417/11/24/11851> (cit. on p. 19).
- [31] Rene El Kati, Steph Forrester, and Paul Fleming. «Evaluation of pressure insoles during running». In: *Procedia Engineering* 2.2 (2010). The Engineering of Sport 8 - Engineering Emotion, pp. 3053–3058. ISSN: 1877-7058. DOI: <https://doi.org/10.1016/j.proeng.2010.04.110>. URL: <https://www.sciencedirect.com/science/article/pii/S1877705810003644> (cit. on p. 20).
- [32] F. Salis and altri. «A multi-sensor wearable system for the assessment of diseased gait in real-world conditions». In: *Front Bioeng Biotechnol* 11 (2023). DOI: 10.3389/fbioe.2023.1143248 (cit. on pp. 20, 32, 34, 39).
- [33] F. Salis and altri. «A wearable multi-sensor system for real-world gait analysis». In: *Proceedings of the Annual International Conference of the IEEE Engineering in Medicine and Biology Society, EMBS*. Institute of Electrical and Electronics Engineers Inc. 2021, pp. 7020–7023. DOI: 10.1109/EMBC46164.2021.9630392 (cit. on pp. 20, 32, 91).
- [34] L. E. Diez, A. Bahillo, J. Otegui, and T. Otim. «Step Length Estimation Methods Based on Inertial Sensors: A Review». In: *IEEE Sens J* 18.17 (Sept. 2018), pp. 6908–6926. DOI: 10.1109/JSEN.2018.2857502 (cit. on p. 21).
- [35] M. Zrenner, S. Gradl, U. Jensen, M. Ullrich, and B. M. Eskofier. «Comparison of different algorithms for calculating velocity and stride length in running using inertial measurement units». In: *Sensors (Switzerland)* 18.12 (Dec. 2018). DOI: 10.3390/s18124194 (cit. on pp. 21, 27, 39, 92).

- [36] R. Rossanigo, M. Caruso, F. Salis, S. Bertuletti, U. Della Croce, and A. Cereatti. «An optimal procedure for stride length estimation using foot-mounted magneto-inertial measurement units». In: *2021 IEEE International Symposium on Medical Measurements and Applications, MeMeA 2021 - Conference Proceedings*. Institute of Electrical and Electronics Engineers Inc. June 2021. DOI: 10.1109/MeMeA52024.2021.9478604 (cit. on pp. 22, 27, 33, 34, 38, 39, 41, 52, 57, 62, 91–93).
- [37] C. J. de Ruiter and altri. «Stride Lengths during Maximal Linear Sprint Acceleration Obtained with Foot-Mounted Inertial Measurement Units». In: *Sensors* 22.1 (Jan. 2022). DOI: 10.3390/s22010376 (cit. on pp. 22, 27, 41, 92).
- [38] S.O.H. Madgwick. «2011 IEEE International Conference on Rehabilitation Robotics». In: *IEEE International Conference on Rehabilitation Robotics*. IEEE. 2011 (cit. on pp. 23, 25, 34, 52).
- [39] T. Islam, M. S. Islam, M. Shajid-Ul-Mahmud, and M. Hossam-E-Haider. «Comparison of complementary and Kalman filter based data fusion for attitude heading reference system». In: *AIP Conference Proceedings*. American Institute of Physics Inc. Dec. 2017. DOI: 10.1063/1.5018520 (cit. on pp. 23–25).
- [40] A. M. Sabatini. «Estimating three-dimensional orientation of human body parts by inertial/magnetic sensing». In: *Sensors* 11.2 (Feb. 2011), pp. 1489–1525. DOI: 10.3390/s110201489 (cit. on p. 24).
- [41] R. E. Kalman. *A New Approach to Linear Filtering and Prediction Problems 1*. 1960. URL: <http://fluidsengineering.asmedigitalcollection.asme.org/> (cit. on p. 24).
- [42] M. I. Ribeiro. *Kalman and Extended Kalman Filters: Concept, Derivation and Properties*. 2004 (cit. on p. 25).
- [43] E. Bergamini, G. Ligorio, A. Summa, G. Vannozzi, A. Cappozzo, and A. M. Sabatini. «Estimating orientation using magnetic and inertial sensors and different sensor fusion approaches: Accuracy assessment in manual and locomotion tasks». In: *Sensors (Switzerland)* 14.10 (Oct. 2014), pp. 18625–18649. DOI: 10.3390/s141018625 (cit. on p. 25).
- [44] A. M. Sabatini. «Quaternion-based extended Kalman filter for determining orientation by inertial and magnetic sensing». In: *IEEE Transactions on Biomedical Engineering* 53.7 (July 2006), pp. 1346–1356 (cit. on p. 26).
- [45] E. Foxlin. «Pedestrian tracking with SHOE-mounted inertial sensors». In: *IEEE Computer Graphics and Applications* 25.6 (Nov. 2005), pp. 38–46 (cit. on p. 26).

- [46] H. M. Schepers, H. F. J. M. Koopman, and P. H. Veltink. «Ambulatory assessment of ankle and foot dynamics». In: *IEEE Transactions on Biomedical Engineering* 54.5 (May 2007), pp. 895–902 (cit. on p. 27).
- [47] I. Skog, J. O. Nilsson, and P. Händel. «Evaluation of zero-velocity detectors for foot-mounted inertial navigation systems». In: *2010 International Conference on Indoor Positioning and Indoor Navigation, IPIN 2010 - Conference Proceedings*. 2010. DOI: 10.1109/IPIN.2010.5646936 (cit. on p. 27).
- [48] G. García-Villamil, L. Ruiz, A. R. Jiménez, F. Seco, and M. C. Rodríguez-Sánchez. *Influence of IMU's Measurement Noise on the Accuracy of Stride-Length Estimation for Gait Analysis*. 2021. URL: <http://ceur-ws.org> (cit. on pp. 27, 34, 41, 62, 92).
- [49] J. Hannink, M. Ollenschläger, F. Kluge, N. Roth, J. Klucken, and B. M. Eskofier. «Benchmarking foot trajectory estimation methods for mobile gait analysis». In: *Sensors (Switzerland)* 17.9 (Sept. 2017). DOI: 10.3390/s17091940 (cit. on pp. 27, 41, 62, 93).
- [50] G. P. Bailey and R. Harle. «Assessment of foot kinematics during steady state running using a foot-mounted IMU». In: *Procedia Engineering*. Elsevier Ltd, 2014, pp. 32–37. DOI: 10.1016/j.proeng.2014.06.009 (cit. on pp. 28, 39, 49, 73, 93).
- [51] M. Zok, C. Mazzà, and U. Della Croce. «Total body centre of mass displacement estimated using ground reactions during transitory motor tasks: Application to step ascent». In: *Medical Engineering & Physics* 26.9 SPEC.ISS. (2004), pp. 791–798. DOI: 10.1016/j.medengphy.2004.07.005 (cit. on pp. 28, 34, 49, 52, 73, 93).
- [52] OPAL. *Mobility Lab User Guide* (cit. on p. 31).
- [53] R. Rossanigo et al. «Estimation of running biomechanical parameters using magneto-inertial sensors: a preliminary investigation». In: *Gait Posture* 97 (Oct. 2022), pp. 38–39. DOI: 10.1016/j.gaitpost.2022.09.063 (cit. on p. 31).
- [54] R. Rossanigo et al. «Estimation of temporal parameters using footworn inertial sensors for different running speeds». In: *Gait Posture* 105 (Oct. 2023), p. 41. DOI: 10.1016/j.gaitpost.2023.07.333 (cit. on pp. 31, 32, 36).
- [55] R. Nicola, G. L. Cerone, M. Caruso, R. Rossanigo, A. Cereatti, and T. Vieira. «On the Detection of High-Quality, High-Density Electromyograms During 80m Sprints: a Case Study». In: *2022 IEEE International Symposium on Medical Measurements and Applications, MeMeA 2022 - Conference Proceedings*. Institute of Electrical and Electronics Engineers Inc. 2022. DOI: 10.1109/MeMeA54994.2022.9856504 (cit. on p. 32).

- [56] G. L. Cerone, R. Nicola, M. Caruso, R. Rossanigo, A. Cereatti, and T. M. Vieira. «Running speed changes the distribution of excitation within the biceps femoris muscle in 80 m sprints». In: *Scand J Med Sci Sports* 33.7 (July 2023), pp. 1104–1115. DOI: 10.1111/sms.14341 (cit. on p. 32).
- [57] R. G. Valenti, I. Dryanovski, and J. Xiao. «Keeping a Good Attitude: A Quaternion-Based Orientation Filter for IMUs and MARGs». In: *Sensors (Switzerland)* 15.8 (Aug. 2015), pp. 19302–19330. DOI: 10.3390/s150819302 (cit. on pp. 34, 44, 48, 52, 65–67, 93).
- [58] E. Dipalma, P. Di Torino, M. Caruso, R. Rossanigo, R. N. Politecnico, and D. Torino. *Stride detection in running using foot-mounted magneto-inertial sensors: a preliminary investigation for different running paces*. Available online: <https://www.researchgate.net/publication/364359968>. 2023 (cit. on p. 36).
- [59] B. Utzeri et al. «Assessment and comparison of zero-velocity detectors under variations in running speed». In: *Proceedings SIAMOC 2023*. 2023, p. 149 (cit. on p. 36).
- [60] M. Ma, Q. Song, Y. Gu, Y. Li, and Z. Zhou. «An adaptive zero velocity detection algorithm based on multi-sensor fusion for a pedestrian navigation system». In: *Sensors (Switzerland)* 18.10 (Oct. 2018). DOI: 10.3390/s18103261 (cit. on pp. 37, 41, 60, 92).
- [61] Y. Wang and A. M. Shkel. «A Review on ZUPT-Aided Pedestrian Inertial Navigation». In: (2020) (cit. on p. 39).
- [62] Y. Li and J. Jack Wang. «A pedestrian navigation system based on low-cost IMU». In: *Journal of Navigation* 67.6 (Nov. 2014), pp. 929–949. DOI: 10.1017/S0373463314000344 (cit. on p. 39).
- [63] R. Zhang, H. Yang, F. Höflinger, and L. M. Reindl. «Adaptive Zero Velocity Update Based on Velocity Classification for Pedestrian Tracking». In: *IEEE Sens J* 17.7 (Apr. 2017), pp. 2137–2145. DOI: 10.1109/JSEN.2017.2665678 (cit. on p. 39).
- [64] M. Ren, K. Pan, Y. Liu, H. Guo, X. Zhang, and P. Wang. «A novel pedestrian navigation algorithm for a foot-mounted inertial-sensor-based system». In: *Sensors (Switzerland)* 16.1 (Jan. 2016). DOI: 10.3390/s16010139 (cit. on p. 39).
- [65] S. O. H. Madgwick. «An efficient orientation filter for inertial and inertial/magnetic sensor arrays». In: *Anno della pubblicazione o nome della rivista* (2010) (cit. on p. 42).

- [66] Y. Suzuki, M. E. Hahn, and Y. Enomoto. «Estimation of Foot Trajectory and Stride Length during Level Ground Running Using Foot-Mounted Inertial Measurement Units». In: *Sensors* 22.19 (Oct. 2022), p. 7129. DOI: 10.3390/s22197129 (cit. on pp. 44, 46, 49, 65–67, 93).
- [67] M. Caruso et al. «Towards an automatic parameter setting for MIMU sensor fusion algorithms». In: *Gait & Posture* 74.S1 (2019), S8 (cit. on p. 47).
- [68] M. Caruso, A. M. Sabatini, M. Knafitz, M. Gazzoni, U. Della Croce, and A. Cereatti. «Orientation Estimation through Magneto-Inertial Sensor Fusion: A Heuristic Approach for Suboptimal Parameters Tuning». In: *IEEE Sens J* 21.3 (2021), pp. 3408–3419. DOI: 10.1109/JSEN.2020.3024806 (cit. on p. 47).
- [69] Z. Wu, D. Yuan, F. Zhang, and M. Yao. «Improving Accuracy of Low-Cost Vehicle Attitude Estimation by Denoising MIMU Based on SSA and ICA». In: *IEEE Trans Instrum Meas* 70 (2021). DOI: 10.1109/TIM.2021.3064803 (cit. on pp. 49, 73, 93).
- [70] Edoardo Mercuri. «Collection of scripts and notebooks developed for "Machine Learning for Running Analysis with Wearable Inertial Sensors"». Master's Thesis. MA thesis. Politecnico di Torino, Nov. 2023. URL: <https://github.com/PIC4SeRThesis/EdoardoMercuri> (cit. on p. 49).
- [71] Edoardo Mercuri. «Machine Learning for Running Analysis with Wearable Inertial Sensors». Master's degree in MECHATRONIC ENGINEERING. Master's thesis. POLITECNICO DI TORINO, Department of ELECTRONICS and TELECOMMUNICATIONS (DET), 2023 (cit. on p. 49).
- [72] Tae Kyun Kim. *Statistic and Probability*. Available at: <http://ekja.org>. 2023 (cit. on p. 85).
- [73] A. J. Jocham, D. Laidig, B. Guggenberger, and T. Seel. «Measuring highly accurate foot position and angle trajectories with foot-mounted IMUs in clinical practice». In: *Gait Posture* (Feb. 2023). DOI: 10.1016/j.gaitpost.2023.11.002 (cit. on p. 91).